Hybrid analysis of ultra-high energy cosmic rays observed with the Telescope Array

Daisuke Ikeda
Department of Physics, School of Science,
University of Tokyo

Abstract

In this thesis, the energy spectrum of UHECRs ($E > 10^{18.7}$eV) was measured using the hybrid data from the Telescope Array experiment. For the precise measurement, the analysis method with the hybrid technique was developed.

The Telescope Array is the largest stereo-hybrid detector for UHECR observation in the northern hemisphere. It consists of three Fluorescence Detectors (FDs) which use the same technique as the HiRes and 507 Surface Detectors (SDs) which use the same technique as the AGASA. The hybrid events which are observed both by FD and SD are useful for the precise measurement of the characteristics of UHECRs and direct comparison between two types of technique.

In this analysis, the hybrid events are used for the precise reconstruction to measure the energy spectrum. To carry out this study, the method of the hybrid analysis, in which the timing information of SD is applied to FD monocular reconstruction, is developed. A full hybrid Monte Carlo (MC) simulation with an air shower simulation is also developed. The MC simulation includes the Utah atmosphere and the detector response with the time dependence. In the hybrid analysis, the resolutions which are estimated by using the MC simulation are less than 1.1 degrees of arrival direction and less than 8% of the energy for the observed UHECRs with energies above $10^{18.7}$ eV, respectively. They are quite better than the resolutions in the traditional analysis either by only the SD or FD monocular analysis for the events with lower energy.

The aperture of the hybrid event is also obtained by using MC simulation. The exposure between May 27, 2008 and September 28, 2009 for this analysis is about 3×10^{15} m^2 sr s for 10^{19}eV, which is equivalent to 6% of the AGASA exposure.

The systematic uncertainties in energy and flux are 19% and 12%, respectively. The measured energy spectrum is consistent with the result of the HiRes within the total systematic error.

Acknowledgement

I would like to express my great appreciation to my leading adviser, Hiroyuki Sagawa. His support, guidance and encouragement have allowed me to reach this point.

I would also like to express my gratitude to Masaki Fukushima. He guided me on many occasions. He also provided me suggestions, helpful advise and guidance for this work.

I would like to thank Shigeru Yoshida. He introduced me to the experimental physics and also to the Telescope Array experiment.

I would like to express my gratitude to N.Sakurai, H.Tokuno, T.Shibata, T.Nonaka, S.Ozawa and S.Udo. I learned from them many things related to physics and experiments.

I am grateful to all in the Telescope Array collaboration. Particular thanks go to A.Taketa and E.Kido. They gave me useful and inspiring discussions.

I would never forget those who worked for FD analysis: Y.Tsunesada, Y.Tameda, K.Hayashi, R.Ishimori, K.Honda, T.Tomida, S.Ogio, H.Fujii and Y.Takahashi. This thesis would never be completed without their support.

I gratefully acknowledge the financial support by the Japan Society for the Promotion of Science.

I would like to thank all the people who supported and encouraged me during my time in graduate school. Special thanks go to N.Okazaki, T.Iida, K.Ueshima, C.Ishihara and M.Ikeda.

Finally, I wish to express my deep gratitude to my family.

Contents

1 Introduction

Since the discovery of cosmic rays by V.F.Hess in 1912, the understanding of cosmic rays has been deepened by the various experiments and theories. The observed energy spectrum is shown in Fig. 1. The energy region of the cosmic rays is extended very widely from 10^9 eV to 10^{20} eV. The spectrum follows a power law with the index of -3. There are four regions in the spectrum which can be divided by two "knee" and one "ankle". The first knee is around 10^{15} eV where the power law index is changed from -2.7 to -3.0. The second knee appears around 10^{18} eV where the index is changed from -3.0 to -3.3. The ankle is around 10^{19} eV where the index is about -2.7. The ankle region, however, is not understood well because the flux of cosmic rays coming to earth is very small. How the universe generates the Ultra-High Energy Cosmic Rays(UHECR) remains as one of the greatest mysteries in the astrophysics.

In the past ten years, the AGASA[1] and High Resolution Fly's Eye(HiRes)[2] observed and published the energy spectrum around GZK cut off (see Fig. 2). It is predicted that the energy spectrum of cosmic rays shows the cut off around $10^{19.6}$ eV by the interaction between UHE proton and the photons of Cosmic Microwave Background(CMB), called "GZK cut off"[3][4]. The HiRes spectrum has the cutoff, but the spectrum of AGASA extends beyond the GZK cut-off. There are several theories to explain the super GZK spectrum, by decay or interaction of exotic particles, breaking of the special relativity, and so on. It is one of the most important topics in the UHECR physics to understand the reason of the inconsistency between the AGASA and HiRes experiments and to measure energy spectrum correctly.

The AGASA experiment observed UHECRs with the Surface Detectors (SDs) of plastic scintillator. On the other hand, the HiRes experiment uses the Fluorescence Detectors (FDs). The SDs provide larger exposure than FD, but the measured energy by SD depends on the lateral distribution of energy deposition in SDs on the ground from particles in air shower on the ground. The lateral distribution depends strongly on the interaction process of the UHECR and atmospheric molecules strongly. But the interaction has large uncertainty because the center of mass energy of the collision is larger than that of the accelerator experiment. For example, the center of mass energy of the collision between the proton of the energy of 10^{20}eV and atmospheric molecular is 433TeV. On the other hand, the center of mass energy of the Tevatron[5] is 2TeV and of the LHC[6] will be 14TeV. So the energy obtained by the SD has the uncertainty of air shower Monte Carlo simulation.

On the other hand, longitudinal development of the air shower is observed by FD technique. The amount of the emitted fluorescence yield in the atmosphere is proportional to the energy deposited by the ionization loss. And the energies of UHECRs are measured calorimetrically by FD. However, the energy spectrum measured by FD also has systematic uncertainty because the aperture of FD depends on energy.

In recent years, the Telescope Array (TA) experiment[7] and Pierre Auger Observatory[8] are running to observe UHECRs with the improved technique and aperture. The most important

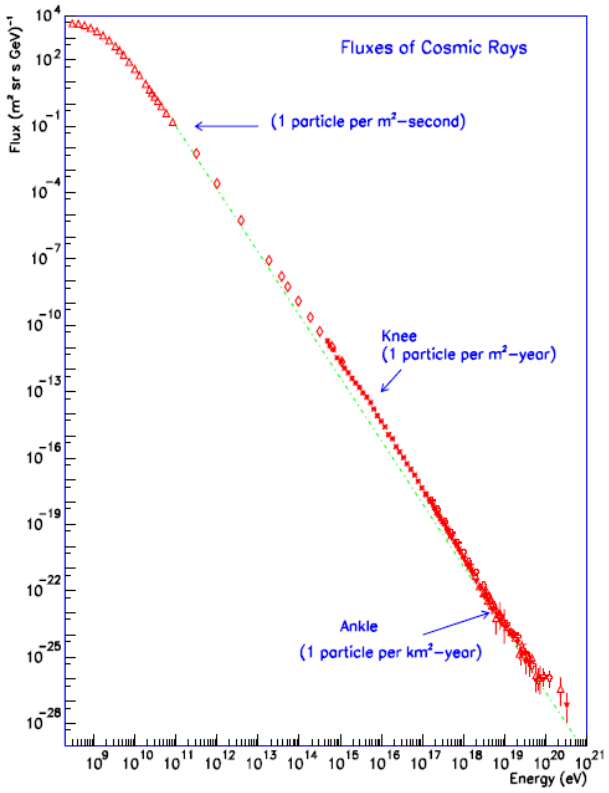

Fig. 1: The energy spectrum of cosmic rays.

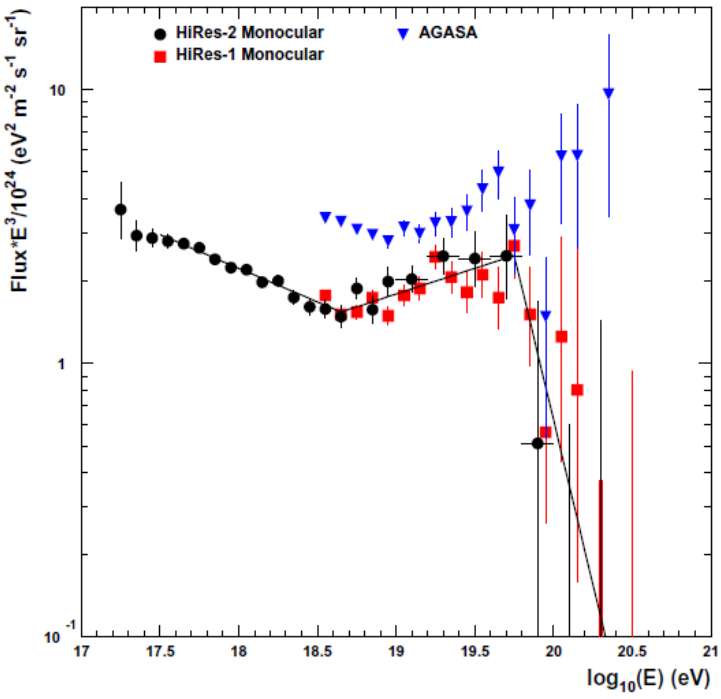

Fig. 2: The energy spectra observed by AGASA and Hires.

technique of these experiments is the “hybrid observation”, by which air showers are observed simultaneously both by SD and FD. The TA SDs are plastic scintillator detectors in the same way as the AGASA detectors, and one set of the telescopes among three TA FD stations is transferred from the HiRes site. The Auger experiments is also the hybrid detector, but the SDs are the water Cherenkov detectors that are sensitive to muons. Only the TA will perform direct comparison between the AGASA and HiRes by hybrid observation. The hybrid analysis in the TA will reveal the reason why the previous experiments showed inconsistency explicitly.

Additionally, the TA has the absolute calibration technique by the electron linear accelerator called Electron Light Source (ELS). By observing fluorescence light from air showers induced by the ELS with the known total energy, fluorescence yield and detector sensitivity are calibrated with about 5% uncertainty. This end-to-end calibration is the first trial in the world and will be started in the spring of 2010. By the calibration with the ELS and atmospheric transparency, the TA will have less uncertainty of energy by hybrid analysis than the other experiments.

The hybrid analysis uses the merit both of the SD and FD. The SD has precise aperture, but the measured energy has uncertainty that depends on hadronic interaction models. On the other hand, the FD measures energy calorimetrically with precise accuracy and will measure energy more accurately by the ELS calibration, but the aperture has uncertainty from its energy dependence. So the hybrid analysis in TA measures the energy spectrum with precise aperture and accurate energy scale.

If the energy scales between SD and FD are inconsistent, there is a possibility that the difference is originated from incorrectness of hadronic interaction between UHECRs and atmospheric molecules in air shower MC simulation. In this thesis, there are two main topics about hybrid analysis in the TA experiment. One is the development of the precise hybrid reconstruction with the information both of FD and SD. The other is the measurement of the energy spectrum above $10^{18.7}$eV by using the hybrid events observed for the first one and half a years. In future, this work will also be used for the SD-FD comparison as the direct comparison with the AGASA and HiRes.

The Section 2 gives an introduction to the UHECR physics. In Section 3 and Section 4, some details about the TA experiment and its calibration are explained. In Section 5, we describe the overview of the hybrid analysis. In Section 6, we present the details of the detector MC simulation for the hybrid event. In Section 7 and Section 8, we discuss the method of the geometry reconstruction by the hybrid technique and its resolution studied by using MC simulation. The aperture to measure the spectrum is also presented in those sections. In Section 9 and Section 10, we present the result of the reconstruction for the real data and energy spectrum. In Section 11, the systematic errors for the energy spectrum are discussed. In Section 12, the prospect of the hybrid analysis is discussed. Finally, in Section 13, we present a conclusion.

2 Ultra-High Energy Cosmic Rays

2.1 Propagation of the UHECRs

Intergalactic space is filled with the radiation of photons called Cosmic Microwave Background (CMB) radiation[10] and Intergalactic Infrared Background Radiation(IIBR)[9]. Since UHECRs can interact with these photons, CMB plays the important role in the propagation of UHECRs. The important interaction processes are the photopion production, pair-production of the electron and positron, and photo-disintegration.

2.1.1 Photopion Production

The main process of photopion production occurs by the Δ resonance. The single pion production modes are

$$\gamma + p \rightarrow \Delta^+ \rightarrow \pi^+ + n \quad (1)$$

$$\gamma + p \rightarrow \Delta^+ \rightarrow \pi^0 + p. \quad (2)$$

The examples of two pion production modes are

$$\gamma + p \rightarrow \Delta^{++} + \pi^- \quad (3)$$

$$\Delta^{++} \rightarrow \pi^+ + p, \quad (4)$$

$$\gamma + p \rightarrow \rho^0 + p \quad (5)$$

$$\rho^0 \rightarrow \pi^+ + \pi^-. \quad (6)$$

The energy threshold for the photopion production is the center of mass energy that equals the mass of the π^0. It corresponds to the primary energy of 6.79×10^{19}eV for proton. The cross section of this process is measured by using accelerator and summarized in [11] as shown in Fig. 3. The maximum cross section is about 500μb at the center of mass energy of about 1.5GeV^2. It corresponds to the head-on collision of CMB photon and proton at 2.0×10^{20}eV. Above this energy, the cross section continues as constant value of about 100μb. The calculated attenuation length by this process shown in Fig. 4 shows the significant decrease at $10^{19.6}$eV. This process plays the main role for creating GZK cut off.

2.1.2 Pair Production

Pair-production process occurs if the Lorentz factor of the cosmic ray is larger than 10^9, the corresponding energy is about 10^{18}eV for the proton. If UHECRs are protons, this process does not affect strongly since the minimum attenuation length is about 3Gpc at 10^{19}eV[12][13] (see Fig. 4). For the nuclei, however, the attenuation length becomes smaller at the higher energy. For instance, it becomes 300Mpc at 10^{20}eV. If UHECRs are iron nuclei, this process will be dominant for the propagation in the intergalactic space.

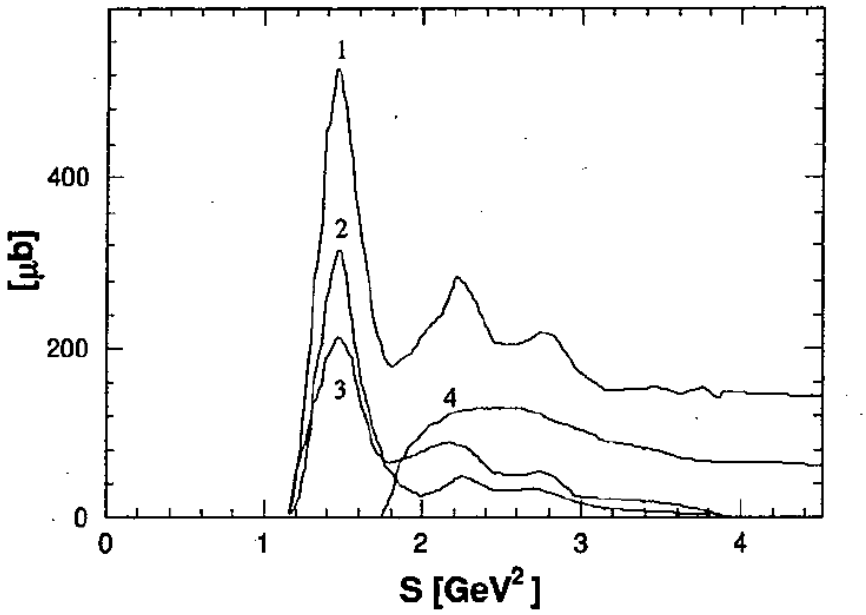

Fig. 3: Cross sections for p-γ interaction. 1:the summation of all channels, 2:$\gamma p \to p\pi^0$, 3:$\gamma p \to n\pi^+$, 4:$\gamma p \to p + 2\pi$ [11].

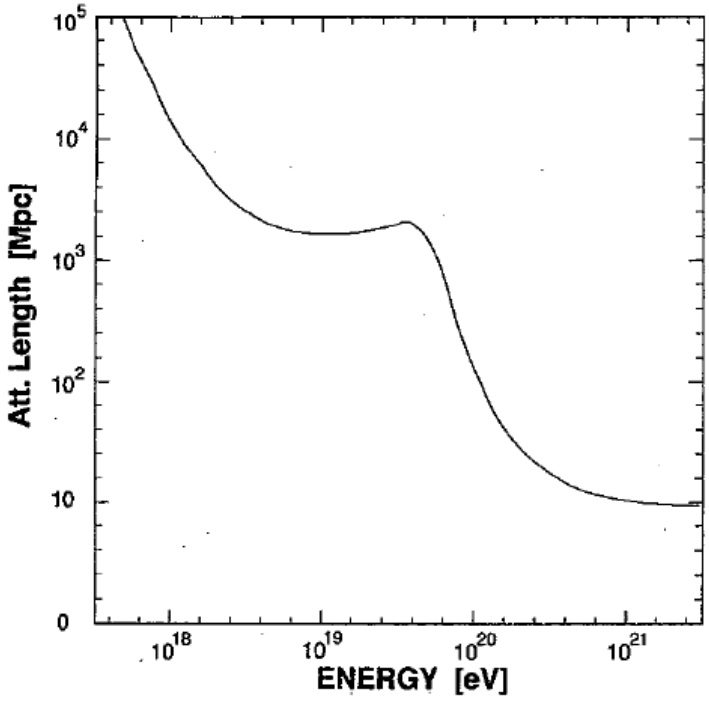

Fig. 4: The attenuation length with the pair production of e^+e^- and photopion production[11]. The left shape around 10^{19} eV is created by pair production and the right shape around 10^{20} eV is created by photopion production.

2.1.3 Photo-disintegration

The nucleus interacts with the background photon and disintegrates into lighter nuclei. If UHECR is the nucleus, this is the main interaction for considering the energy deposit during the propagation. The nucleus is affected strongly by the photons with the energy in the rest system of the nuclei from 10MeV to 30MeV. This is the domain of the giant dipole resonances of the nuclear photo-disintegration. The upper energy for the meson production is about 150MeV[14]. In the case of the head-on collision with the photon and iron, the energy of iron is 3.75×10^{20}eV which corresponds to the energy of photon of 10MeV.

The average cross section of this process summarized by J.L.Puget[15] shows 104.1mb at the photon energy around 30MeV. The attenuation length is shown in Fig. 5[16]. For the nuclei, this process dominates in the most of energy range for the target of the UHECR measurement. So if UHECRs are nuclei, the energy spectrum will be reduced at the energy almost same as GZK cut off.

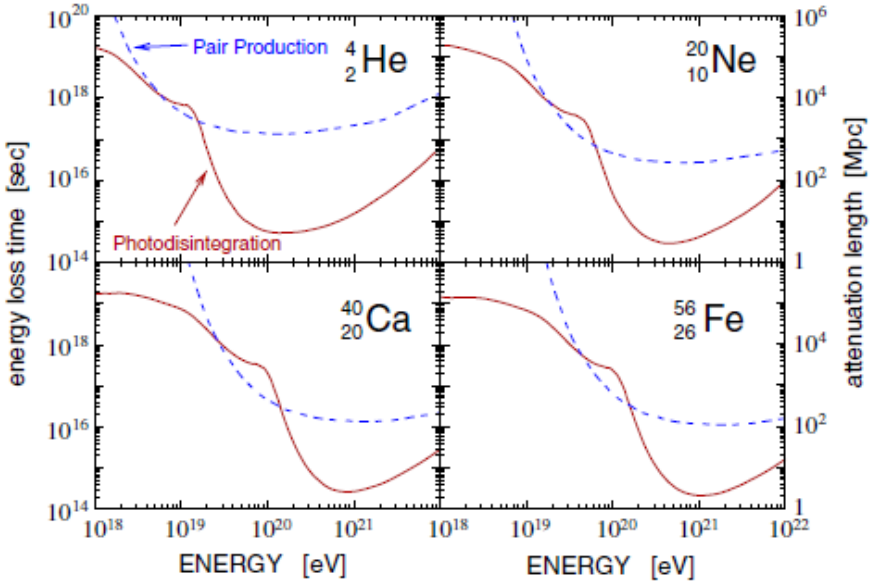

Fig. 5: The attenuation length of the He,Ne,Ca and Fe by the e^+e^- pair production and photo-disintegration[16].

2.2 Origin of the UHECRs

The origin of UHECRs remains as a mystery. There are two types of model to explain the origin. One is the acceleration in the astronomical objects. This is called “bottom-up” model. The other is the decay or interaction mechanisms of the exotic particle, being called “top-down” model.

The bottom-up models may be divided into the following two types of popular scenarios: diffusive and incident acceleration[17]. The most famous scenario is the diffusive shock wave acceleration. Cosmic ray will be accelerated while a particle move near the boundary of shock wave and leave from this accelerator. For accelerating up to UHECR energy, however, the particle has to be confined within the diffusive shock region during the time needed by acceleration. So the candidate of the source of UHECRs is limited by its size and of the strength of magnetic field. The cooling by radiation loss also has to be considered to pick up the candidate objects.

The possible acceleration sites with the constraints of size, magnetic field and cooling loss are shown in Fig. 6[18]. Only powerful active galaxies (radio galaxies, quasars and BL Lac and so on) are capable as the origin of UHECR. Gamma-ray bursts (GRBs) and super-massive black holes in AGN also remain as the origin of UHECR.

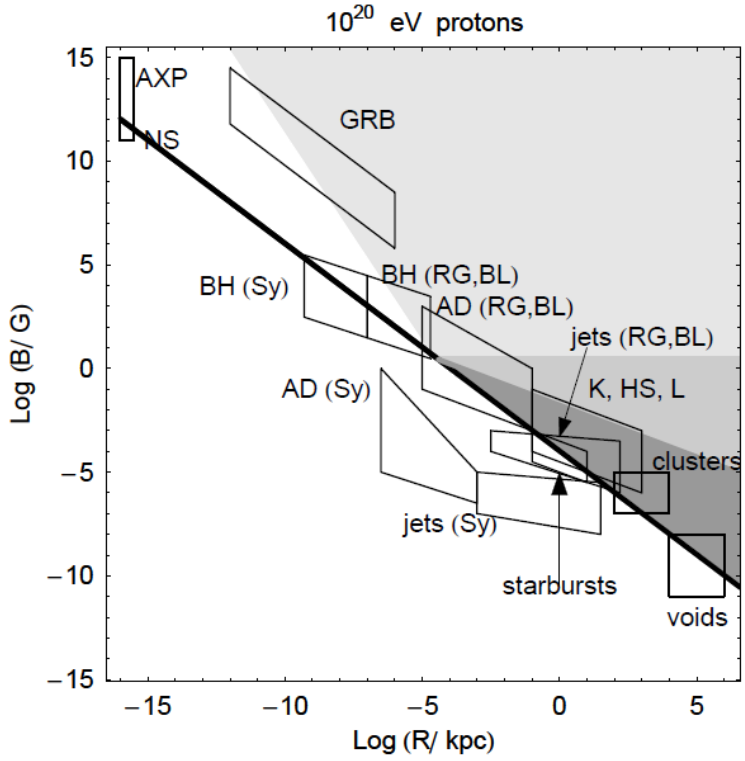

Fig. 6: The size and strength of the magnetic field of the astronomical objects[18]. Boxes denote parameter regions for objects in which conditions for this loss regime may be satisfied, that is central parsecs (AD) of active galaxies (low-power Seyfert galaxies (Sy) and powerful radio galaxies (RG) and blazars (BL)), relativistic jets, knots (K), hot spots (HS) and lobes (L) of powerful active galaxies (RG and BL); non-relativistic jets of low-power galaxies (Sy); starburst galaxies; gamma-ray bursts (GRB); galaxy clusters and intercluster voids. The thick line shows the lower boundary for the proton at 10^{20}eV.

The top-down mechanisms is caused by decay or interaction of exotic particles, the decay

of a super heavy relic particle, dark matter or the interaction of a magnetic monopole[19]. Most of the scenarios predict that these mechanisms generate very high energy photons and are thus able to be verified by measurement for the composition of the UHECR. However, ultra-high energy photons have not been observed by now.

On the other hand, the anisotropy can be also verified if the UHECR is produced by dark matter since the matter density is high around the galactic center. The decay of interaction mode of the dark matter also generates the photon and neutrino. So we can observe anisotropic ultra high energy photons in this scenario.

2.3 Air Shower Phenomena

An UHECR particle entering the atmosphere generates the high energy hadrons by the collision with air molecules. These secondary particles also generate the other particles, mainly π mesons. The produced $\pi^+\pi^-$ mesons become the source of the muons observed on the ground. The π^0 particles decay into two photons and starts the electro-magnetic shower. These giant hadronic and electro-magnetic showers are called air showers. The pattern diagram of these phenomena is shown in Fig. 7. This shower, which mainly consists of e^+e^-, and photons, is developed with billions of particles and it reaches the ground over the radius of several kilometers. These charged particles also generate the ultraviolet light through the fluorescence phenomena. Generally, the observation for the primary UHECR is done through the observation of the air shower.

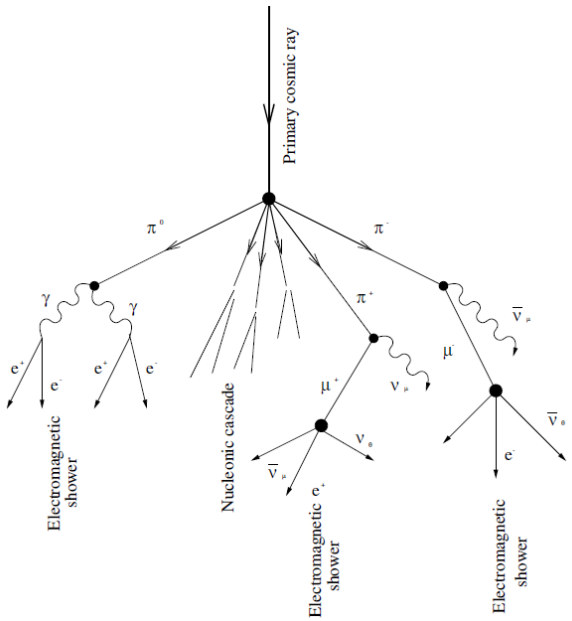

Fig. 7: The pattern diagram for the development of the air shower.

2.3.1 Properties of Air Showers

The important properties for the observation of UHECR are the lateral distribution on the ground and the longitudinal development of the charged particles in the air. The lateral distribution is formed mainly by the interaction at the early stage of the hadronic shower and the multiple Coulomb scattering in the electro-magnetic shower, and the latter is dominated. The typical scattering angle for electrons with energy E is given by

$$< \theta^2 > = (E_s/E)^2 \quad (7)$$

$$E_s = \frac{4\pi}{\alpha}^{1/2} m_e c^2 \simeq 21\mathrm{MeV}, \quad (8)$$

where α is the fine structure constant. The spread by the scattering of electrons with critical energy ε_0 which run by one radiation length X_0 can be used as the typical scale for the lateral distribution.

$$X_m = (E_s/\varepsilon_0)X_0 \simeq 9.3\mathrm{g/cm}^2. \quad (9)$$

Here X_m is called Moliere unit. The lateral distribution indeed scales to X_m as the Nishimura-Kamata-Grisen (NKG) function.

$$\rho_e(R,s) = N_e C \left(\frac{R}{R_m}\right)^{(s-2.0)} \left(1+\frac{R}{R_m}\right)^{(s-4.5)} \quad (10)$$

$$s = \frac{3t}{t+2y} \quad (11)$$

$$y = ln\left(\frac{E}{\varepsilon_0}\right), \quad (12)$$

where t is the longitudinal atmospheric depth and s is the degree of the cascade development which is called age parameter. Here s = 1 is equivalent to maximum development and s > 1 corresponds to the cascade attenuation region. Ne is the total number of electrons at each depth and described as the longitudinal development analytically by the Gaisser-Hillas formula

$$N_e(E, X-X_1) = N_{max}\left(\frac{X-X_1}{X_{max}-\lambda}\right)^p \exp\left[-\frac{X-X_1}{\lambda}\right] \quad (13)$$

$$p+1 = \frac{X_{max}}{\lambda}, \quad (14)$$

where X_{max} is the shower maximum, X_1 is the atmospheric depth at the first interaction point of the air shower, and λ is the attenuation length which is $\simeq$ 70 g/cm^2 for the proton. The total energy deposit E_{cal} is calculated by integration of this function. The integrated formula is written simply:

$$E_{cal} = \lambda N_{max} \overline{\frac{dE}{dX}} (\frac{e}{\xi})^\eta \Gamma(\xi+1) \quad (15)$$

$$\xi = \frac{X_{max}-X_1}{\lambda}, \quad (16)$$

where $\overline{\frac{dE}{dX}}$ is the average value of the energy deposit when the charged particles run by x. If we know the ratio of the deposited energy to the energy of the primary particle, we obtain the energy of the primary particle by this function.

2.3.2 Fluorescence Light

When charged particles pass through the atmosphere, energy is deposited to the atmospheric molecules by ionization loss phenomena. These molecules emit a part of these energies as the visible or ultraviolet photons, which are called atmospheric fluorescence light phenomena. Since the air shower includes so many charged particles, these emitted photons are observed by the telescope.

Most of molecules of atmosphere emit for the fluorescence photons. However, the effect from N_2 is dominated. There are three main processes.

1. Direct excitation

   N_2 is excited directly by high energy charged particles in air shower as 1N system.

$$N_2 + e^- \rightarrow N_2^{+*} + e^- + e^-. \tag{17}$$

2. Excitation by secondary electrons

   The high energy charged particles produce secondary electrons in ionization. N_2 is also exited by these electrons as 2P system.

$$N_2 + e^- \rightarrow N_2^*(C^3\Pi_u) + e^-. \tag{18}$$

$$N_2 + e^- \rightarrow N_2^*(C^3\Pi_u). \tag{19}$$

3. Excitation by Auger electrons

These excited N_2 molecules, however, do not emit all energies to photons since N_2 molecules lose the energy by collision to the other atmospheric molecules. This phenomenon is called "quenching". This effect makes fluorescence yield small dependence of the pressure. Generally, the number of fluorescence photons per unit length is given by

$$Y_\lambda = \frac{A_\lambda \rho}{1 + \rho B_\lambda \sqrt{T}}, \tag{20}$$

where Y_λ is emitted photons per unit length, ρ is the atmospheric density, T is the temperature and A_λ and B_λ are constants for each wavelength[21].

These parameters, A_λ, B_λ and emission spectrum are measured by laboratory experiments. The absolute number of fluorescence photons for multiple energies, 1.4MeV electrons of ^{90}Sr and 300MeV, 600MeV and 1000MeV electron beam prepared by the accelerator in Institute for

Nuclear Study (INS), were measured by Kakimoto[22] with 10% systematic error. From this experiment, the parameters of Eq. 20 are obtained as follows:

$$yeild = \frac{\frac{dE}{dX}}{\frac{dE}{dX}_{1.4MeV}} \times \rho\left(\frac{A_1}{1+\rho B_1\sqrt{t}} + \frac{A_2}{1+\rho B_2\sqrt{t}}\right) \quad (21)$$

$$A_1 = 89.0 \pm 1.7 \mathrm{m^2 kg^{-1}} \quad (22)$$

$$A_2 = 55.0 \pm 2.2 \mathrm{m^2 kg^{-1}} \quad (23)$$

$$B_1 = 1.85 \pm 0.04 \mathrm{m^3 kg^{-1} K^{1/2}} \quad (24)$$

$$B_2 = 6.50 \pm 0.33 \mathrm{m^3 kg^{-1} K^{1/2}}, \quad (25)$$

where A_1 is the values for wavelength of 337nm and 358nm, B_1 are for 391nm.

The relative spectrum of fluorescence, excited by a 28.5GeV electron beam was measured by FLASH experiment[23] with a spectrograph. The results at 2.1×10^4 Pa, which correspond to the upper altitude range of UHECR detection, are shown in Fig. 8. The lines at 337nm, 357nm and 391nm are dominated in the fluorescence spectrum.

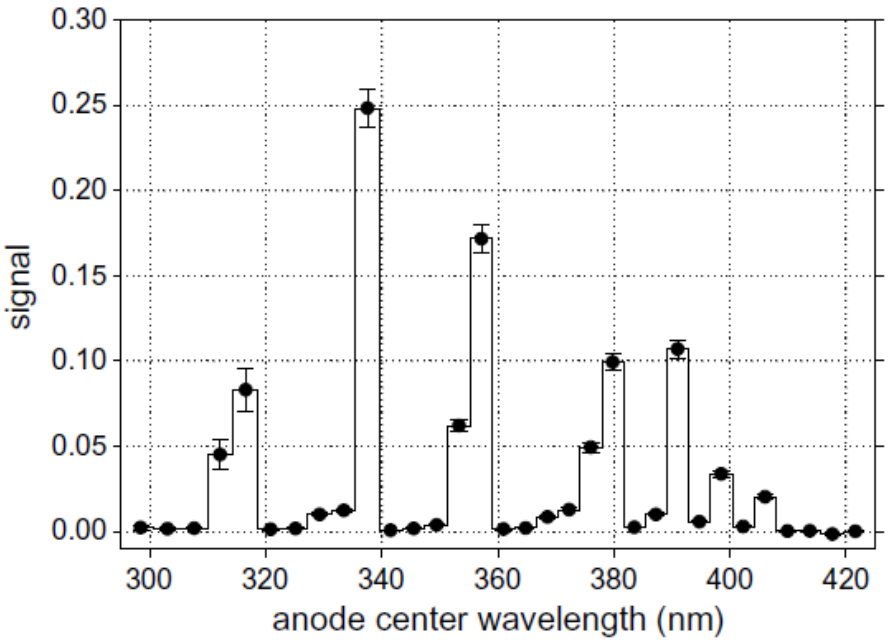

Fig. 8: Fluorescence spectrum in 2.1×10^4 Pa air measured by FLASH[23].

2.3.3 Cherenkov Light

When a charged particle passes through the atmosphere with the velocity greater than the speed of light in that material, Cherenkov photons are also emitted with characteristic angle,

$$\cos\theta = \frac{1}{n\beta}, \quad (26)$$

where θ is the emission angle, β is v/c and n is the refractive index. The threshold energy is 37 MeV for electrons and 7.6GeV at an altitude of 10km with US standard atmosphere[24], which is given by

$$E_{th} = \frac{mc^2}{\sqrt{2(1-n)}}. \tag{27}$$

Here m is the mass of corresponding particles and c is the speed of light.

Since air shower also has many charged particles with high velocity, mainly e^+e^-, it also becomes the important phenomenon. The total number of Cherenkov photons produced in a shower is given by

$$\frac{dN}{dXd\theta}(X,\theta,h) = A(X,\theta,h)N(X)\int_{E_{th}}^{\infty} y(h,E)\, f_e(X,E) dlnE \tag{28}$$

$$f_e(X,E) = \frac{1}{N_e(X)}\frac{dN_e}{dlnE}(X,E), \tag{29}$$

where X is the atmospheric depth, h is an altitude, y(h,E) is the Cherenkov photon yield which depends on particle energy and height, A(X,θ,h) is the angular distribution of produced Cherenkov photons, N(X) is the number of charged particles at each atmospheric depth, f_e(X,E) is the normalized differential electron energy spectrum as functions of depth X and E.

These angular distribution and energy spectrum of electrons in the air shower are calculated and parameterized by the simulation of CORSIKA[25] and GEANT [26] by Nerling *et al.* [27]. The results are

$$f_e(X,E) = \frac{E}{(E+a_1)(E+a_2)^s} \tag{30}$$

$$a_1 = 6.42522 - 1.53183 \cdot s \tag{31}$$

$$a_2 = 168.168 - 42.1368 \cdot s \tag{32}$$

$$a_0 = k_0(E_{sim}) \cdot \exp(k_1 \cdot s + k_2 \cdot s^2) \tag{33}$$

$$k_0(100keV) = 0.142049 \tag{34}$$

$$k_1(100keV) = 6.18075 \tag{35}$$

$$k_2(100keV) = -0.605484, \tag{36}$$

where E is the energy of primary particles in MeV, s is the age parameter as described in Eq. 12, E_{sim} is the lower threshold energy for tracing electro-magnetic particles in the simulation. The angular distribution of produced Cherenkov photons is given by

$$A(\theta,h,s) = a_s(s)\frac{1}{\theta_c(h)}e^{-\theta/\theta_c(h)} + b_s\frac{1}{\theta_{cc}(h)}e^{-\theta/\theta_{cc}(h)} \tag{37}$$

$$a_s(s) = a_0 + a_1 \cdot s + a_2 \cdot s^2 \tag{38}$$

$$b_s(s) = b_0 + b_1 \cdot s + b_2 \cdot s^2 \tag{39}$$

$$\theta_c = \alpha \cdot E_{th}^{-\beta} \quad \text{with } E_{th} \text{ in MeV} \tag{40}$$

$$\theta_{cc} = \gamma \cdot \theta_c(h) \quad \text{with } \gamma = \alpha' + \beta' \cdot s \tag{41}$$

$$(a_0, a_1, a_2) = (4.2489 \times 10^{-1}, 5.8371 \times 10^{-1}, -8.2373 \times 10^{-2}) \tag{42}$$

$$(b_0, b_1, b_2) = (5.5108 \times 10^{-2}, -0.5587 \times 10^{-2}, -5.6952 \times 10^{-2}) \tag{43}$$

$$(\alpha, \beta) = (0.62694, 9.60590) \tag{44}$$

$$(\alpha', \beta') = (10.509, -4.9644), \tag{45}$$

A fluorescence telescope observes not only fluorescence lights but also Cherenkov light. For the measurement of the energy of the UHECR by the calorimetric fluorescence technique, the observed photons have to be separated into the origins of the fluorescence and Cherenkov phenomena. Since the difference of these photons is the longitudinal development along the shower axis, the reconstruction method of the telescope uses this characteristic for the separation of these photons.

3 Telescope Array Experiment

The Telescope Array which is located at Utah desert in United States (39.30° Latitude, -112.91° Longitude and 1382m A.S.L.) is the largest UHECR detector in the northern hemisphere[7] (Fig. 9). The main target of this experiment is precise measurement of the energy spectrum, arrival direction and composition of UHECR through the investigation of the inconsistency about GZK cut off between the results of the AGASA and HiRes. For this subject, TA uses the hybrid technique with three stations of Fluorescence Detectors (FDs) which are the same as HiRes technique and 507 Surface Detectors (SDs) which are the same as AGASA technique (Fig. 10). Each detector measures UHECRs through the observation of air showers created by the interaction between UHECRs and atmospheric molecules (Section 2.3). SD directly observes particles in air shower on the ground and FD detects fluorescence photons generated by air shower (Section 2.3.2). Since one of the FD station, which is the north station called the Middle Drum (MD), is the detector transferred from the HiRes experiment, we can compare the result from the MD site with the Hires result directly. The “hybrid” observation started from March 2008.

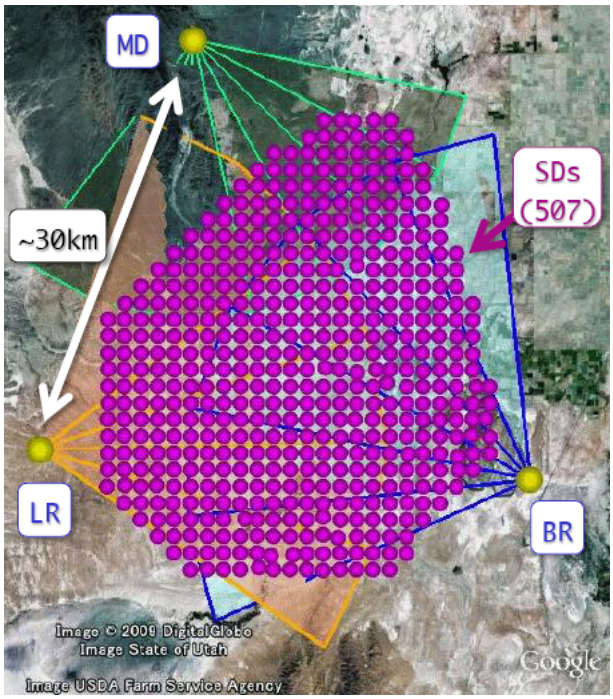

Fig. 9: Overall view of the detectors in the Telescope Array. Purple points show the positions of 507 surface detectors and yellow points show the three fluorescence stations (BR:Black Rock Mesa, LR:Long Ridge, MD:Middle Drum).

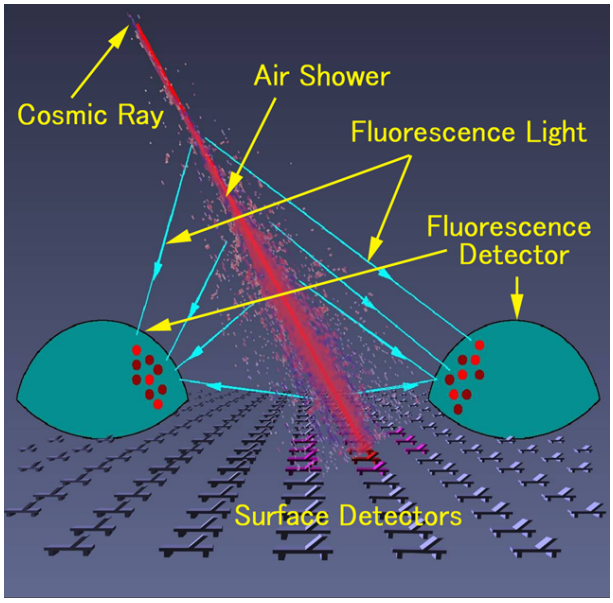

Fig. 10: The pattern diagram of the hybrid observation.

3.1 Surface Detectors

3.1.1 Detector

The 507 SDs of TA using a plastic scintillator which is the same as AGASA detector cover 700km^2 approximately in 1.2km spacing (Fig. 11)[30]. Fig. 12 shows the schematic views of inside of a surface detector. It consists of 3m^2 plastic scintillator of 1.2cm thickness with two layers which are separated by 1mm thick stainless-steel and read out each by one PMT (Electron Tube 9124AS) independently (Fig. 13). Each PMT is calibrated to obtain the relation between the applied voltage and the gain, and linearity curve. Two LEDs (Nichia NSPB320BS) are also installed at each layer to calibrate the linearity of PMT response. The photons produced in scintillator is guided by 104 Wave-Length Shifting Fibers (WLSFs) (Kuraray WLSfiber Y-11) with 2cm spacing. The non-uniformity of the detector response at the PMT is less than 5%.

Each SD has 120W solar panel with one deep-cycle battery (DCS1001T C&D technologies) to provide sufficient power (4W) itself. The battery can supply the power for 3 days without electric generation by solar panel. The battery is mounted in the cooler box at the backward of the solar panel with electronics for data acquisition (Fig. 14) to keep moderate temperature. The output signal are recorded by electronics with 12bit Flash ADCs (FADCs) which are running with 50MHz of sampling rate, FPGA for fast signal processing, CPU for slow signal processing, CPLD for board control, one charge controller, ADCs for monitoring, and DACs for setting high voltage of PMTs through power bases. The pedestals of FADCs are monitored. All electronics are synchronized by 1pps signal received by GPS unit with time

Fig. 11: A picture of a deployed SD. Scintillator box is under the roof visible in the picture. Electronics box is located under the solar panel. These components are on the iron frame.

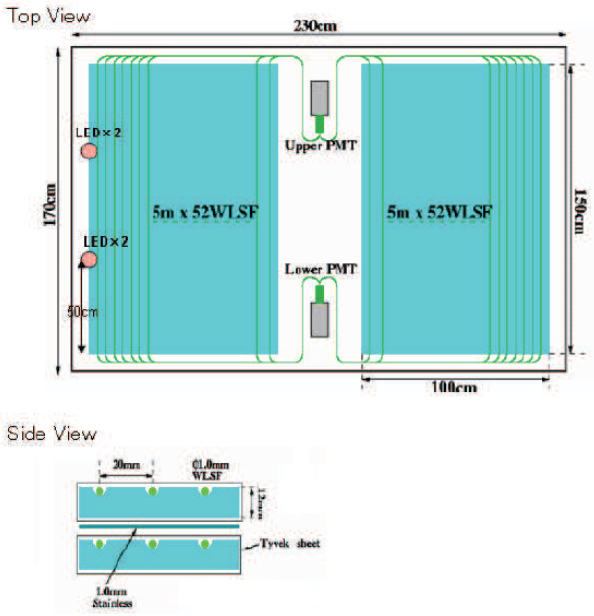

Fig. 12: Top view and side view of the detector inside stainless-steel box. There are two layers of 3m^2 scintillator and 104 WLSFs on each layer.

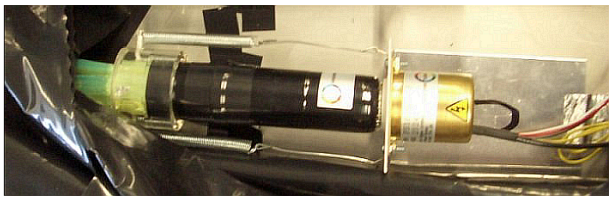

Fig. 13: The PMT for SD (Electron Tube 9124SA) with 9/8-inch diameter. It is covered with Mu-metal for protection from geomagnetism.

Fig. 14: The stainless-steel box at the backward of the soler panel. Battery is set in the cooler box to keep moderate temperature (left figure). The cooler box and electronics for the data acquisition are set in the stainless-steel box for the protection from the rain and wind (right figure). This stainless-steel box is closed and locked after deploying.

resolution less than 20nsec and are cleared by 50MHz of the sub clock on the system board. The electronics also has the GPS unit (Motorola M12+) and wireless LAN modem with the maximum speed of 11 Mbps using 2.4GHz spread spectrum technology by using an 802.11g wireless network(Fig. 15,Fig. 16). The planar-type antenna is used for most of the surface detectors while the parabolic antenna with higher gain is used for the detectors far or out of sight from the communication tower. Since it is impossible to distribute triggers and clocks in real time, the surface detectors are operated autonomously and synchronized to each other with the wireless LAN.

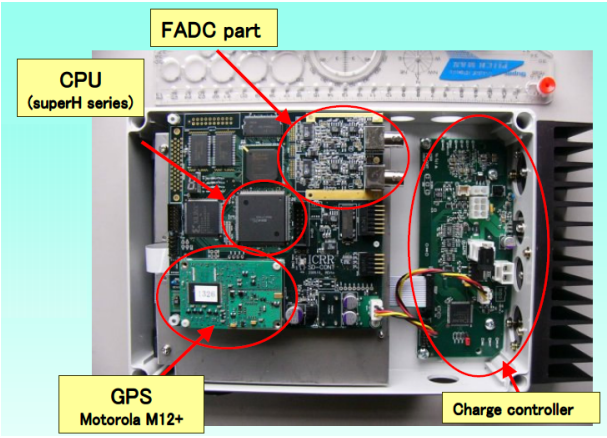

Fig. 15: Top view of the SD electronics.

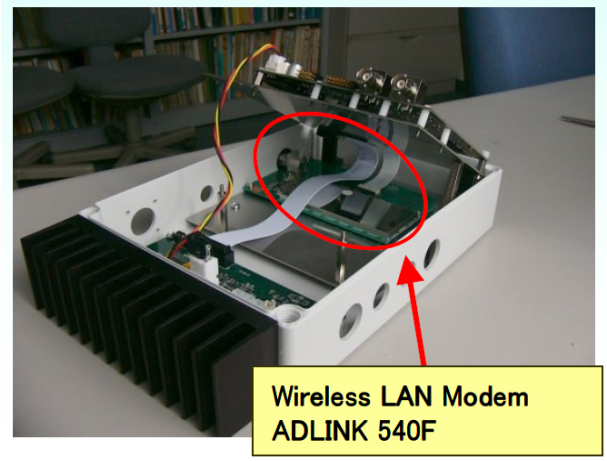

Fig. 16: The wireless LAN modem is set under the main board.

3.1.2 Trigger and DAQ system

To achieve efficient and stable SD DAQ, we divided the whole area into three sub-arrays which have each communication tower with host electronics system. The communications system between towers uses standard communications architecture based on commercially available microwave equipment to provide point-to-point links with 5.8 GHz band[31]

Output signals from PMTs are continuously digitized using FADCs. The recorded waveforms are judged for the trigger by the unit of Minimum Ionization Particles (MIPs), which corresponds to the deposited the energy by ionization loss of single charged particles with high energy. At the current setup, signals greater than $0.3 \times$ MIPs equivalent are stored to memory buffer with a time stamp by a GPS as Level-0 trigger data. When upper and lower PMTs detect greater than 3 MIPs,the trigger timing information is locally stored in a trigger list as Level-1 trigger, which is transmitted to the corresponding host tower electronics at 1 Hz by wireless network. The host electronics judges the final coincidence trigger based on the trigger table with 3 SDs pattern match for searching for the cluster with a time window within 8μs to take waveforms from SDs as Level-2 trigger. The final Level-2 trigger rate is around 0.003Hz for each sub-array.

When tower electronics generates the Level-2 trigger, corresponding SDs which store the event with good coincidence timing within $\pm 32\mu$s start to send the waveforms to each tower. The data in a tower electronics are transmitted and once stored in a tower PC inside a cabinet at the tower site. The data taken in the tower PC are transmitted the Cosmic Ray Center in the town near TA site later via networks between towers.

The sub-array DAQ system began to run in March 2008. We also installed a cross-boundary trigger between neighboring two or three regions in November 2008. One of the tower electronics works as a central PC and judges the cross-boundary trigger from the trigger information with the other two sub-arrays. Fig. 17 shows the map of triggered surface detectors before and after installing a cross-boundary trigger. The cross-boundary trigger works well and the uniformity of Level-2 trigger becomes good.

3.1.3 Monitoring

Each detector has the following real-time monitors.

- Every second
  - the number of events with signals greater than 3 MIPs, which corresponds to the Level-1 trigger rate.
  - GPS time stamps
  - the number of clock count between 1pps

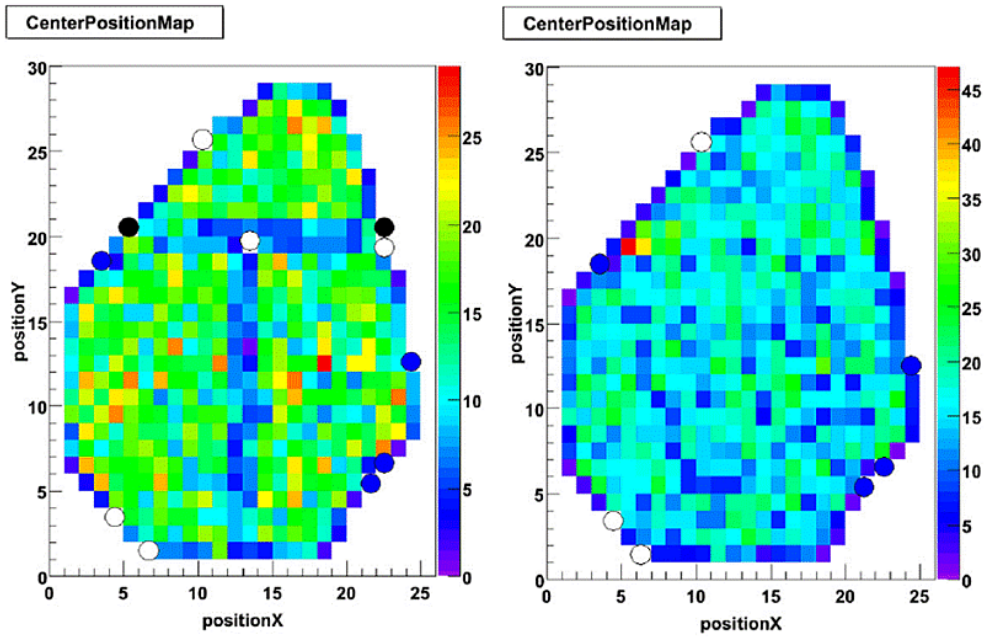

Fig. 17: Maps of triggered surface detectors. The left figure is the map before installing the cross-boundary trigger. There was inefficiency of Level-2 trigger at around X=13 or Y=20. The right figure is the map after installing the cross-boundary trigger. Ineffiency around the boundary of each sub-arrays disappeared.

- Every minute
  - the number of events with signals greater than 0.3 MIPs which corresponds to the Level-0 trigger rate
  - battery voltage
  - charge current
  - voltage of solar panel
  - temperature in the cooler box, electronics and stainless-steel box
  - humidity inside the stainless-steel box
- Every 10 minutes
  - charge histogram
  - pedestal histogram
  - the number of detected satellites and antenna connection of the GPS

Fig. 18 shows the examples of several monitors from one surface detector. In this case, the number of detected satellites is about 8, the battery voltage is from 12V to 14V, charging

current is about 0.3A during night time, 750Hz of the Level-0 trigger, 20Hz of the Level-1 trigger, temperature near the scintillator is from -8° to 23°, and humidity changed from 20% to 60%.

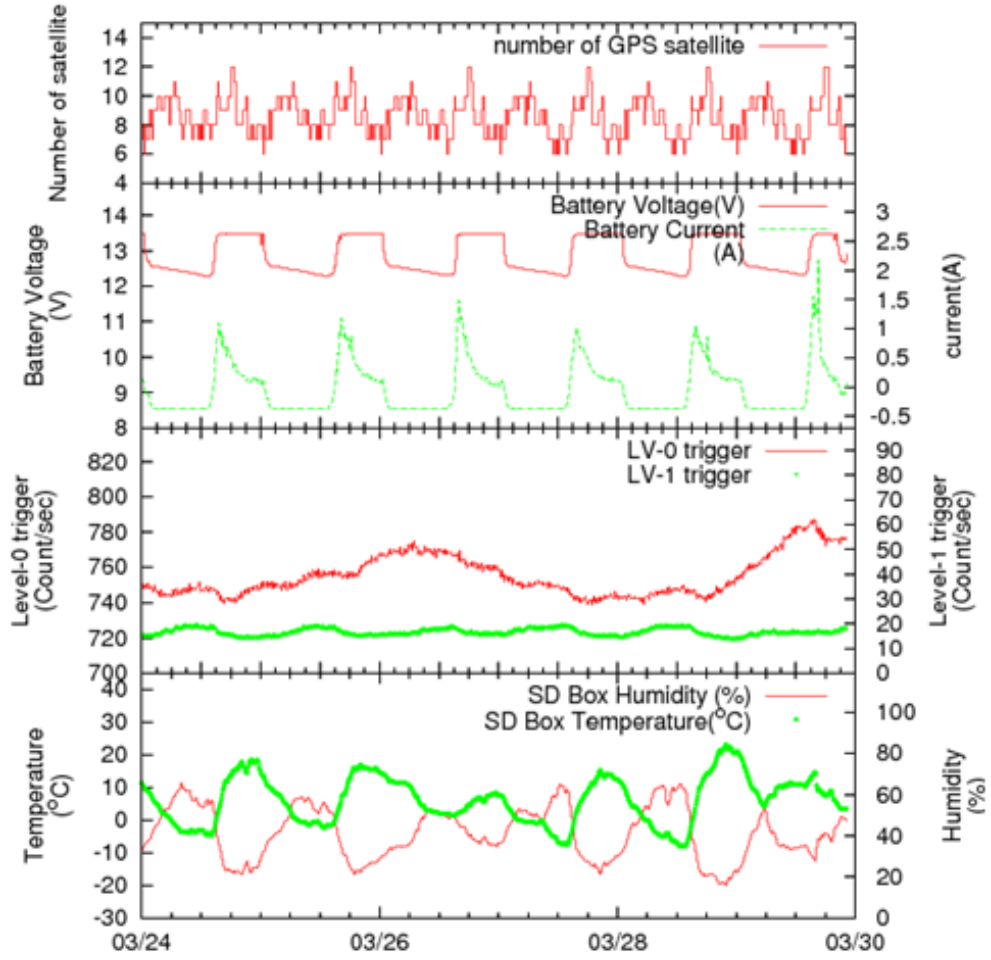

Fig. 18: Examples of SD real-time monitoring.

3.2 Fluorescence Detectors

3.2.1 Detector

The Telescope Array has three stations of fluorescence detectors called “Black Rock Mesa“(BR), ”Long Ridge“(LR) and ”Middle Drum“(MD). At the BR and LR sites, we have constructed new detectors designed specifically for the TA experiment. Each station has twelve telescopes: six telescopes are in the upper side, and the other six telescopes are in the lower side. The overview of the FD is shown in Fig. 19. The upper and lower rings cover 3°-33° in elevation and 108° in azimuth. This field of view (FOV) covers the whole area of the SD array. Each telescope

has a camera with 256 pixel photo-tubes and a spherical mirror with a diameter of 3.3m, and curvature of 6.067m which consists of 18 segment mirrors. The center of the mirror is reserved for setting any calibration items for the measurement of the distance between camera and mirrors, tuning of the mirror curvature, and gain adjustment and so on. The camera has two types of filter, an acrylic window on the camera and UV filters on each photo-tube. Details about construction, monitoring and calibration for the detector are written in Section 4.

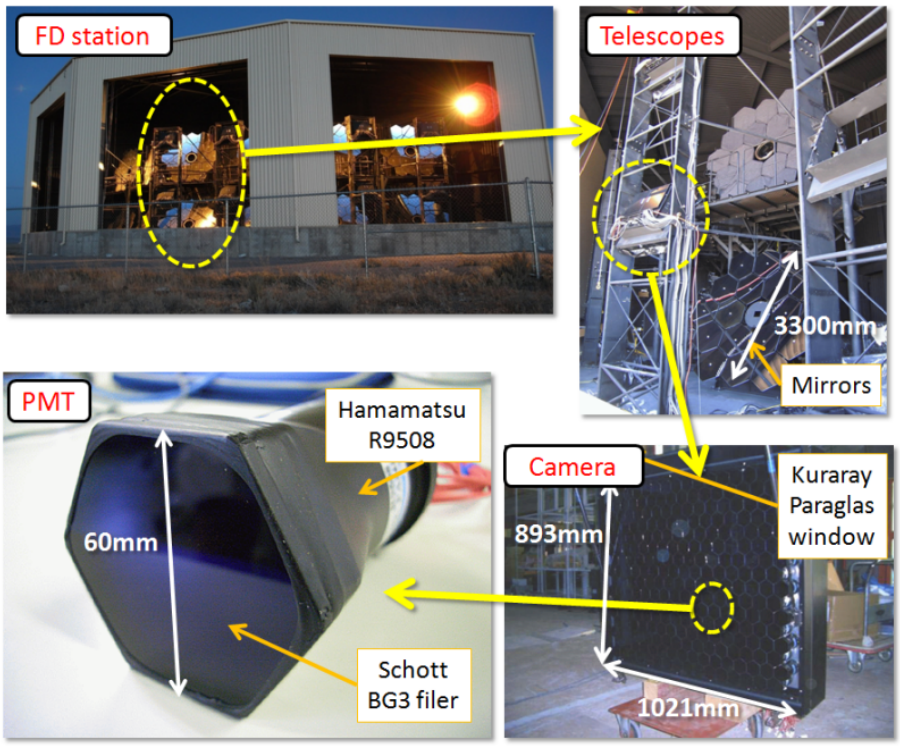

Fig. 19: Overview of the station of fluorescence detectors. It corresponds to the “Black Rock Mesa” station at the east-south of TA site.

3.2.2 Trigger and DAQ system

The trigger electronics of the southern two FD stations (BR and LR) consists of three types of VME electronics module: Signal Digitizer/Finder(SDF), Track Finder(TF) and Central Trigger Distributor (CTD). The schematic view of these modules is shown in Fig. 20

The SDF module is the signal digitizer and signal finder[32]. One SDF module processes 16 input channels and 16 modules are installed for each camera with 256 PMTs. Output signals from PMTs which pass through a DC-coupled pre-amplifier are continuously digitized by FADC on SDF with 12bit and 40MHz sampling. Since each of 4 consecutive bins is combined to 1 bin in this module, it works as 14bits and 10MHz sampling digitizer (100ns/bin). The dynamic range depends on the characteristics of pre-amplifier and shows about 7K photo-

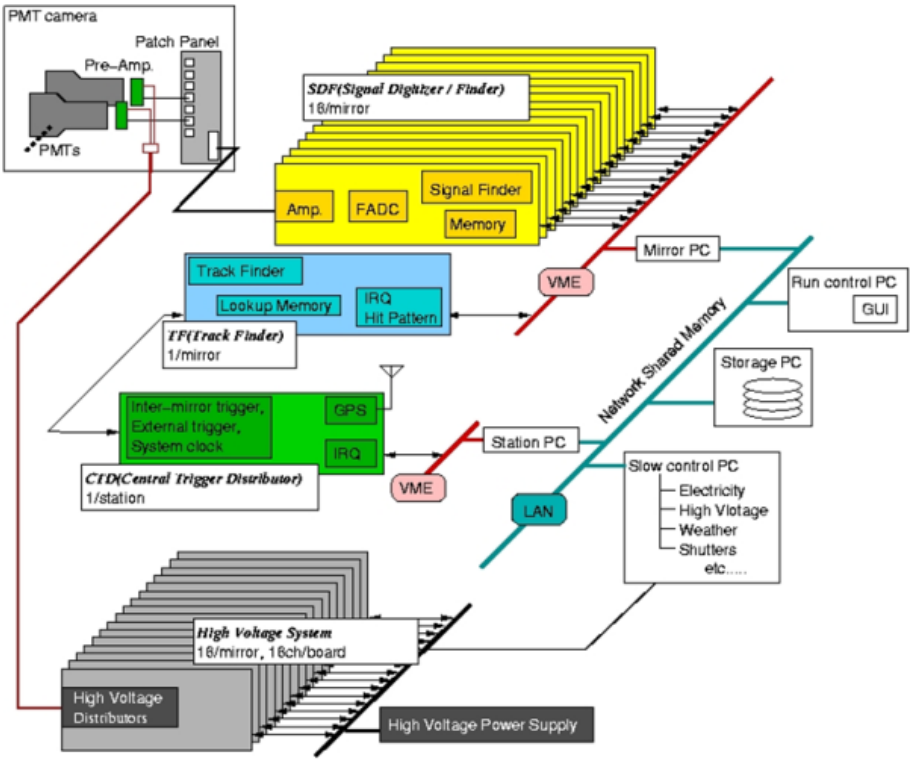

Fig. 20: Schematic view of FD DAQ modules.

electrons with the conversion factor which is 2.27 count per photo-electron. The recorded waveforms are sliced into a frame of 25.6μs with overlap of 12.8μs between adjacent frames. For each frame, SDF module calculates Signal to Noise ratio (S/N) for the four time windows (1.6, 3.2, 6.4 and 12.8μs) to find the fluorescence signals. SDF modules continuously keeps four mean/dispersion of 2^{14} bundles which are combined to 16 bins as the background information at the times 0ms, 16ms, 53ms and 79ms ago. If the S/N ratio which is calculated using background information 0ms ago exceeds the pre-determined threshold, SDF generates an alert to the TF modules as Level-1 trigger. Typically, the trigger rate is about $\simeq$3Hz at the 6 sigma threshold level. The example of digitizing and finding of SDF is shown in Fig. 21

One TF module is used for one camera as the track finder. The TF module collects the Level-1 trigger from all 256 PMTs of the camera via the 16 SDFs and search for the track by pattern matching on the camera[33]. The TF scans over hit map identified by SDF within 25.6μs in subarrays which consists of 5$\times$5 PMTs by each frame. If a hit map of the subarrays which moved on all the cameras in one station is matched to the prepared pattern in the look-up tables of TF, TF generates the alert to CTD as the Level-2 trigger with “complete track“ code (Fig. 22). An additional trigger condition is also implemented in TF to recognize the short track with straddled two cameras. These partial tracks are identified if there are three adjoining PMTs above threshold in 4$\times$4 sub-matrix at the boundaries of two adjacent cameras(Fig. 23).

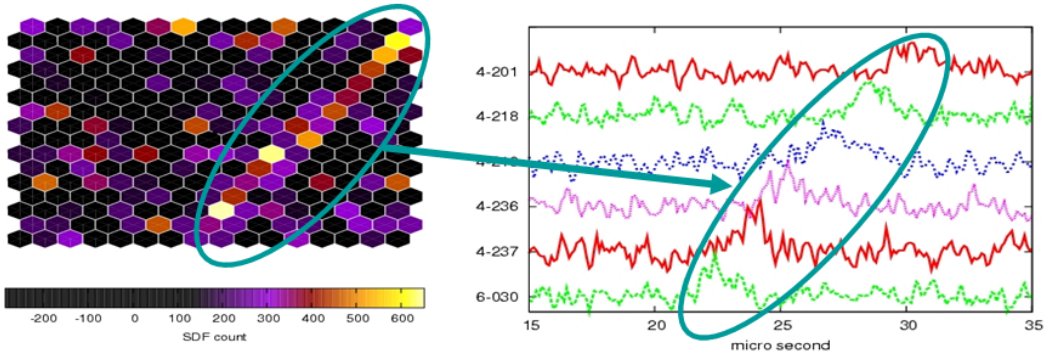

Fig. 21: The example of SDF signal finding and digitizing. The left figure shows the event display of a camera with weak signal where the colors shows the timing. The right figure shows the digitized signals. SDF recognized these weak signal.

This condition is equivalent to the complete track condition since there is an overlap of one PMTs in fields of view of neighboring cameras. In this case, the TF sends the Level-2 trigger with ”partial track“ code to CTD. There is an other additional trigger condition that SDF finds significantly large signals. If TF gets this condition, it sends the Level-2 trigger with ”non-conditional(NC)“ trigger to CTD for calibration runs.

The CTD module works not only for the Level-3 (final) trigger judgement but also for the distribution of the system clock obtained by GPS for keeping all of the SDFs and TFs synchronized[33]. The GPS modules are the same as the ones used for SD (Motorola M12+). Thus it is expected that the difference of time stamp between SD and FD is small. When CTD receives Level-2 trigger with ”complete track“ code from one or more TFs, it generates and distributes a Level-3 trigger to all TFs for recording the waveform data of all PMTs in the station. If received Level-2 trigger has ”partial track“ code from two neighboring TFs or ”NC“ code, CTD also generates the Level-3 trigger. At the moment of the generation of the Level-3 trigger signals, the CTD and TFs send the flag for each VME control PC to start a DAQ cycle.

The acquired time for the DAQ cycle, from the beginning of the signal finding process to the end of data transmission into readout buffers is less than 12.8μs corresponding to the frame length. It is dominated by the time for the track finding process and transmission of trigger information between modules. If the readout buffers of SDFs and TFs are full, CTD suspends trigger distribution and records these periods as the dead times in operation.

TFs and CTD also works for the ”air plane veto“. Sometimes air-planes fly on our observation site with visible light as noise. Since time width of that light from an air-plane is clearly longer than fluorescence’s one, it can be identified easily. If TF is triggered continuously between 8 frames, it judges the event as the air-plane event and sends the information to CTD. CTD stops the DAQ cycle until continuous triggers from the TFs stop. This period is also recorded as the dead time by CTD.

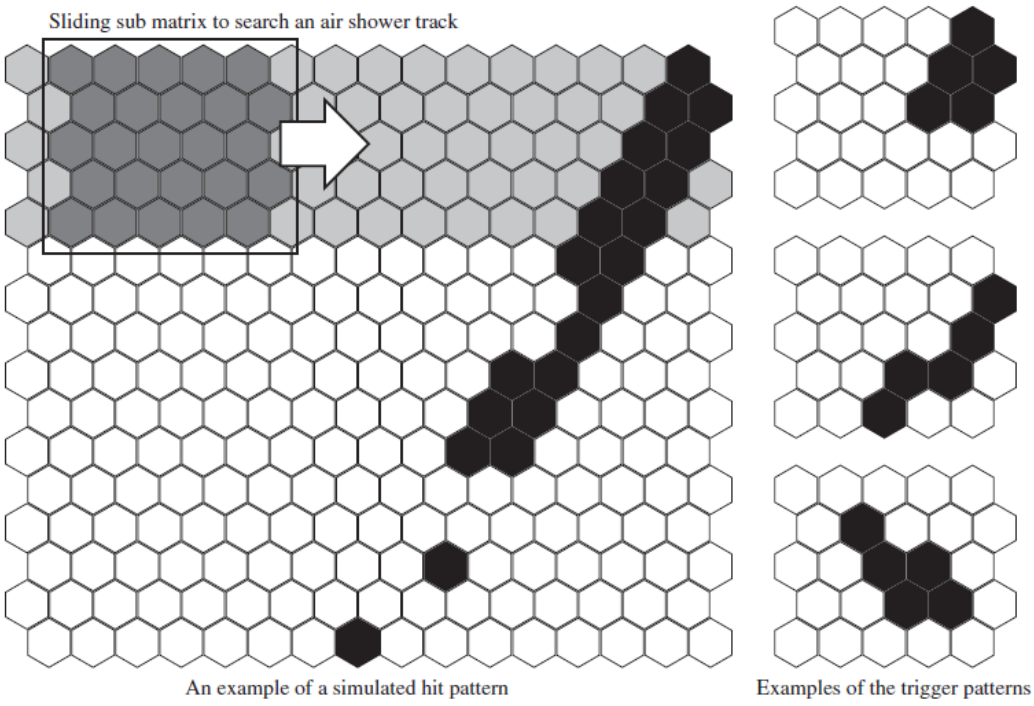

Fig. 22: The schematic view of the track finding at the TF for the complete track.

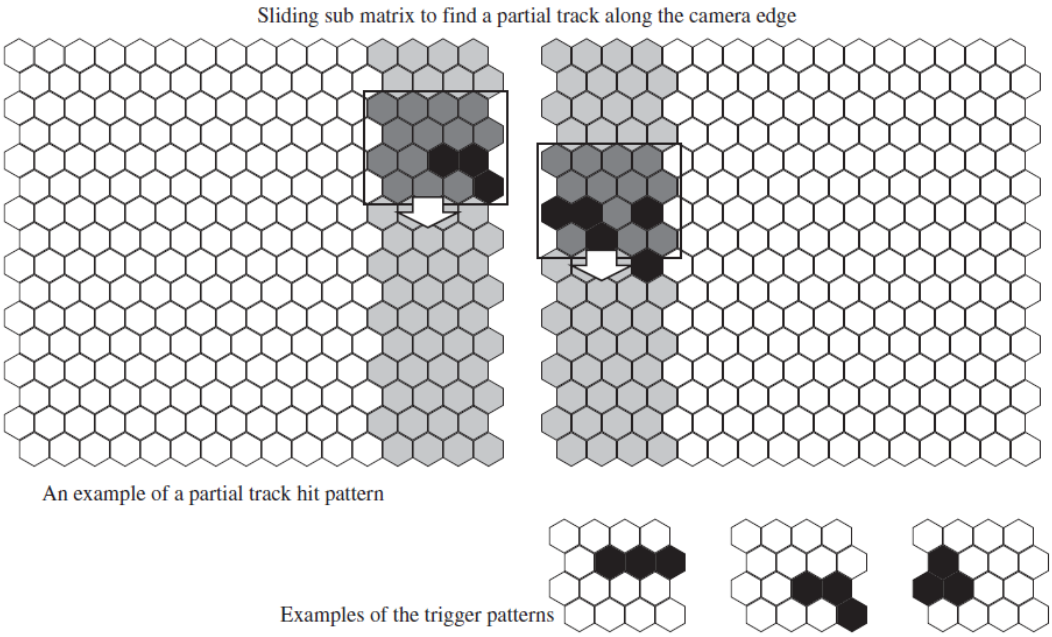

Fig. 23: The schematic view of the track finding at the TF for the partial track.

4 Calibration for the Fluorescence Detectors

For precise measurement of UHECR properties, the efficiencies of telescope optics, mirror reflectance, filter transmission, photo-tube quantum efficiency and electronics sensitivity have to be understand. The overview of the FD is shown in Fig. 19. Here we describe how we calibrate the mirror reflectance and optical filter transmittance of the cameras which are measured using a spectrophotometer, and absolute gains and uniformities of the tubes which are measured and monitored hourly for each camera with a tiny stable light source and a Xe flasher as a uniform light source. Moreover the calibration for the non-uniformity of photo-cathode sensitivity measured by a large XY stage attached to a camera window is reported. In this section, the measurement and analysis of the above-mentioned value are discussed. The details can be found in the other papers[34][35].

4.1 Mirror reflectances

A mirror of TA FDs is the spherical mirror with a diameter of 3.3m which consists of 18 hexagonal segment mirrors (Fig. 19). Each segment mirror is selected with a condition of the spot size at the focal plane less than 30mm. We have the spectral reflectances for all the segment mirrors above 250nm in wavelength measured by the production company (SANKO SEIKOJYO Co.). Moreover, the reflectances are measured and monitored regularly with a spectrophotometer (KONICA MINOLTA CM-2500d). The overview of this spectrophotometer is shown in Fig. 24. A handling of this spectrophotometer is easy because it has a compact (w69mm$\times$h96mm$\times$d193mm) and light weight (670g excluding the battery) body. However, the minimum of wavelength of the sensitive range is 360nm. Therefore, the data measured by the company is used as an absolute spectral reflectance, and their time variations and degradations are monitored as relative reflectance.

At the time of installation of the mirrors, the reflectances for all the mirrors are measured in order to know an individual difference (Fig. 25). While the maximum difference is about 5%, almost all the mirrors are within $\pm$1% difference. Until June 2008, the mirror reflectances only for lower mirrors are monitored every half a year.

One of the result of the measurement in June 2008 is shown in Fig. 26. The variation depends on the height of the segment mirrors. The lowest three mirrors in the lower telescopes show about 10% decrease after installing. In this case, since the total effect of this variation is decided by the averaged reflectance of all segment mirrors, detected photons at the camera is decreased by about 5%.

Then, in July 2008, all mirrors were washed with pure water and the reflectances were measured before and after washing. After this, we have decided to monitor the reflectances for the same 4 telescopes of each station every one or two months. Fig. 27 shows the time variation of the averaged mirror reflectances for each layer of lower telescopes at the LR station. Here

the spectrophotometer has 1% systematic fluctuation for each measurement. The magnitude of degradation depends on the height of the mirrors, and that is about 3% every half a year for the lowest layer and less than 1% every half a year for the highest layer.

The absolute spectral reflectance for every mirror is calculated with an individual difference (Fig. 25) and its time variation(Fig. 27) and an absolute reflectance at its production. Fig. 28 shows an example of spectral reflectance for a telescope. The systematic errors of the measured reflectances are estimated to be about 3% by considering the systematic uncertainty on the spectrophotometer and interpolation of time variations.

Fig. 24: The spectrophotometer for measurement of the mirror reflectance (KONICA MINOLTA CM-2500d).

4.2 Transmittance of the UV filters on the photo-tubes and the camera

As important optical components, TA FDs have two types of optical filters. In order to reduce incident night sky background light, a UV transparent filter (SCHOTT BG3) with 4mm thickness is mounted on each photo-tube. On each camera, there is a UV transparent acrylic panel (KURARAY PARAGLAS-UV00) for protecting photo-tubes from the dust. The overview of the filters is shown in Fig. 19. The spectral transmittances of the filters and panels are measured with a spectrophotometer (HITACHI U-1100). Fig. 29 is the result for 99 UV filters measured before installations, and Fig. 30 is the result for 3 tiny fragments of acrylic panels.

Additionally, we checked the transmittance of every acrylic panel by comparing the Xe flash intensity[35] through the window with that without the window. The individual difference is smaller than 3%.

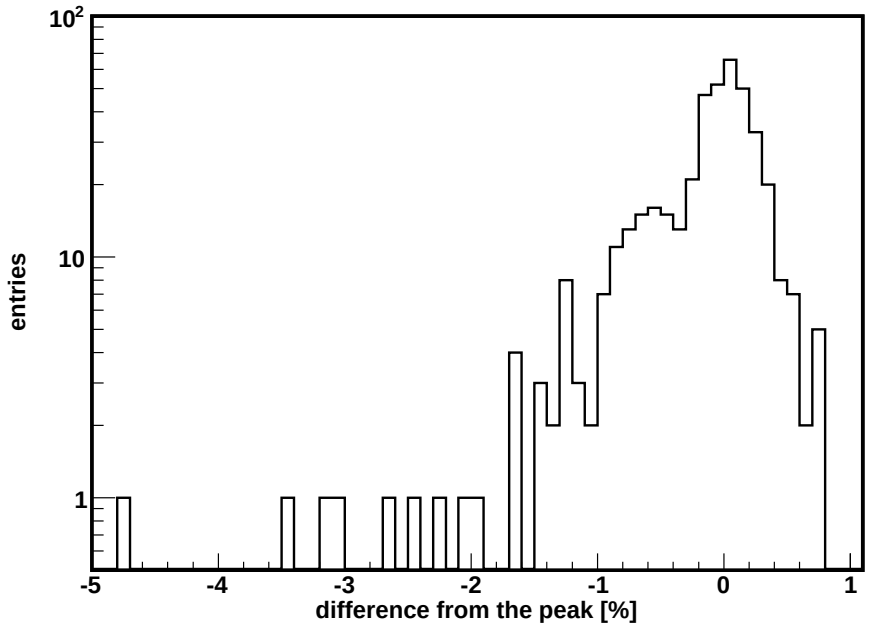

Fig. 25: The individual difference measured at the time of installation. The total number of mirrors is 432 at the BR and the LR stations. The horizontal axis shows the difference from the peak value of all mirrors.

4.3 Non-uniformity of photo-cathode sensitivity

The quantum efficiency (QE) and the collection efficiencies (CE) for several photo-tubes have been measured by HAMAMATSU PHOTONICS. Fig. 31 is the result of averaged QE for 32 samples. The measured averaged CE for five samples is $0.909^{+0.005}_{-0.002}$. In general, however, these efficiencies are not uniform over the photocathode.

The spot size of our telescope optics is less than 30mm at the focal plane. On the other hand, the photo-tube has a hexagonal photo sensitive area with 2in. diameter. Therefore, output signals of photo-tubes are affected by the non-uniformity of the sensitive area.

In order to measure the non-uniformity, we developed a large XY stage attached on the camera window (XY-scanner)[35]. This module has eight light sources which consist of UV LEDs (NICHIA-NSHU590B) with a peak wavelength of 365nm and the spot size of 4mm$\times$4mm. The schematic view of the XY-scanner is shown in Fig. 32. The number of measured points per photo-tube is about 200 with 4mm spacing.

Fig. 33 is an averaged non-uniformity map over 253 photo-tubes (excluding the three standard photo-tubes with YAP) on the camera #05 at the BR station. This sensitivity is normalized with the bins inside a circle with 36mm diameter, which corresponds to the effective area for the absolute gain calibration(Section 4.4).

HAMAMATSU PHOTONICS has also measured the non-uniformities along two orthogo-

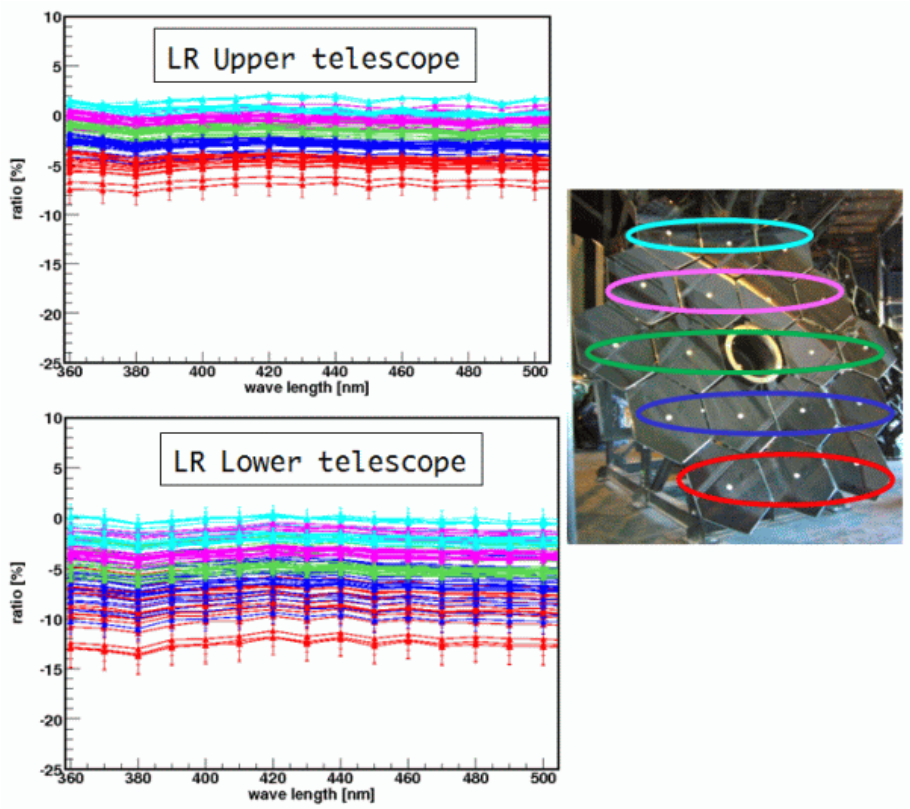

Fig. 26: The variation of the reflectances of the LR mirrors in June 2008. Colors on the left figures correspond to the colors on the right figure. The vertical axis is the variation from installing. The variation depends on the height of mirrors.

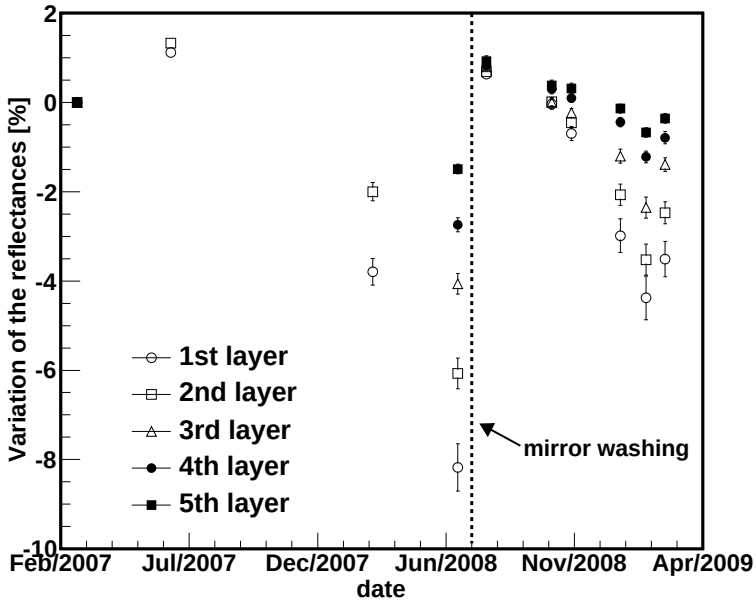

Fig. 27: The time variations of the averaged mirror reflectance for each layer of the lower telescopes at the LR station. Each data point corresponds to an average over mirrors of the same height (the 1st layer is the lowest). Open circles are for the 1st layer (lowest), and open squares, open triangles, filled circles and filled squares show the variations for the 2nd, 3rd, 4th and 5th layers, respectively. Error bars indicate standard deviations for each layer. The vertical axis is the difference from the first mirror reflectance measured at the time of installation.

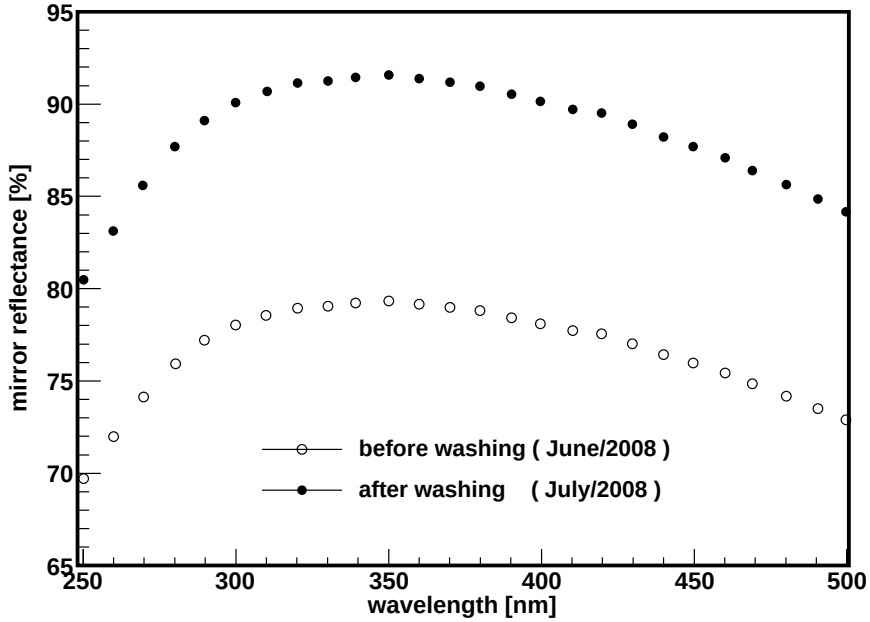

Fig. 28: The spectral reflectance of the camera #06 of the BR station. Open circles are the reflectance before washing and filled circles are after washing.

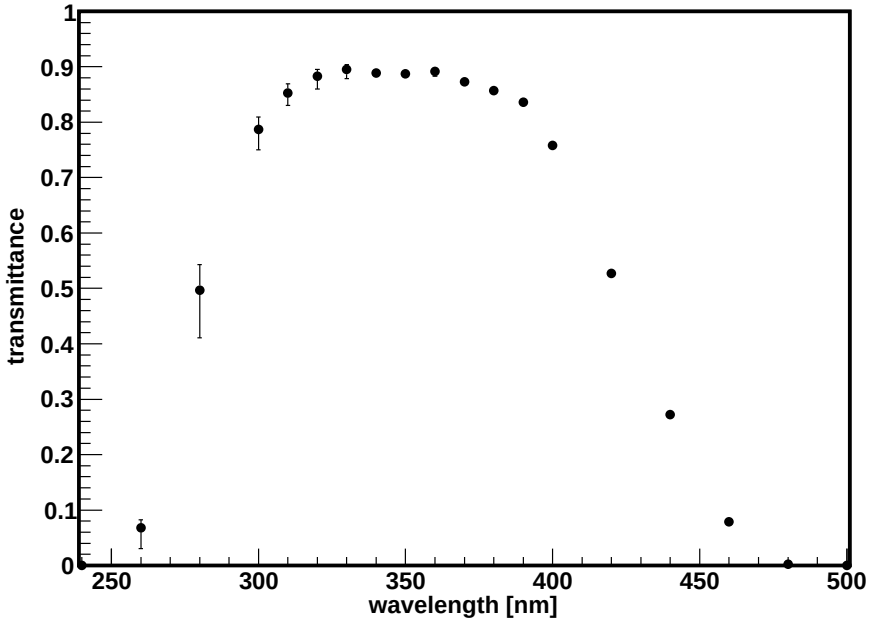

Fig. 29: A typical transmittance of the UV filter on photo-tubes. Data points are the medians for all the sampled filters with the bars corresponding to one standard deviation.

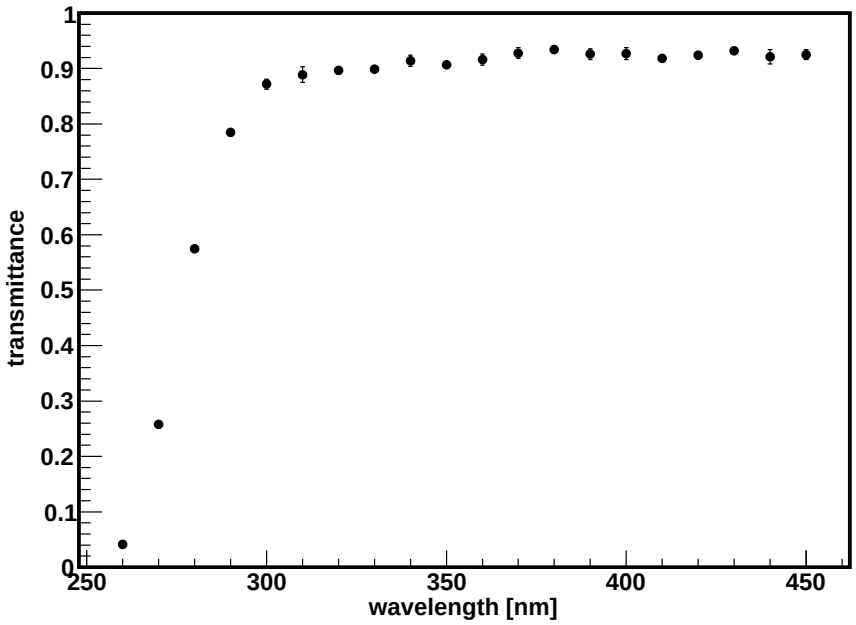

Fig. 30: The typical transmittance of the acrylic window panel on the camera. Filled circles are the median value for three samples. Error bars indicate the differences between the median and the other two samples.

nal and cross-sectional axes. Fig. 34 is the comparison between the results by HAMAMATSU and that of XY-scanner, and they are in good agreement.

4.4 Absolute and relative calibration of photo-tubes

The FD camera consists of 256 (16×16) hexagonal photo-tubes (HAMAMATSU R9508). Currently, the calibration process of photo-tube gain is divided into three steps, namely the absolute gain measurement for the standard photo-tubes, the relative gain measurement for a camera, and the correction for the temperature characteristics of photo-tubes.

In the Institute for Cosmic Ray Research (ICRR), a simple pulsed UV light calibration system called CRAYS (Calibration using RAYleigh Scattering)[36] was developed. The schematic view of the CRAYS setup is shown in Fig. 35. As the light source, a scattered photons of nitrogen laser light are used with 5% absolute intensity error with pure nitrogen gas molecules. By the system, three photo-tubes per camera are sampled, and for each sample the absolute relation between the number of injected photons of 337.1nm and the sum of the ADC counts by the electronics used in TA FDs are recorded as the conversion factor. It should be noticed that the measured absolute response by CRAYS includes the transmittance of UV filters, and effective photo-cathode area is limited within the circle with a diameter of 36mm by a light buffer.

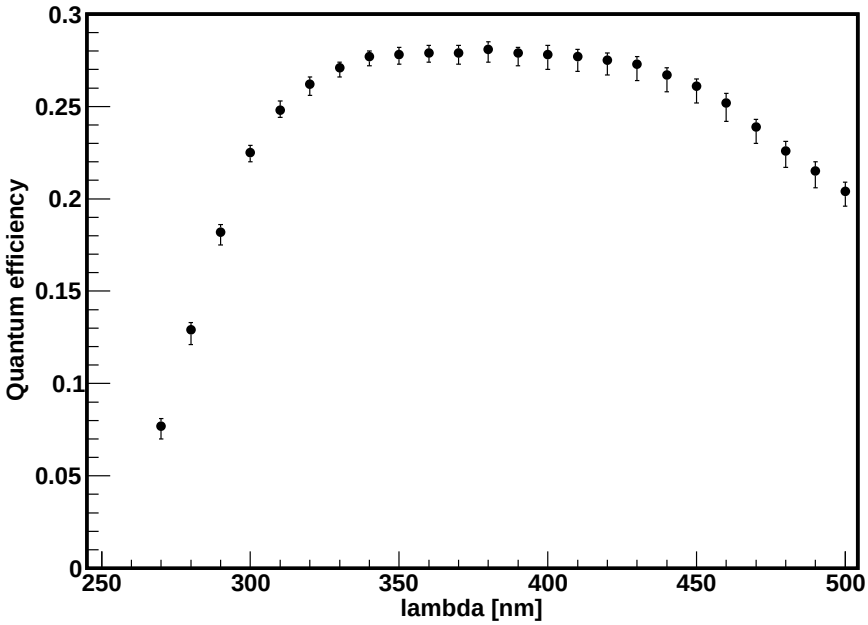

Fig. 31: The typical quantum efficiency of photo-tubes. The data point shows the median with 1 σ error bar of all the photo-tubes measured by HAMAMATSU PHOTONICS.

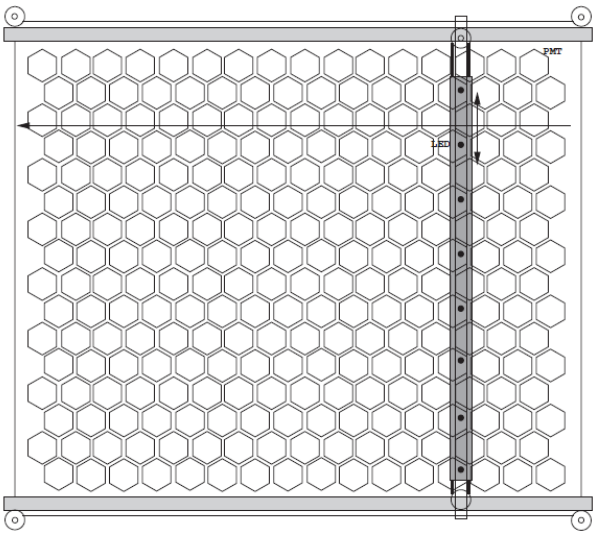

Fig. 32: The schematic view of the XY-scanner.The covering area of each LED is 2.5 PMTs vertically and 16PMTs horizontally.

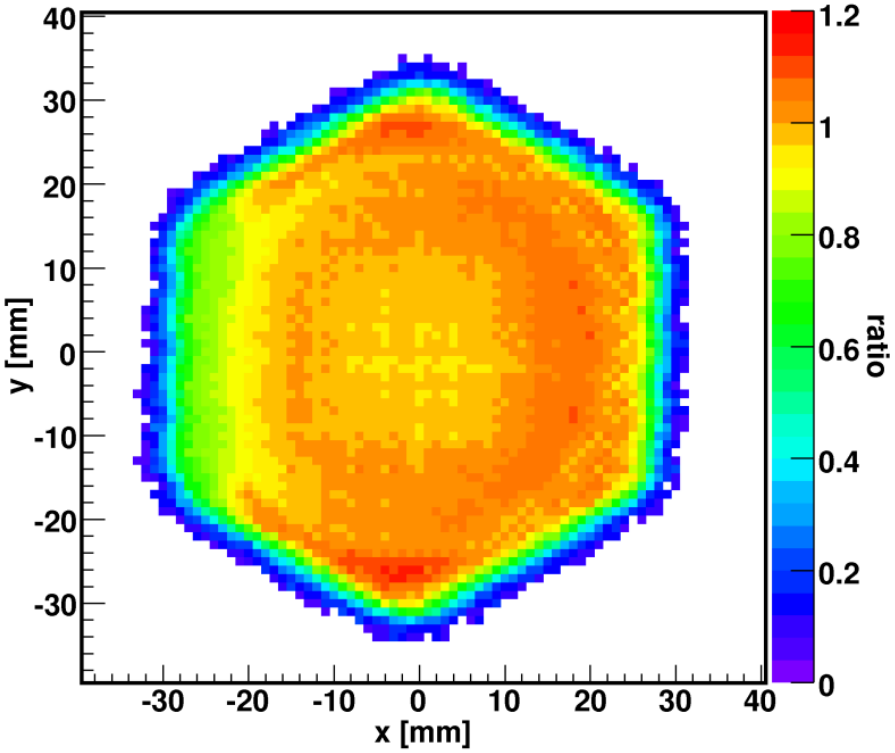

Fig. 33: The typical non-uniformity map with 1mm×1mm resolution of the photo-cathode of our photo-tube. The non-uniformity map is normalized with the bins inside a circle with 36mm diameter. The obtained map shows an asymmetry along the x axis. It is caused by the dynode structure of the PMT.

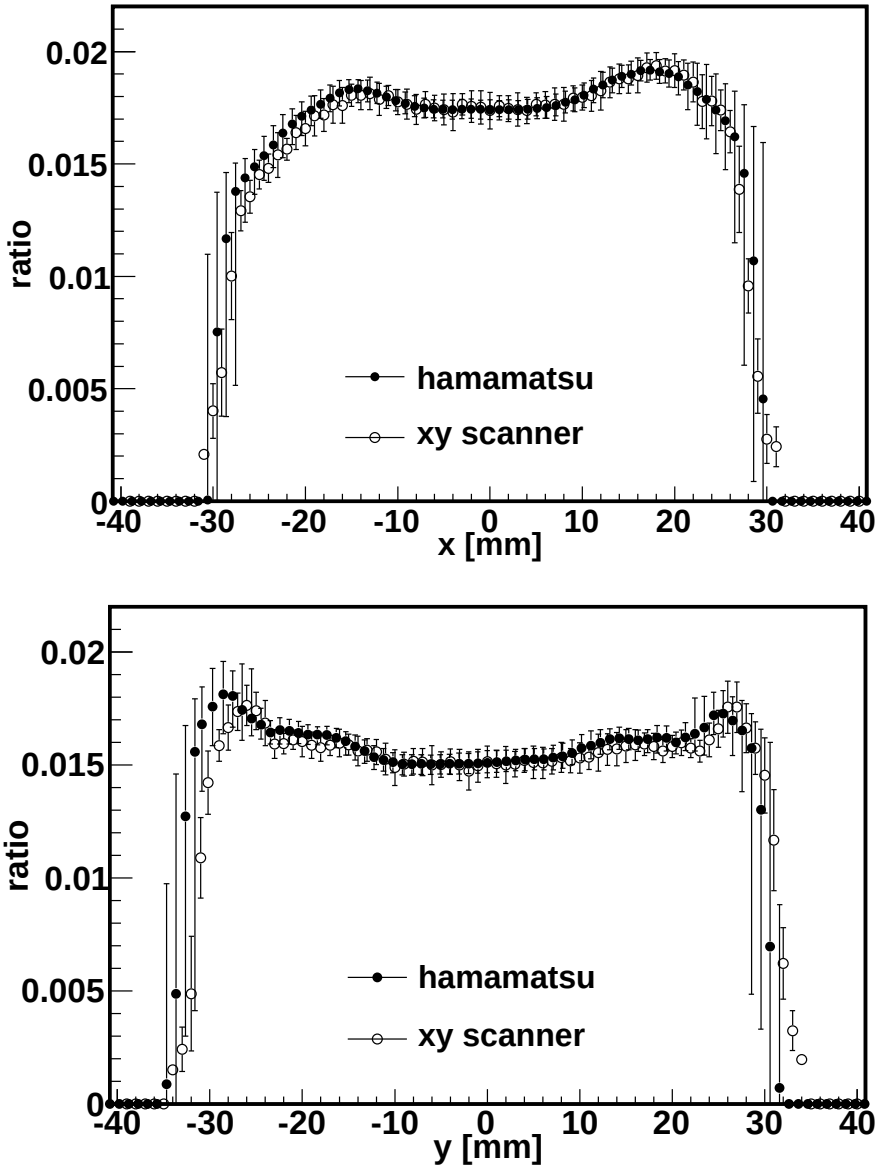

Fig. 34: The result of the comparison of HAMAMATSU data with the data measured by XY-scanner. Upper and lower figures correspond to the differences measured along X axis and Y axis, respectively.The definition of the coordinate of x and y axis is the same as Fig. 33. Filled circles are the HAMAMATSU data, and open circles are XY-scanner's.

This photo-tube with calibrated absolute gain is used as a standard photo-tube and it is monitored hourly by a tiny stable light source called YAP pulsar. This is a UV pulsed light source with a diameter of 4mm and a height of 2mm consists of a 50 Bq alpha-ray sources (Am^{241}) and a YAP scintillator ($YAIO_3$:Ce). The temperature dependence of an intensity is about -0.2 % / degree from -10 to 40 $^{\circ}$C [37]. Each standard photo-tube has this pulsar on the center of photo-cathode, and its gain is regularly monitored by comparing outputs with the YAP pulsar intensity. The typical intensity is equivalent to 450p.e. with a fluctuation of 10% and an individual difference of 5%. The relation between the absolute gain and the intensity of the YAP pulsar is also calibrated by CRAYS for all of the standard photo-tubes.

The uniform light source called Xe flasher is mounted on the center of each mirror, and it is faced to the camera center. The schematic view of the Xe calibration is shown in Fig. 36. Xe flasher, which consists of Xe lamp and diffuser, emits pulsed photons with an intensity equivalent to 2×10^4p.e. and a width of 2μs. We adjusted the gains of all of the photo-tubes to these standard photo-tubes, and we monitored once per hour during observations with the Xe flasher. The standard deviation of the adjusted relative gains for each camera is about 1%[35].

In general, responses of the photo-tubes and the pre-amplifiers depend on temperature. We prepared a measurement system for temperature characteristics for photo-tubes, the pre-amplifiers and YAP pulsars. Several standard photo-tubes were tested, and the typical measured temperature coefficient of the photo-tubes including that of pre-amplifiers is about -0.7% / degree [37]. Moreover temperature of each camera is measured every minute with a thermometer mounted in each camera box. Therefore, we correct temperature effects for all the observation terms.

Currently, we calculated the absolute gains for all the photo-tubes with the measurement of absolute and relative gains and temperature coefficients. Fig. 37 shows an example of the averaged absolute gains for 256 photo-tubes in camera #06 of the BR station in March 2008.

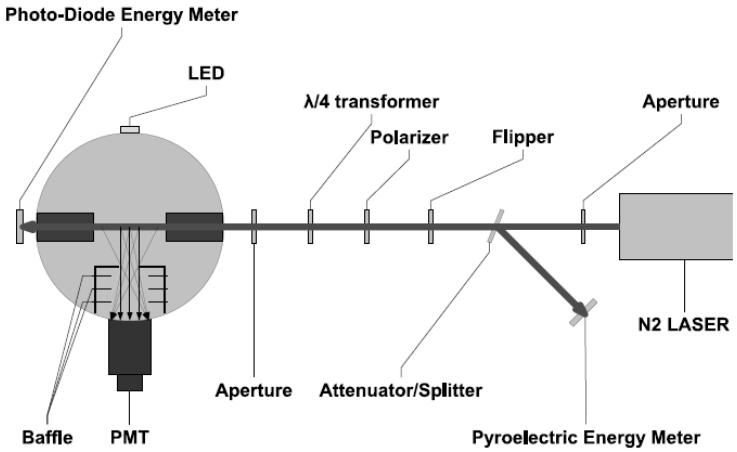

Fig. 35: The setup of the CRAYS measurement[36].

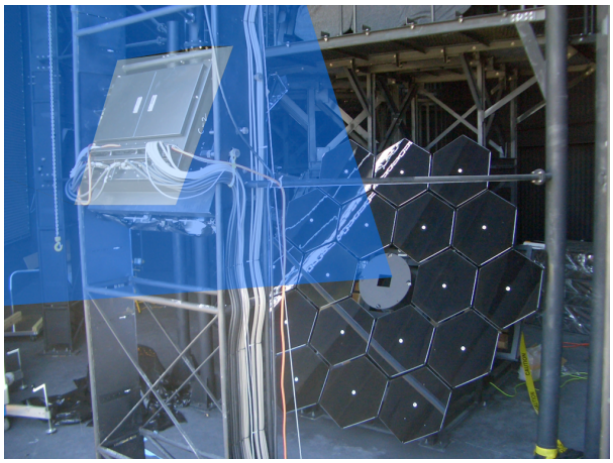

Fig. 36: The schematic view of the Xe calibration. The Xe flashers was set on the center of the mirrors for each telescope. The uniform light is detected by the each PMTs on the camera for the adjustment of the relative gain of each PMT.

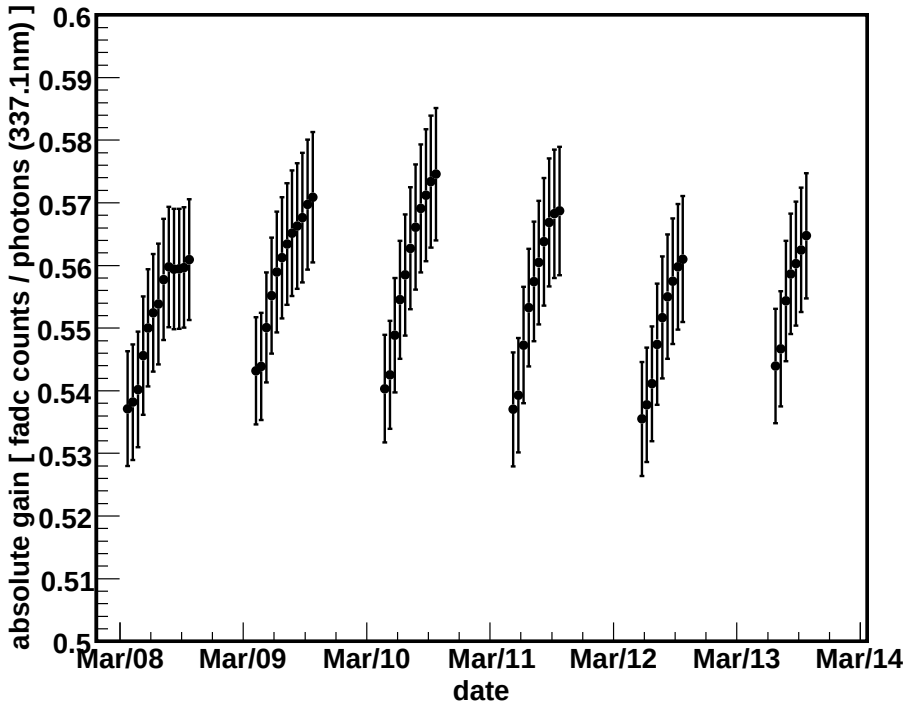

Fig. 37: The hourly variation of absolute gain in March 2008. Filled circles are averaged gains for 256 photo-tubes in camera #06 of the BR station. Error bars are the standard deviations for 256 photo-tubes. In this observation term, the temperature of the camera was changing from 24 degree to 7 degree in each day.

4.5 Atmosphere

In this section, the method how to measure the atmosphere is discussed. There are three items for using the FD analysis:

- Atmospheric parameters
- Transmittance
- Cloud

The atmospheric parameters such as temperature, pressure and humidity are used for estimation of the yield of the fluorescence light and the transmittance by the Rayleigh scattering. Those parameters are measured by the radiosonde (Section 4.5.1).

Since the transmittance of the atmosphere affects the reconstructed energy directly, this is one of the most important calibration. The main uncertainty of this measurement is caused by the Mie scattering. Since it depends on the time, the transmittance has to be measured frequently. In the hybrid analysis, the result of the LIDAR measurement is used (Section 4.5.2).

The aperture of the FD is affected by the cloud. There are two methods to measure the amount of the cloud; the weather code (WEAT code) visually recorded by the operator in the MD station and the pictures taken by the IR camera at the BR station. In the hybrid analysis, the WEAT code is used for the analysis. The details is described in Section 4.5.4.

4.5.1 Radiosonde

The atmospheric parameters such as pressure, temperature and humidity are important for the FD analysis. These parameters are used for the calculation of the fluorescence yield, atmospheric depth, transparency of the atmosphere and so on. Since the atmosphere is changed by time, these parameters have to be measured periodically. For the demand of the high altitude measurement, the measurement is done by the balloon, up to an altitude of about 30km. There are six launching sites for the radiosonde around the TA site by meteorological instrument. At each site, the characteristics of the atmosphere are measured every 12 hours and they are opened to the public at the web site[38]. In this analysis, the atmospheric parameters measured by ELKO site (40.87N, 115.73W) are used. All of the data are prepared as the database to use for the analysis. The detailed study for the radiosonde is written in [39].

4.5.2 LIDAR

For the measurement of the attenuation in the atmosphere, the TA experiment has laser system called LIght Detection And Ranging (LIDAR) which is located 100m far from the BR station. It consists of the YAG laser with 355nm wavelength, 4mJ power and 1 Hz frequency,

Fig. 38: The overview of the LIDAR system.

and a 30cm-diameter telescope on the steerable mounting and a PMT with a UV filter. The remote operation can be done from the FD station. The overview is shown in Fig. 38.

The atmospheric attenuation is measured using the photons that return from the shooting laser. The photons are detected by the PMTs with the telescope and digitized by the oscilloscope. The LIDAR system operated before and after observation with 4 types of measurement: 500 vertical shots and 500 horizontal shots with two types of energy. The details of the operation and analysis are written in [40].

The atmosphere has two main components for the attenuation: the molecules in the atmosphere and aerosols. The scattering phenomenon caused by a molecule is called Rayleigh scattering. It is expressed well by atmospheric parameters (temperature and pressure). So the important things for measurement of the atmospheric attenuation is the attenuation caused by aerosols, called Mie scattering. This system can measure the total attenuation for the atmosphere. The component of the Rayleigh scattering can be calculated by the atmospheric parameters measured by Radiosonde. So the component of the Mie scattering can be obtained by the measured total attenuation subtracted by the calculated attenuation for the Rayleigh scattering.

This system measures the extinction coefficient α, the inverse of the attenuation length, for each height for every observation term. The data obtained by the horizontal shots can measure the extinction coefficient on the ground. The distribution of the attenuation for the component of the Mie scattering is shown in Fig. 39. The typical attenuation length on the

ground is 29.4km. For the index of the attenuation, we define the Vertical Aerosol Optical Depth (VAOD) τ_A as:

$$T_{Mie} = \exp(-\tau_A), \tag{46}$$

where T_{Mie} is the transparency by the Mie scattering. The distribution of the VAOD is shown in Fig. 40. The median of the measured data is about 0.033.

The amount of the aerosol is reduced as the altitude increases. So the extinction coefficient $\alpha_{Mie}(h)$ at the several heights h is expressed as:

$$\alpha_{Mie}(h) = \exp(-h/H), \tag{47}$$

where H is the scale height for the aerosol distribution. This parameter can be obtained by fitting for the attenuation length on the ground and VAOD at each height. The fitted scale height is obtained for 1.0km. When the attenuation length on the ground is 29.4km and scale height is 1.0km, the VAOD at the 3.5km is 0.033 and VAOD at the 5.0km is 0.034. It shows the good agreement with the measured VAOD. The obtained values show almost the same as those of HiRes[41]. In this analysis, the typical values shown in Table. 1 are used for the attenuation of the Mie scattering.

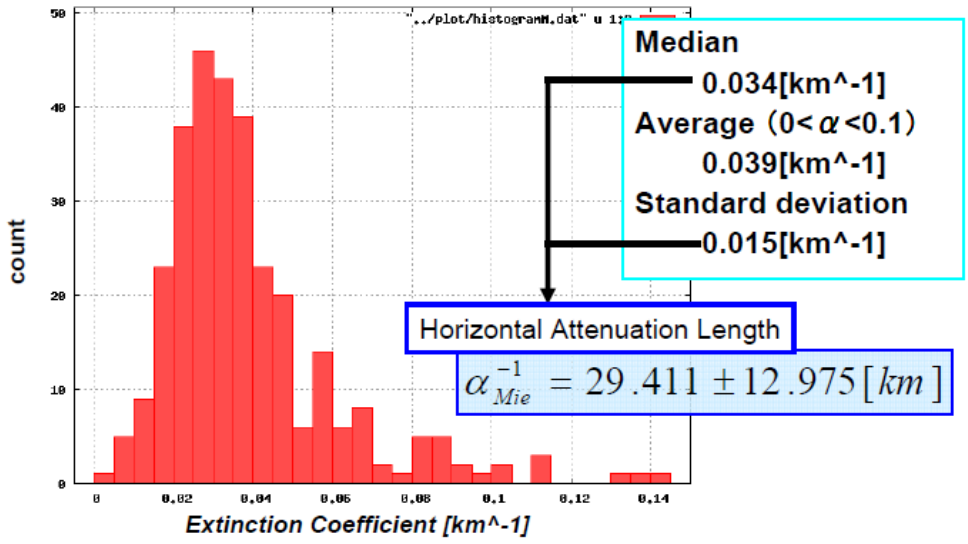

Fig. 39: The distribution of the extinction coefficient for the Mie scattering on the ground. The horizontal axis is the measured extinction coefficient and the vertical axis is the number of events. The median value 0.034 (/km) is equivalent to the attenuation length of 29.411 km.

4.5.3 Central Laser Facility

The Central Laser Facility (CLF) is located at the center of the TA site with the YAG laser with 335nm wave length and 5mJ laser power as the calibration light source. It shoots the

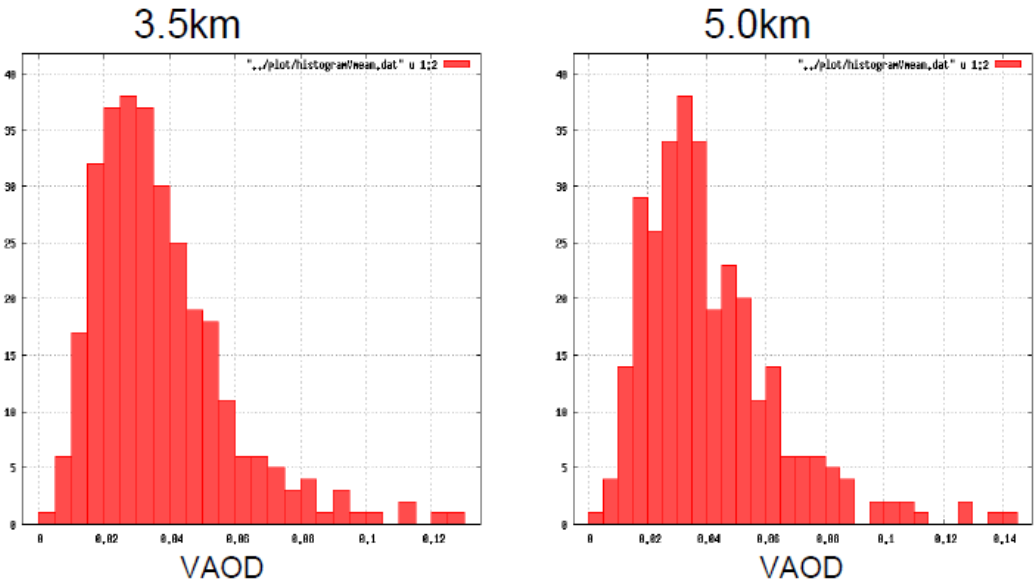

Fig. 40: The distributions of the VAOD. The left figure is the VAOD at 3.5km height and the right figure is the VAOD at 5.0km height. The horizontal axis is the VAOD and the vertical axis is the number of events. The medians of these distributions are 0.033 at 3.5km and 0.038 at 5.0km.

Items	Values
Extinction coefficient on the ground	0.034 ± 0.015 /km
Attenuation length on the ground	29.4 ± 13.0 km
Scale height	1.0 km
VAOD at the 3.5km above ground level	0.033 ± 0.012

Tab. 1: The typical attenuation parameters for the Mie scattering.

laser to the vertical direction during observation every 30 minutes. The overview of the CLF is shown in Fig. 41. The detailed information is written in [40].

It measures the atmospheric attenuation same as LIDAR and becomes the calibration light source to measure the relative gain of the stations. The distances of the CLF from the three stations are same (20.85km). For the comparison of the detected signals in three stations, the relative gain is measured.

The characteristics of the CLF as the atmospheric monitor is the frequency of the operation. The measurement by the LIDAR is operated only before and after the observation. On the other hand, the CLF is operated every 30 minutes in the observation. So the CLF data are used for the relative calibration of the atmosphere with better time resolution.

The analysis of the CLF data is not finished yet. In future, we will use it as the calibration light source for the atmospheric and gain monitor.

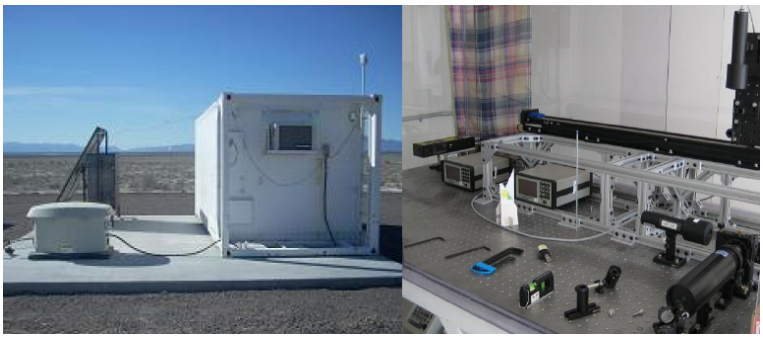

Fig. 41: The left figure is the overview of the CLF system. The right figure is the view in the CLF container.

4.5.4 Cloud monitor

In the FD observation and analysis, the cloud is important for calculating the aperture and reconstructed energy. In the TA experiment, there are two types data for cloud. One is the weather code visually recorded by the operator (WEAT code) at the MD station. The other is the sky pictures taken by IR camera at the BR station. In this analysis, since the analysis of IR camera is not finished, only the WEAT code is used for the quality cut of the observed data.

WEAT code

As part of the weather codes, an operator of the MD station is required to record the amount of cloud cover in the sky visually every one hour. The recorded code is called as the WEAT code. It has some information of the cloud: amount of the cloud in the directions of North, East, South, West and Overhead, thickness of the cloud and haze. This monitoring method is the same as that of HiRes experiment[2]. For the analysis of the BR and LR stations, the

information of the cloud of South and East are used. These codes are recorded as 0 or 1 for each. The directions of the WEAT code are shown in Fig. 42.

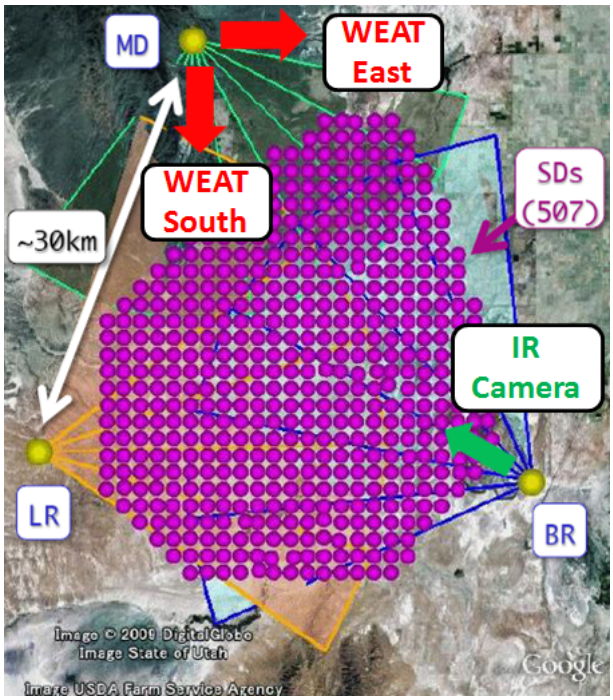

Fig. 42: The directions of the cloud monitors. The red arrows show the East and South direction of the WEAT code and the green arrow shows the center of the direction of IR camera. The purple points show the positions of 507 surface detectors and the yellow points show the three fluorescence stations (BR:Black Rock Mesa, LR:Long Ridge, MD:Middle Drum).

IR Camera

In the TA experiment, the IR camera (Avio TV S-600) which is sensitive in a wavelength range of 8 $\sim$ 14 μm is used near the LIDAR. This camera measures the temperature in a field of view 25.8° $\times$ 19.5° and digitizes in 320 $\times$ 236 pixels. The camera is mounted on the steering stage. The IR camera is operated every hour, and in one sequence it takes 14 pictures. Twelve pictures correspond to the direction of the 12 telescope in the BR station. Others are the horizontal and vertical view.

In the data analysis, each IR picture is divided into 4 segment pictures in the vertical direction and categorized by the score from 0 or 1 for the cloud information by using temperature information. So each picture has the score from 0 to 4. The score of 0 means the clear sky and the score of 4 means mostly cloudy. The details for this analysis are written in [42]. The examples of the taken pictures and scoring are shown in Fig. 43.

The analysis of the IR camera is not finished yet. In future, the quality cut of the cloud will

be updated by using the IR camera information.

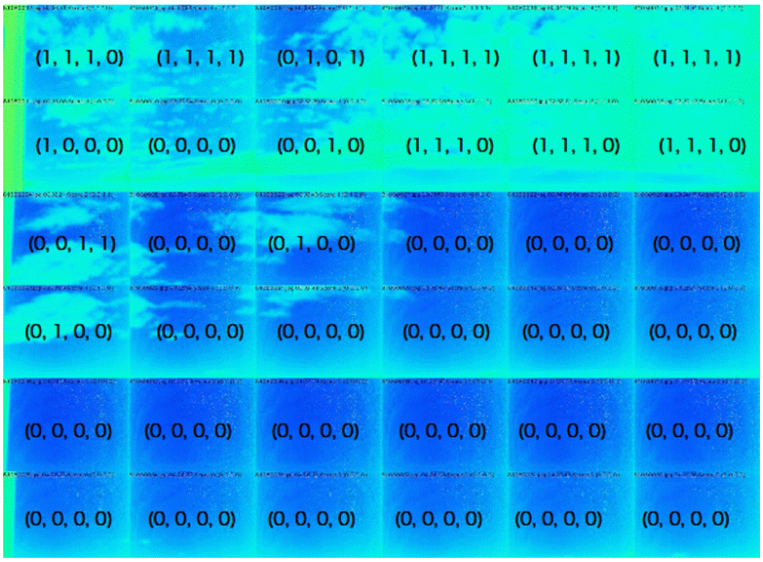

Fig. 43: The examples of the taken pictures by IR camera and scoring for the cloud information. The numbers on the pictures correspond to the categorized score. Each two layer which has twelve pictures is taken by one observation of the IR camera.

4.6 End-to-end calibration by accelerator

For the analysis of FD, many calibration constants, such as the amount of emitted photons by energy deposit and dependence of atmospheric parameters of fluorescence yield, atmospheric transparency, mirror reflectance and PMT gain have to be used. Each component has measured accuracy, and the systematic errors of the calibration constants are integrated. Then the total systematic error becomes large. For the verification of this issue and towards smaller total systematic error for energy measurement, the end-to-end calibration is useful. The CLF can be used as the total calibration method, but it excludes the fluorescence yield. So a compact linear electron accelerator was constructed for the end-to-end calibration method which includes the effect of fluorescence yield. The accelerator is called the Electron Light Source(ELS). The specification of ELS is shown in Table. 2

The ELS was installed 100m away from the BR station. Therefore, it cannot calibrate the atmospheric transparency because the attenuation factor of fluorescence photons is about 1% for a distance of 100m. So ELS calibrates the fluorescence yield and the components of the detector by the end-to-end method. Since the vertical field of view of telescopes is from 3° to 33°, the maximum height of field of view at the 100m distance is equivalent to 57m. The simulated beam development in the atmospheric is shown in Fig. 44. The telescope sees the brightness area. The total energy of 10^9 electrons with eneargy of 40MeV (=4×10^{16}eV) at

Beam energy	$\sim$ 40MeV
Output current	$10^9 e^-$/pulse
Beam intensity	6.4J/pulse
Pulse width	1μs
Repetition rate	1Hz

Tab. 2: The specification of ELC.

the distance of 100m is equivalent to about 10^{20} eV air shower at 10km. By this calibration, we obtain the conversion factor from energy deposit calculated by Geant4[43] simulation to obtained FADC counts at the telescope.

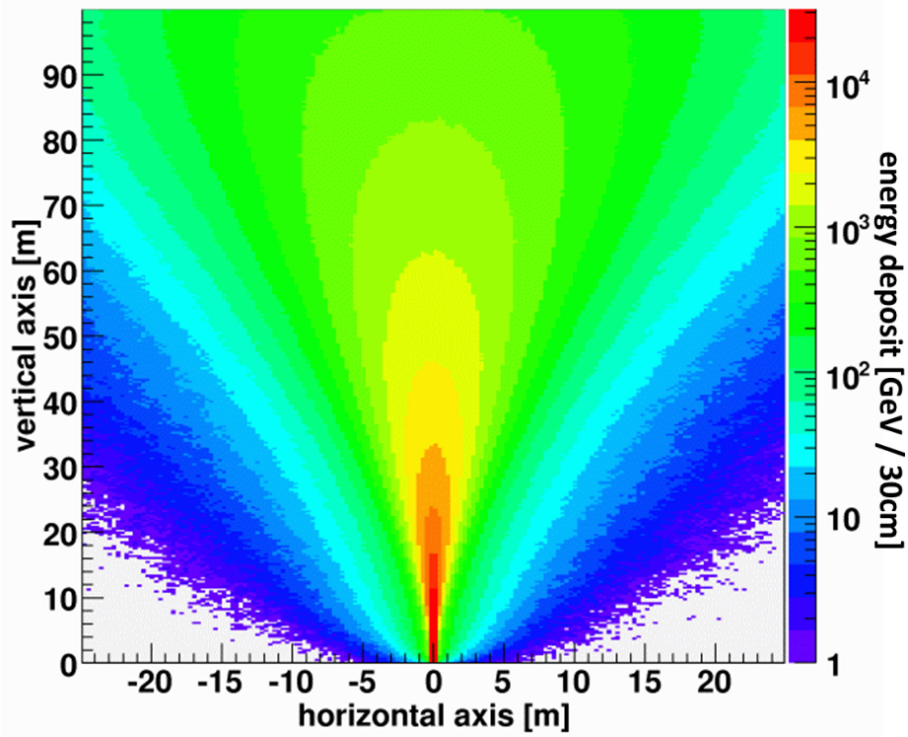

Fig. 44: The ELS beam development in the atmosphere which is simulated by Geant4[43] simulation. The colors show the energy deposit at each point.

The construction of the ELS was finished at the High Energy Accelerator Research and Organization (KEK) in Japan. The overview of the ELS is shown in Fig. 45. It mainly consists of 100kV electron gun, bunching unit, 2m accelerating tube, 90° bending magnet and some focus magnets. The details of the design are written in [44]. The ELS was already transferred to the experimental site of Utah and started the preparation for shooting the beam in the atmosphere. The first beam will be shot in the Spring of 2010.

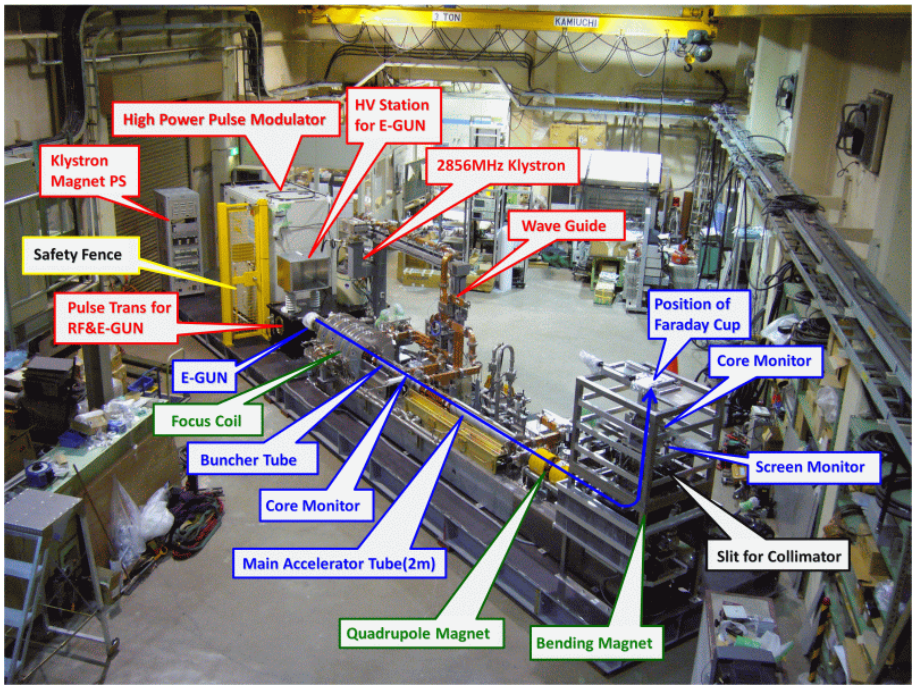

Fig. 45: The overview of the ELS at the KEK in Japan.

5 Overview of the hybrid analysis

In this thesis, the performance of the developed hybrid reconstruction and the energy spectrum above $10^{18.7}$eV measured by the hybrid technique are presented. In this section, the following items are discussed as the overview of the hybrid analysis:

- Traditional monocular FD reconstruction
- Merit of the hybrid analysis by comparing with the FD monocular analysis
- Data set
- How to use the MC simulations

The basic principle of the developed hybrid reconstruction is to improve the traditional FD analysis by requiring SD timing information. The schematic diagram of the traditional FD analysis is shown in Fig. 46.

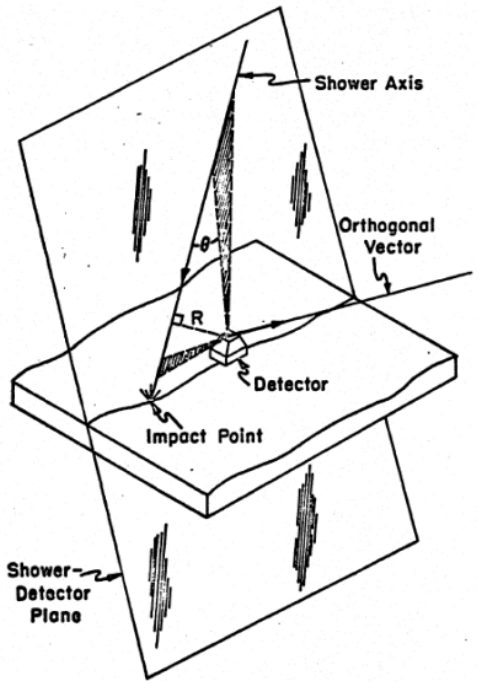

Fig. 46: The schematic diagram of the observation and reconstruction of an UHECR by a monocular FD.

The basic idea of the energy measurement by the FD is that the number of the emitted fluorescence photons along the shower axis is proportional to the deposited energy. The sum of the energy deposited in the atmosphere is not equal to the energy of the primary cosmic ray due to missing energy of the following two types: the energy deposited under the ground and

the energy of neutral particles which do not emit fluorescence light. To estimate the former, the observed longitudinal development of the shower is extrapolated underground by the fit using the Gaisser-Hillas function. The latter is estimated from the fraction of energy of neutral particles by air shower MC simulation. The integrated energy of the fit function after the correction of the missing energy becomes the energy of the primary cosmic ray.

One of the difficult points of the reconstruction by FD is the contribution of the Cherenkov light. The FD observes not only the fluorescence photons but also Cherenkov photons. The Inverse Monte Carlo(IMC) is used to consider Cherenkov photons. It estimates the longitudinal development along the shower axis by the comparison with the data and MC including Cherenkov light. The longitudinal development of the fluorescence contribution is obtained after subtracting Cherenkov contribution.

There are three steps in the traditional FD reconstruction. Firstly, the Shower Detector Plane (SDP) is determined precisely because the SDP is observed as the image on the camera. Secondly, the shower axis on the SDP is determined by the timing information from the PMTs on the camera. Thirdly, the longitudinal development is estimated by the IMC method, which is mentioned below.

It is difficult to estimate the angle of the shower axis on the SDP and the distance from the FD station by the traditional monocular FD reconstruction. These parameters are fit only by timing information. For hybrid events, SD information can be also used to improve the reconstruction of the air shower. Here the hybrid reconstruction was developed which is based on the monocular FD reconstruction by requiring timing information of one SD. The details how to reconstruct hybrid events are described in Section 7.

One of the merits of the hybrid analysis by comparing with the FD monocular analysis is that the aperture is flat for high energy events. On the other hand, the aperture by FD is increased when the energy is increased because the amount of emitted photons is proportional to the energy. The FD aperture which is not flat causes uncertainty to measure the energy spectrum. For hybrid events, the aperture is limited by SD for the energies above which the shower trigger efficiency by SD reaches 100%. For the hybrid analysis, the energy spectrum is measured using the flat aperture and the FD energy scale.

It is necessary to use the detector MC simulation in addition to air shower MC simulation to estimate the resolution of the hybrid reconstruction, to obtain the aperture, and to use the IMC method. The details of the MC are explained in Section 6. The resolution of the reconstruction and the aperture for the hybrid events are studied in Section 8.

The observation term of the data set for this analysis is from May 27, 2008 to September 28, 2009. The cloudy time is excluded by the cloud monitor data of the WEAT code explained in Section 4.5.4.

The result of the hybrid reconstruction of the data is described in Section 9. The comparison between data and MC is also shown as the verification of the treatment of data and MC. The

measured energy spectrum and its systematic error are shown in the Section 10 and Section 11.

One of the most important subjects of the hybrid analysis is the comparison of energy scale between FD and SD. Since the SD analysis is not currently ready, the comparison is not finished yet. In Section 12, the plans of the comparison and other improvements are described as the prospect of the hybrid analysis.

6 The detector Monte Carlo

6.1 Air Shower Monte Carlo

One of the problems of the Monte Carlo (MC) simulation for an air shower by UHECR is that it takes very long time for calculation because a UHECR generates too many particles. The COSMOS, a full simulation code for the air shower[45], has the solution to reduce the calculation time with accuracy, called "skeleton-flesh" method[46][47]. This code generates the air shower by tracing the each particle with all of the interaction with thinning method. For using the detector simulation, we generated air showers with several conditions and stored those data to a large database. Each shower information can be used quickly for the analysis, using detector MC for SD and FD. The conditions for the COSMOS for this analysis are shown in Table. 3.

primary energy	from 10^{18}eV to 10^{20}eV
zenith angle	from 0.65 to 1 in $\cos\theta$
Primary particle	Proton
Thinning ratio	10^{-4} for $< 10^{20}$eV, 10^{-5} for $\geq 10^{20}$eV
Hadronic interaction model	QGSJET Ⅱ for energy $>$ 80GeV
	DPMJET Ⅲ for energy $<$ 80GeV
Cut threshold energy	100keV for all particles

Tab. 3: The simulation condition of COSMOS for this analysis.

These shower databases include the number of particles and energy for each particle type at each altitude. The number of particles with lateral distribution on the ground level is used for SD analysis and the longitudinal development of energy deposit along the shower axis is used for FD analysis. The example of longitudinal development is shown in Fig. 47.

Since several particles, mainly neutrinos, do not emit the fluorescence light, the total energy of these particles becomes missing energy for the FD analysis. It have to be estimated by using air shower MC simulation. In the procedure of this analysis, the energy of the primary cosmic ray is obtained by using the integrated value of the fitted Gaisser-Hillas function (Eq. 14). The details of this method are written in Section 7.4. The missing energy is defined as the difference between the true primary energy and integrated value of the energy deposit development. The estimated fraction of missing energy is shown in Fig. 48. The result shows that the typical missing energy for this analysis is about 8% with small energy dependence. The difference of the fraction of missing energy between COSMOS and CORSIKA[25] is $\sim$ 1%.

The missing energy depends on the primary particle. The comparison of the missing energy ratio between proton and iron is shown in Fig. 49. The difference is 5%. In this analysis, the missing energy of the proton is used for all of the observed events. So the systematic error of

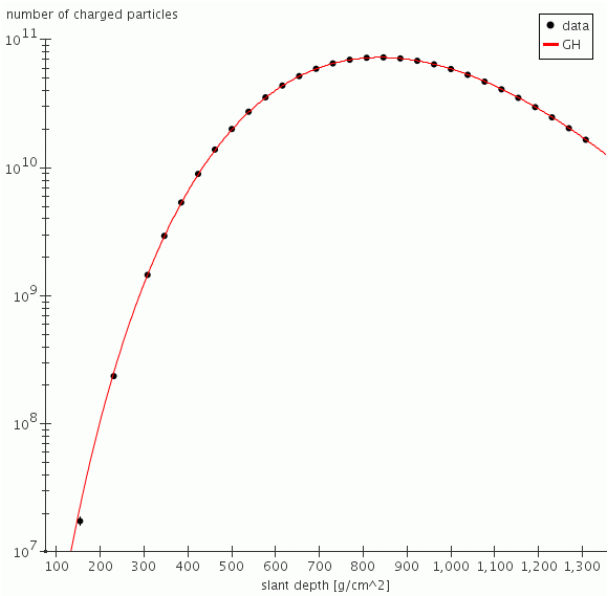

Fig. 47: Example of the longitudinal development created by COSMOS where primary energy is 10^{20}eV, cos(zenith angle) is 0.65. The horizontal axis shows the slant depth and the vertical axis shows the number of charged particles. Black points are the simulated data. The red line is the fitted Gaisser-Hillas function (Eq. 14). In this case, the X_{max} is 837.4g/cm^2 and the N_{max} is 7.137×10^{10}. This function matches the simulated longitudinal development.

the reconstructed energy for different primary particles is estimated to be about 5%.

6.2 Detector Monte Carlo for FD

The FD detector simulator written by JAVA is prepared for the air shower simulation with detector response. Currently, the air shower is generated by three methods: COSMOS database used in this analysis, CORSIKA, and Gaisser-Hillas function for a typical shower. In the COSMOS case, firstly, the longitudinal development of energy deposit at the 1g/cm^2 step is obtained by the interpolation of COSMOS database which has the information at 25g/cm^2 step. Each energy deposit is converted to the fluorescence photons with wavelength spectrum by the FLASH and Kakimoto models (Section 2.3.2). The atmospheric parameters are obtained by the result of the Radiosonde measurement (Section 4.5.1). Three types of Cherenkov light are also generated at that time: direct injected photons, scattered photons in the atmosphere by Rayleigh or Mie scattering. All of these photons are reduced by the solid angle, atmospheric transparency with wavelength dependence which includes the Rayleigh and Mie scattering. The typical value shown in Section 4.5 are used for the parameters for attenuation of the Mie scattering. The remaining photons are injected to the telescope simulator.

The telescope simulator has the segmented mirrors, optical filters and all of obstruction

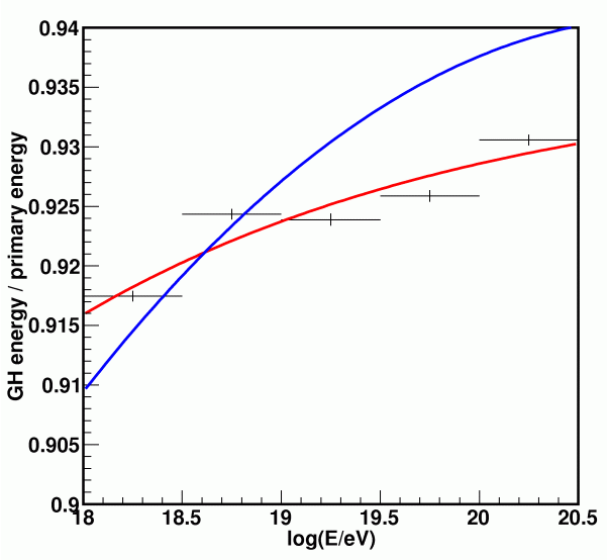

Fig. 48: Ratio of estimated energy obtained by the method of Gaisser-Hillas integration versus primary energy as the missing energy. The horizontal axis is the primary energy and the vertical axis is that ratio. Black points are the COSMOS data and the red line is fitted line as A-B$\times$($E_{primary}$/1EeV)$^{-C}$ where (A,B,C) is (0.9365, 0.02064, 0.2069). The blue line is the result of the same study by CORSIKA where primary particle is proton, energy cuts is 500KeV for electro-magnetic particles and thinning factor is 10^{-4}[48].

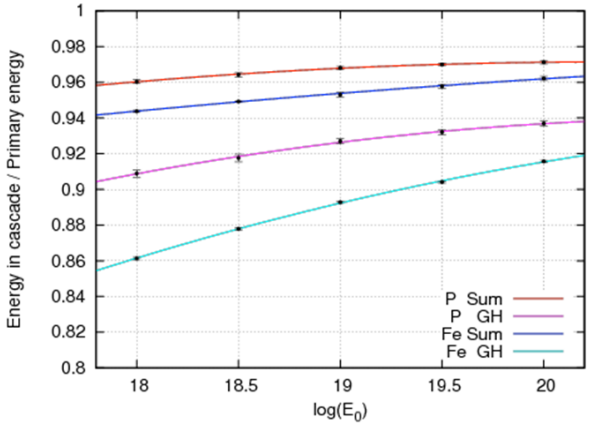

Fig. 49: The comparison of the missing energy ratio between the proton and iron. The horizontal axis is the energy and the vertical axis is the ratio of the reconstructed energy to simulation true value. The red line is the sum of all energy deposit for the proton primary. The purple line is the integration of the fitted Gaisser-Hillas function for the proton primary. The blue line is the sum of all energy deposit for the iron primary. The light blue line is the integration of the fitted Gaisser-Hillas function for the iron primary.

such as camera frames, camera boxes and shutter frames (Fig. 50).

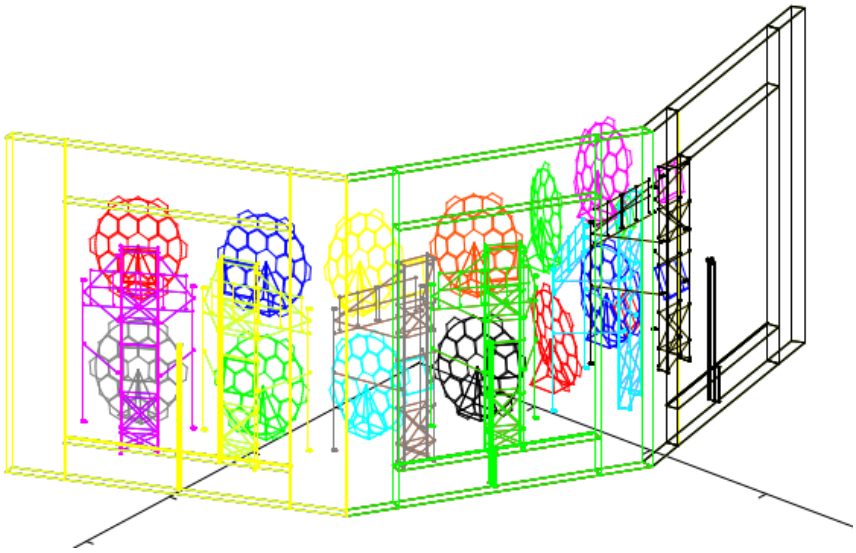

Fig. 50: Overview of the JAVA FD detector simulator.

All of injected photons are traced to the photo-tubes with these obstructions. The reflected angle at the mirror is fluctuated randomly by the Rayleigh distribution where σ = 0.19 degrees. It corresponds to the target for the tuning of the segment mirrors. The radius of spot size at the focal plane is less than 3.0cm. The simulated spot is shown in Fig. 51. This parameter is calculated roughly because the spot is not circle. The precise adjustment of all of the geometrical information to the real detector is done by star light calibration.

The geometry for the FD detector simulation is fixed by the star light calibration. It is based on the study for the HiRes detector[49] with the TD1 Catalog of stellar ultraviolet fluxes[50]. A star light can be observed clearly as the pedestal height by DC-coupled electronics. The air planes, lightning and the moon become the noise to pick-up the star light. However, since the positions of the stars are well-known and the pulse width of the light from the air plane and lightnings are much shorter than those from the star light, the star light is selected easily. By this method, the position, pointing direction and curvature of mirrors, the rotation of cameras, pointing direction of each photo-tube are adjusted to the obtained star image on the camera plane. The comparison of obtained pointing direction by star light calibration with that by ray tracing method for the corrected geometry is shown in Fig. 52. The geometry is adjusted at a level less than 0.1degree by the star calibration.

The background for the FD is important for calculating the aperture. It is affected by the night sky background with star light. The values of mean and dispersion of the background which are recorded by SDF (see Section 3.2) are stored in the database every 10 minutes. The time of 10 minutes corresponds to the time when a star goes through the field of view for the

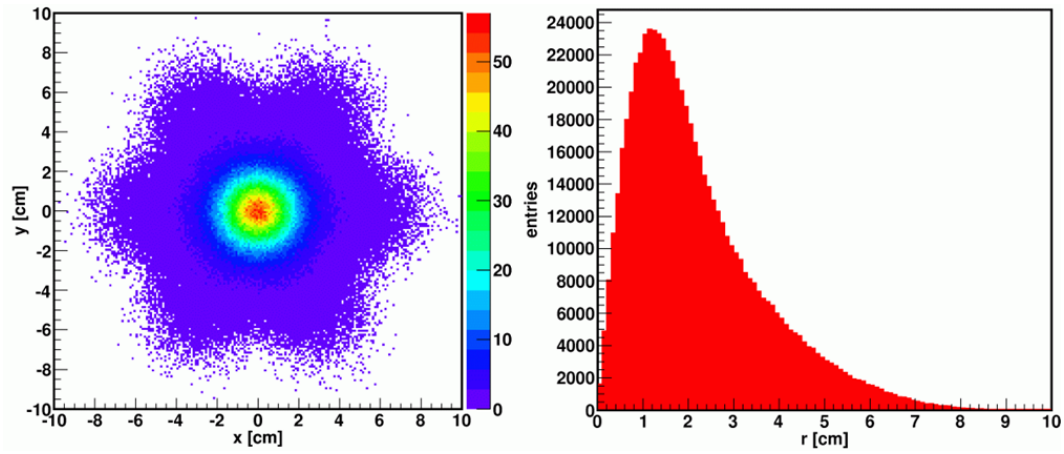

Fig. 51: The spot size of the FD detector simulation. To obtain these figure, the parallel photons are injected to the all of the mirror area. In the left figure, the horizontal and vertical axes are along the focal plane, and colors show the number of detected photons. The right figure shows the radius distribution. Since the FD mirror consists of the hexagonal segment mirrors, the spot is not a circle.

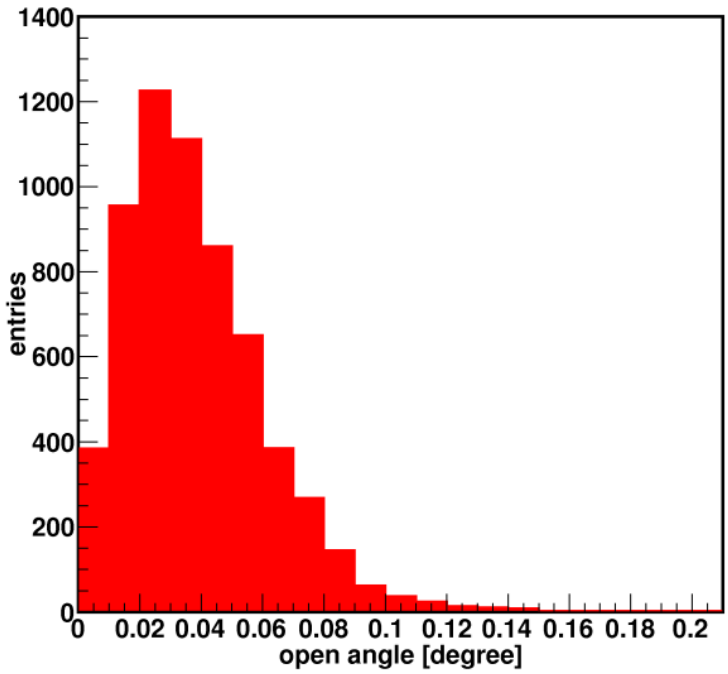

Fig. 52: The opening angle of the PMT pointing directions obtained by star light calibration and ray tracing for the corrected geometry. The vertical axis shows the number of entries and the horizontal axis shows the opening angle. All of PMTs in the BR and LR station (6144 PMTs) are plotted.

PMTs with spot size. The MC simulation uses the database to obtain the real background. The example of the data in the database is shown in Fig. 53.

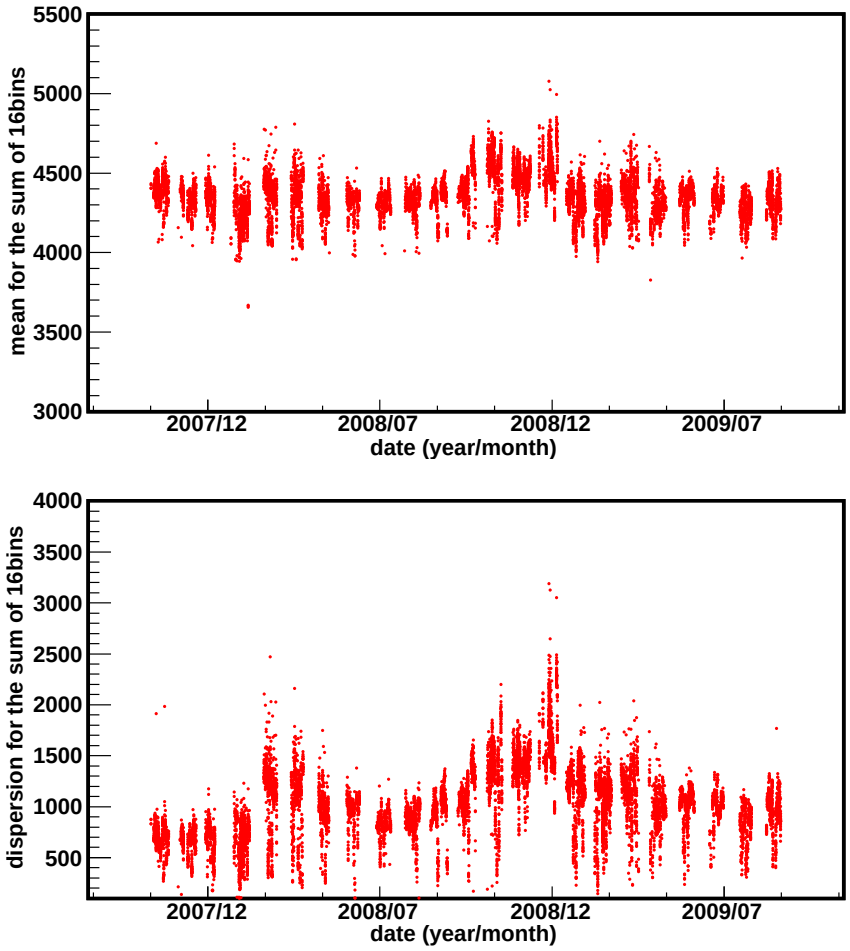

Fig. 53: The example of the database for the background. The upper figure shows the mean values for 2^{14} "bundles". The bundle consists of the sum of 16bins of FDAC count and is recorded by SDF continuously. This figure is for the 6th telescope in the BR station. The lower figure is the dispersion for the same PMT. The horizontal axis is the measured date (year/month).

6.3 Detector Monte Carlo for SD

The SD simulation is divided into two steps: generation for the particle lateral distribution on the ground and injection of detector response to the SD. An air shower generated by COSMOS includes the particle information on the ground, particle type and numbers. The SD detector simulation is prepared by GEANT4. It includes all of components: scintillators, a stainless-steel box, a roof, a battery, a solar panel and so on. The overview of this simulation is

shown in Fig. 54.

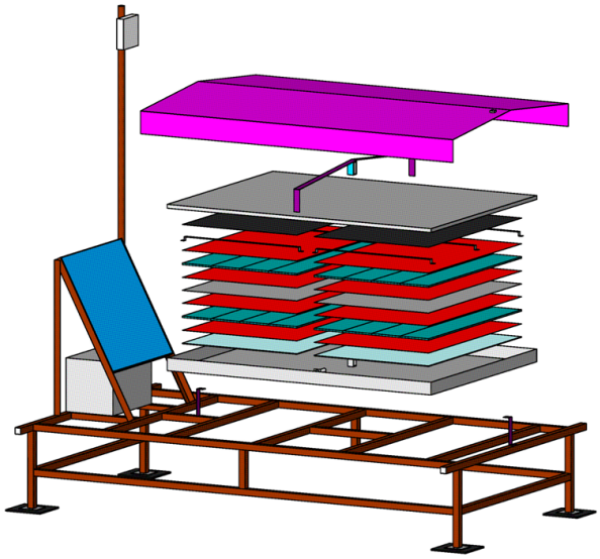

Fig. 54: The overview of the SD detector simulator by Geant4 simulation

The trigger is simulated by the same methods for DAQ with/without the boundary trigger. For the generation of the pseudo-data, this simulation uses the calibration constant with time dependence same as the real data analysis. It includes the photo-tube gain corrected by the temperature, response function of photo-tubes and electronics, time constant of the emission at the scintillator and transmission in the WLSF, position and height of each SD obtained by GPS, pedestal line and fluctuation and so on.

The analysis for the pedestal data monitored every 10 minutes is done by using this simulation. This analysis is done to obtain the conversion factor from waveform ADC counts to deposited energy. For the reproduction for the obtained pedestal, we generated the pseudo-background data with the spectrum of primary cosmic rays for each particle type by AMS data[28][29] (see Fig. 55). We trace particles to the ground by COSMOS with QGSJET2 and simulation with the detector response by this simulator. The example of this analysis is shown in Fig. 56. Since the obtained shape of charge distribution shows good consistency with the data, it means that the MC with COSMOS and data are consistent. The details of this analysis are shown in [30][31]. This technique generates the precise conversion factor from ADC counts to energy deposit. It is important for the SD analysis because this factor affects the energy scale directly.

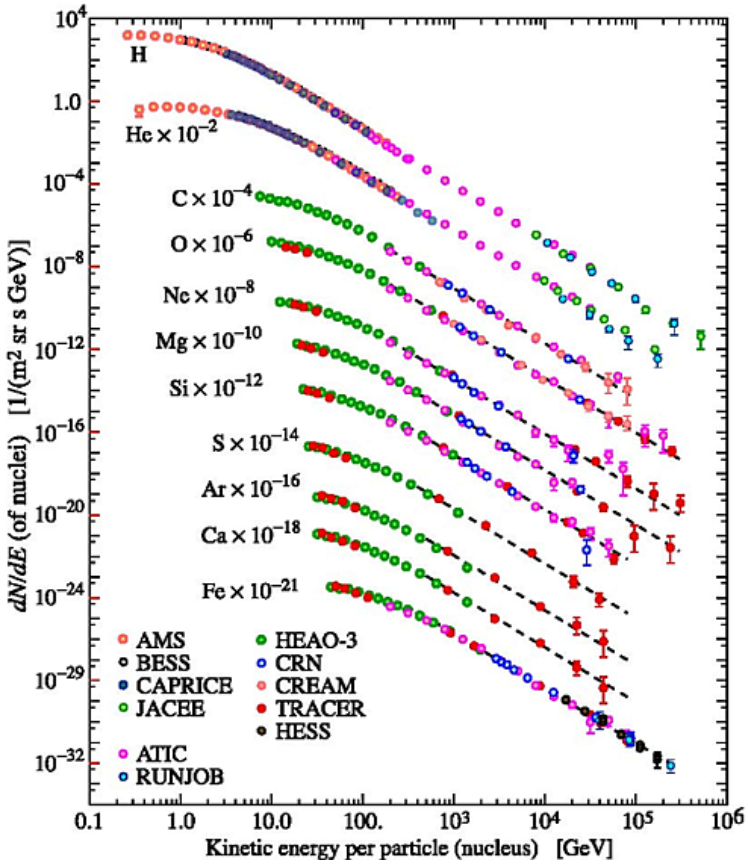

Fig. 55: The spectrum of primary particles obtained by AMS[28][29]. It is used for the SD background simulation.

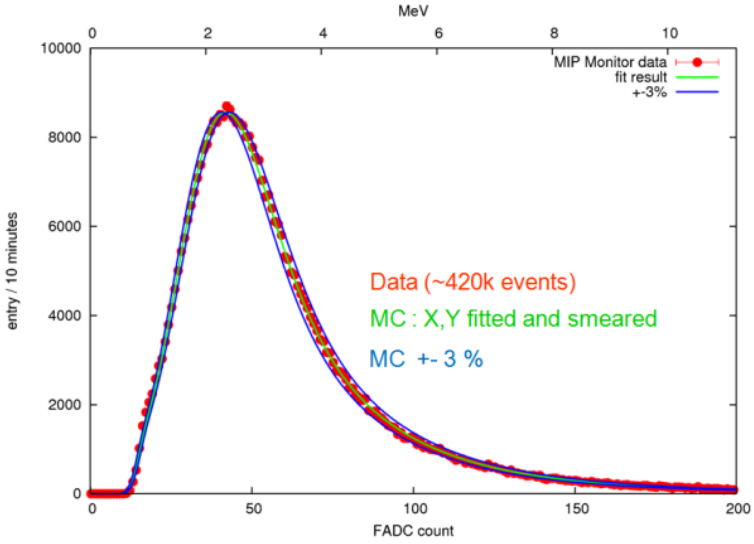

Fig. 56: The example of SD charge distribution. The red points show the data obtained every 10 minutes. The green line shows the simulated shape by SD simulator with calibration constant, for which the total number of events is normalized to that of data. The blue lines show the result when the normalization factor is changed by $\pm$ 3%.

7 Data processing for Hybrid analysis

In this section, the methods how to analyze the obtained hybrid data are discussed. The overview of the analysis is described in Section 5. The process of the analysis is divided into four steps:

- Conversion from the observed raw data to data base.
- Pre-reconstruction for selecting the signaled data.
- Geometrical reconstruction to obtain the shower axis
- Shower profile reconstruction to obtain the energy

The basic principle of the developed hybrid reconstruction is to improve the traditional FD analysis by requiring SD timing information. The schematic diagram of the traditional FD analysis is shown in Fig. 46. In the geometrical reconstruction, the timing information of the SD makes the traditional FD reconstruction precisely. The details are described in Section 7.3. The energy of the UHECR is reconstructed by the calorimetric technique of FD. The basic idea of the energy measurement by the FD is that the number of the emitted fluorescence photons along the shower axis is proportional to the deposited energy. The details are described in Section 7.4

7.1 Data Storage(DSTBank)

For easy treatment of data, most of raw-data is converted as DSTBank format which is used by the HiRes collaboration. This database consists of the simple custom byte strings and the libraries for reading / writing are prepared by C and JAVA languages. This step plays the two roles: selecting only the useful data and taking the corresponding calibration constant.

Since the FD raw data are too large ($\sim$ 1TB / month), only useful PMT data are picked up to DSTBank. Firstly, we select the neighboring camera to the triggered camera. Secondly, we pick up only high significant PMTs calculated by the same routine for signal search in SDF (Section 3.2.2). Currently, the threshold is set to 3 σ. By this handling, the data size is reduced to about 10%. The calibration data are also prepared by DSTBank by using the triggered time. The details of FD calibration analysis are described in Section 4.

The SD raw data are divided into 3 sub-arrays. So in the data storage step the SD raw data are combined to one DSTBank format with monitored data. The items of monitoring are described in Section 3.1.3

7.2 Pre-Reconstruction

In this section, we obtain the useful information for analysis from each FD PMT and reject noise hits. It is performed through four steps. The useful information for analysis, timing, S/N ratio, and the number of photo-electrons are obtained at the first selection. The 2nd and 3rd step work as the tighter selection to obtain the initial parameters for the 4th step by the track search on the camera plane and timing of each PMT. At the 4th step, the final PMTs are obtained by the geometrical reconstruction with the iteration. The 4th step judges for all the PMTs which includes the rejected PMTs in the 1st, 2nd and 3rd selections.

7.2.1 SD Pre-Reconstruction

Before the analysis for the FD, all triggered SD data are analyzed simply to obtain the deposited charge and timing. In this analysis, since the timing is used for calculating the shower core timing on the ground, the leading edge of the shower is important. So the first rising time is used as the timing of the SD.

The rising time is obtained by using the S/N ratio. The fluctuation of the pedestal line σ_{ped} is monitored every 10 minutes (see Section 3.1.3). Firstly, the waveform is divided into units which is defined from the bin above 3 $\times\sigma_{ped}$ to the bin below 3 $\times\sigma_{ped}$. The start time of the first unit is used for the timing of the SD as the leading edge. The total deposited charge is calculated by the integration of all waveform unit with the conversion factor from waveform count to energy deposit. This conversion factor is calculated by using monitored charge distribution and SD MC (Section 6.3). The global position of each SD is also obtained from the GPS information.

7.2.2 1st Selection

Firstly, we get the timing, signal size (the number of photo-electrons) and signal to noise ratio from each waveform by calculating the significance with the weight of the triangle shape, which is called triangle filter (Fig. 57). It looks for the largest significance $\sigma(w,i)$ with peak p and width w in the waveform:

$$\sigma_{w,p} = \frac{\sum_{i=p-w}^{p+w} F_{sub}(i)W(i)}{\sum_{i=p-w}^{p+w} P_{rms}(i)W(i)}, \tag{48}$$

$$W(i) = w - |p-i|, \tag{49}$$

where F_{sub} is the i-th bin of waveform subtracted by pedestal mean, W(i) is the weight, P_{rms} is the pedestal fluctuation. The mean and fluctuation of each pedestal were obtained by SDF (Section 3.2.2). This filter searches for the width w from 0 to 30th bin and the peak bin p in all of the bins.

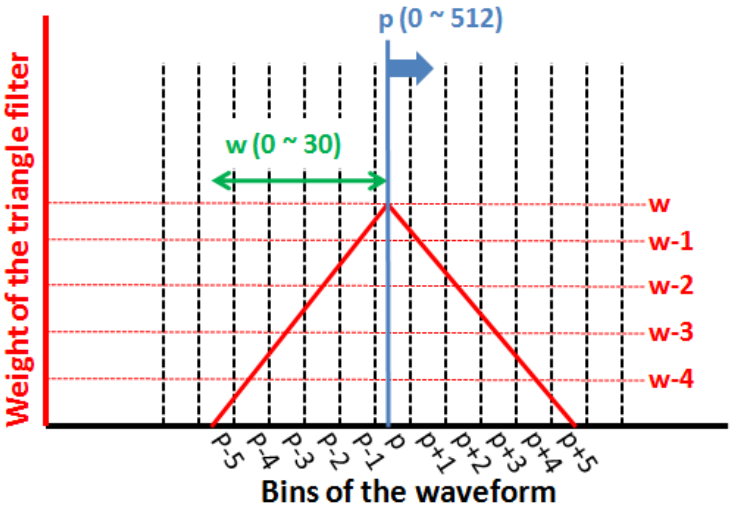

Fig. 57: The schematic diagram of the weight of the triangle filter. The triangle filter looks for the pair of peak p and width (w) with the maximum significance with the weight of triangle shape. The blue line shows the peak p and the green line shows the width w. The search range is from 0 to 512 bins for p and from 0 to 30 for w. The weight $W(i)$ for i-th bin ($p-w \leq i \leq p+w$) is calculated by $w-|p-i|$.

If it finds the pair of p and w with maximum significance, the timing T and its error σ_T are calculated by

$$T = 100ns \times \frac{\sum_{i=p-w}^{p+w} i \times F_{sub}(i)}{\sum_{i=p-w}^{p+w} F_{sub}(i)} \quad (50)$$

$$\sigma_T^2 = 100ns \times \frac{\sum_{i=p-w}^{p+w} F_{sub}(i) \times (T-i)^2}{\sum_{i=p-w}^{p+w} F_{sub}(i)}. \quad (51)$$

Here 100ns is the bin width corresponding to the 10MHz sampling. The timing T corresponds to the center of gravity in the assigned width. If the selected width is 30 bins, this PMT is treated as failed fitting for noise PMT and is not used for the analysis. The number of photo-electrons $N_{p.e.}$ is calculated by

$$N_{p.e.} = Gain \times \sum_{i=p-3\times w}^{p+3\times w} F_{sub}(i), \quad (52)$$

where Gain is the conversion factor from FADC count to the number of photo electrons which

is obtained by calibration (Section 4). The integration area between $p \pm 3w$ is much larger than the width of the detected pulse. $N_{p.e.}$ is used for the weight of geometrical and longitudinal fitting.

Secondly, we calculate each S/N ratio and select the PMTs with high significance (greater than 6σ) as the initial parameters for the next step. The S/N ratio is calculated by the same method used by DAQ (Section 3.2.2). The PMTs with small significance (lower than 6σ) are not used for the 2nd and 3rd steps. However we try to pick up some of them at the 4th selection.

7.2.3 2nd Selection

This step is the track scan on the camera plane to reduce of the PMTs with noise hit by using the coordinate conversion, which is called Hough Transform. This is one of the features of the extraction method in image analysis. In general, a line in X-Y plane is represented by a parameter pair (ρ,ω) as

$$\rho = x\cos\omega + y\sin\omega. \tag{53}$$

The ρ-ω space is called Hough space and this parameterisation is called Hough Transform. A line group which goes through the same point (x_i,y_i) is shown as the curve line in the Hough space. Therefore, the cross point of all curved lines which corresponds to all positions of PMTs is shown as the track line on the PMT direction plane (Fig. 58).

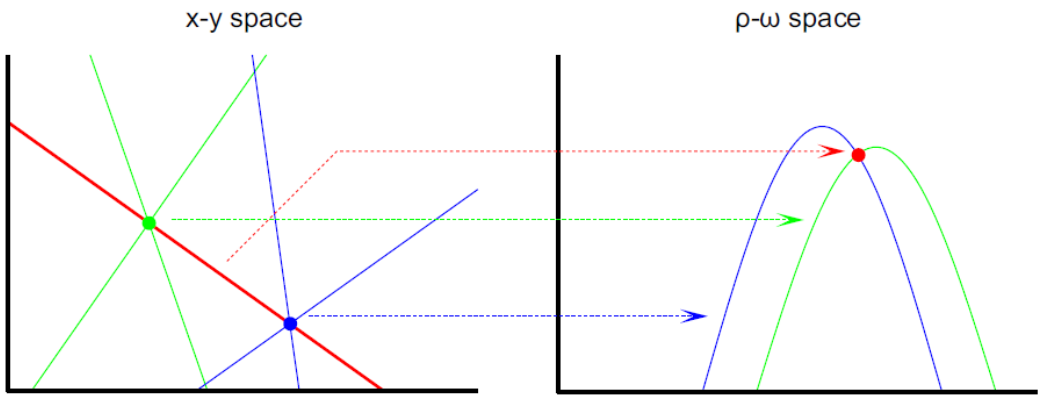

Fig. 58: Schematic view for the Hough Transform. Since the line group which goes through a point in the x-y space is represented by one curved line in the ρ-ω space, the line which goes through the several points is shown as the cross point in the ρ-ω space.

In the analysis, we create points (θ,ϕ) in the azimuth angle and zenith angle plane which correspond to each PMT direction and search for track line by Hough Transform. The relevant parameters (ρ,ω) are obtained by using the center of gravity near the peak in the cross point distribution. The example of this result is shown in Fig. 59

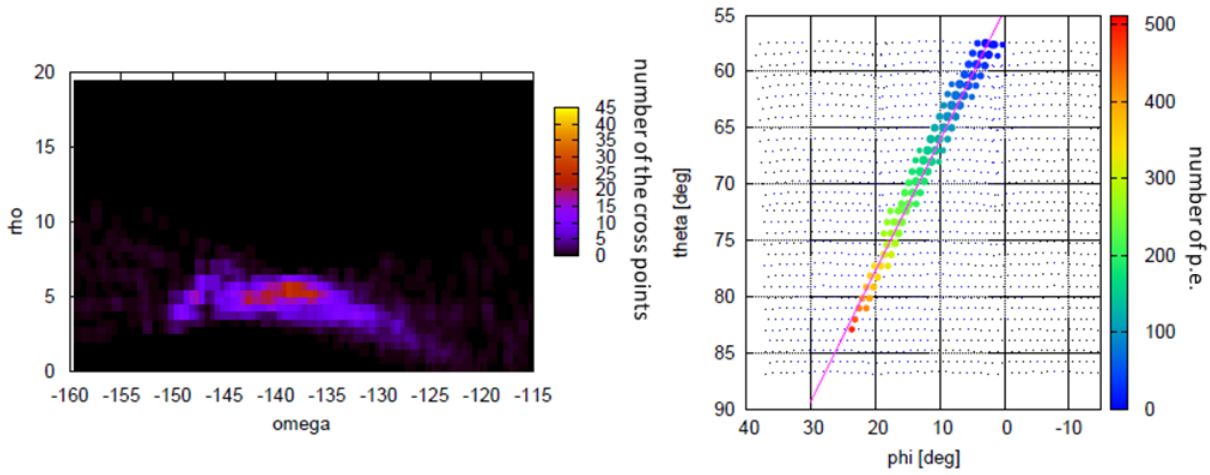

Fig. 59: The left figure shows the cross point distribution of the Hough Transform. The right figure shows the obtained track line (red line) and PMT direction with timing(color) and the number of photo-electrons is proportional to the size of the circles.

After the decision of the track line, we reject the separated PMTs from the track. The elongation angle β_i of the PMT$_i$ is defined as

$$\cos(\beta) = \vec{n}_i \cdot \vec{n}_{proj,i}, \tag{54}$$

where $\vec{n}_i$ is the direction vector of i-th PMT and $\vec{n}_{proj,i}$ is the projection vector to the obtained line (ρ,ω).

For the decision to reject PMTs, all of the β_i of the PMTs are filled to the histogram with 1 degree bin width. The threshold is obtained by the first zero entried bin which is scanned from the bin of 0 degree. The PMTs which have β above the threshold are rejected before the next step.

7.2.4 3rd Selection

The separated PMTs with noise hit in the camera plane are rejected by the 2nd selection. However other PMTs with noise close to the track remain. In the 3rd and 4th selections, we reject them by using timing information. The expected arrival time t$_i$ is represented as

$$t_i = t^* + \frac{1}{c}\frac{\sin\psi - \sin\alpha_i}{\sin(\psi+\alpha_i)} r_0, \tag{55}$$

where t* is the timing when the shower core hits the ground, r$_0$ is the distance of the shower core on the ground from the FD station, α is the elevation angle of the direction of i-th PMT on the SDP and ψ is the elevation angle from the shower core. These parameters are explained in Fig. 46. For the precise fitting, in this step, we try to fit simply and do the rough PMT selection.

The line which is calculated by Hough Transform in the 2nd step is used as the shower detection plane.

For the decision by which PMTs are rejected, the residual ΔT, the time difference between the time of the PMT and expected time by the fitted function, is calculated for all of the PMTs and filled to the histogram with 1 μs bin width. Each bin is scanned from 0 μs and the first bin with no entry is decided as the threshold for the rejection. The PMTs which have the ΔT above the threshold are rejected before the next step.

7.2.5 4th Selection

In this step, we select PMTs by timing information almost same as hybrid geometrical reconstruction. By the 1st, 2nd and 3rd selections, only PMTs with high significance are selected for initial parameters of this step. This step works not only for the rejection but also for the addition of the rejected PMTs in the previous selections.

Firstly, the elevation angles of the PMT directions on the obtained Shower Detection Plane (SDP) described in Fig. 46 and timing of all selected PMTs are fitted by hybrid mono timing fitting. The details for this timing fit and how to obtain the SDP are described in Section 7.3.

Secondly, the timing difference R_i from fitted function, pseudo χ_i^2 and opening angle with SDP β_i are calculated for all PMTs, including all rejected PMTs in the previous steps:

$$R_i = |f(\alpha_i) - T_i|, \tag{56}$$

$$\chi_i^2 = (\frac{R_i}{\sigma_{T_i}})^2, \tag{57}$$

$$\beta_i = \vec{P_i} \cdot \vec{V}_{NSDP}, \tag{58}$$

where α_i is the projected elevation angle to the SDP of i-th PMT, $f(\alpha_i)$ is the obtained timing from the fitted function at α_i, σ_{T_i} is the error of the peak timing obtained by the 1st selection, $\vec{P_i}$ is the pointing vector, $\vec{V}_{NSDP}$ is the perpendicular direction to the SDP. These parameters are used for the judgement for addition/rejection of PMTs. These PMTs are categorized by the criteria, which is shown in Table. 4. There are two types of criteria: SOFT and HARD. Firstly these PMTs are categorized by SOFT criteria. After the 4th step with SOFT criteria is finished, this step is applied again with HARD criteria for the precise selection.

ITEMS	SOFT	HARD
R_i	$< 1.2\mu$ s	$< 0.8\mu$ s
χ_i^2	< 20	< 15
β_i	$< 4^\circ$	$< 2^\circ$

Tab. 4: The criteria for selecting the candidate PMTs in the 4th PMT selection.

Each categorized PMT is judged by the linear fitting of α_i and T_i with the neighboring

PMTs, which are selected by the opening angle with the judged PMT $< 5^\circ$ and timing difference $< 5\mu s$. The time difference from fitted function R_{Lin}, pseudo χ^2_{Lin} and the number of used PMTs N_{Lin} are used for this judgement. The criteria are shown in Table. 5. This judgement works for the rejection for the PMTs which have isolated position and timing. If the PMT which is in these criteria, this PMT is picked up and the 4th selection starts again. If the PMT which is not in these two criteria, this PMT is rejected and the 4th selection is also restarted. This iteration continues until there is no corresponding PMT.

ITEMS	THRESHOLD
N_{Lin}	> 3
R_{Lin}	1.2μ s
χ^2_{Lin}	20

Tab. 5: The criteria for the judgement by the linear fitting in the 4th PMT selection.

The examples of the selected PMTs are shown in Fig. 60. The event-like PMTs are picked up by these selections.

7.3 Geometrical Reconstruction

Since the target threshold energy of UHECRs in this analysis is around $10^{18.7}$eV, the SD event is almost poor and mainly only three or four SDs can be used for the analysis. So it is difficult to estimate the core position only by SDs. In this analysis, the hybrid geometrical reconstruction method which uses only one SD is developed. This method is useful for the lower energy event.

In the near future, the hybrid-trigger, by which SD is triggered using FD information, will be installed. These events have lower energy, less than $10^{18.0}$eV, and one or two SDs can be used for the analysis. This technique will be used for the events with lower energy. So the hybrid trigger makes the better reconstruction of the hybrid events even with one SD information.

In the geometrical reconstruction by the monocular FD analysis, the geometry is decided by using PMT direction and timing:

$$T_{exp,i} = T_{core} + \frac{1}{c}\frac{\sin\psi - \sin\alpha_i}{\sin(\psi+\alpha_i)}R_{core}, \tag{59}$$

where $T_{exp,i}$ and α_i are the expected timing and the elevation angle on the SDP for the PMT$_i$, T_{core} is the timing when the air shower reached on the ground, R_{core} is the distance from the FD station to the core position, ψ is the elevation angle of the air shower on the SDP. The axis is decided by the three parameters, ψ, R_{core} and T_{core}. The definition of these parameters is shown in Fig. 61.

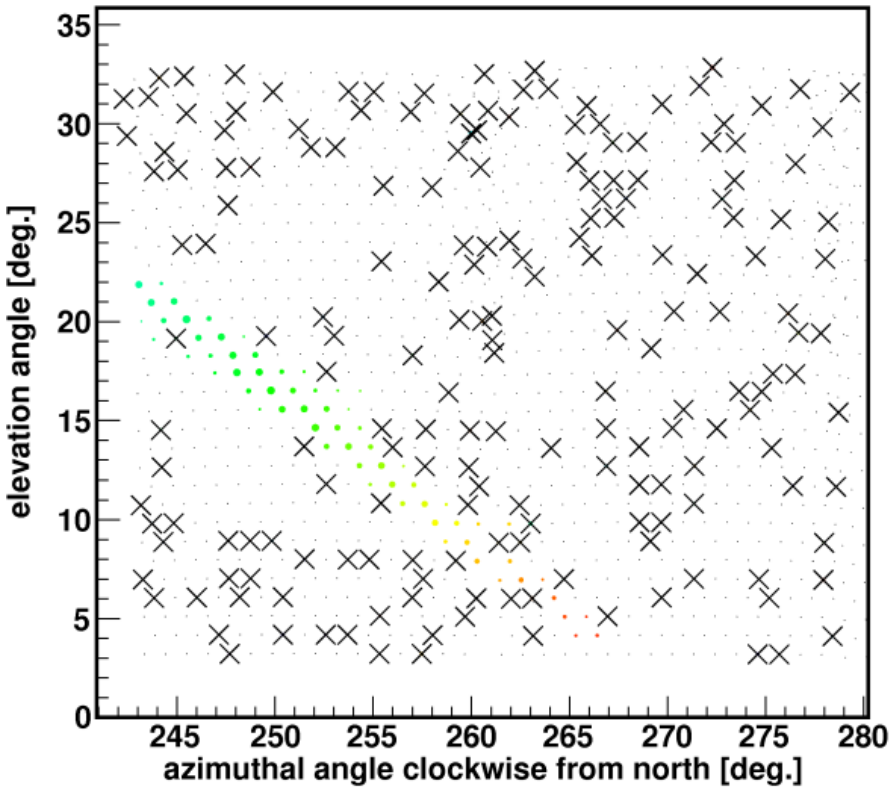

Fig. 60: The example of the PMT selection. This is a real event observed on June 02, 2008 in the BR station. The horizontal and vertical axes show the pointing direction of each PMT. Filled circles show the PMTs with S/N $> 3\sigma$. The size is proportional to the square root of the obtained number of photo-electrons. The color shows the timing, ("blue" is fast and "red" is late). The cross marks are the rejected PMTs.

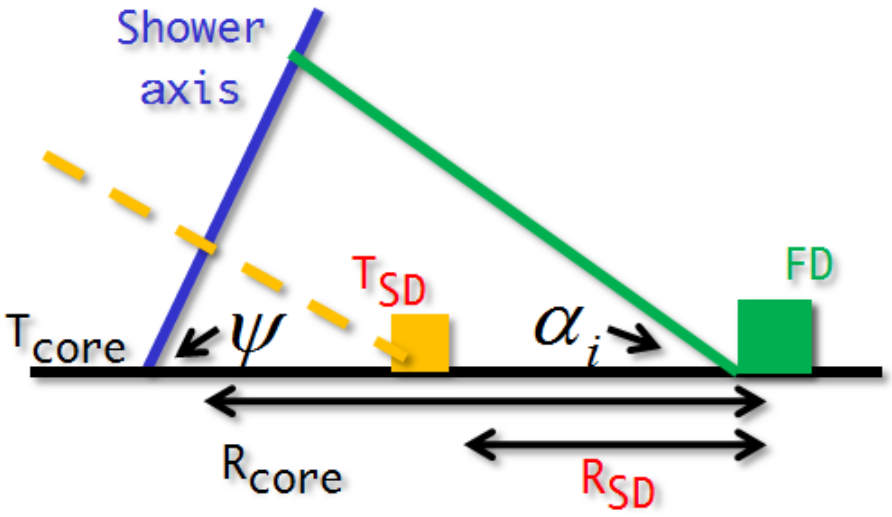

Fig. 61: The pattern diagram for the geometrical reconstruction.

This method decides the SDP precisely. However, the estimation for the shower depth using FD is difficult. The distance between a shower and FD station affects the estimated energy directly. If this event has an SD with signal near the core, T_{core} can be calculated by:

$$T_{core} = T'_{SD} + \frac{1}{c}(R_{core} - R_{SD})\cos\psi, \tag{60}$$

$$T'_{SD} = T_{SD} - \frac{1}{c}\{(\vec{P'}_{SD} - \vec{P}_{SD}) \cdot \vec{P}\}, \tag{61}$$

where $\vec{P}_{SD}$ is the position of the SD, $\vec{P'}_{SD}$ is the projected SD position on the SDP, $\vec{P}$ is the direction of the shower axis from the ground, T_{SD} is the timing of the reading edge of the SD which is described in Section 7.2.1, T'_{SD} is the corrected timing for the projection length and R_{SD} is the distance between FD and $\vec{P'}_{SD}$. So the χ^2 can be written as:

$$\chi^2 = \sum_i \frac{(T_{exp,i} - T_i)^2}{\sigma^2_{T,i}}, \tag{62}$$

where σ_T is the fluctuation of the estimated timing which is calculated at the 1st selection. This function has the assumption that the shower front structure is flat. This assumption is good enough when the SD is near the shower axis or the energy of the primary particle is small. The typical structure of the shower front is the 100ns delay at 600m far from shower core and 10^{19}eV energy. On the other hand, as the energy becomes lower, the particles in the shower front is dominated by the muon. In that case, the fluctuation becomes large, but the typical delay from the flat assumption is small.

When the hit SDs include the noise-triggered detectors, these SDs have to be rejected. The hybrid analysis can also select the signaled SDs better than the other analysis which is done

only by FD or SD only. In this analysis, firstly, the detectors which are triggered clearly by noise are rejected by the information of FD. The SDs which are far from 1.2km from the line where SDP and ground cross are rejected. After this rejection, this method tries to use the other SDs and select the result which has least χ^2 (Eq. 62). This method is also used for the 4th selection, and the noise reduction for both detectors and decision of the SDP and shower axis become better by the hybrid technique. The resolution for this method is discussed in Section 8.

7.4 Longitudinal Reconstruction

The produced photons by the air shower is caused not only by fluorescence light but also Cherenkov light (Section 2.3). The origin of the detected photons are divided into four types: Fluorescence light, direct Cherenkov light, scattered Cherenkov light by Rayleigh and Mie phenomena. It is difficult to divide detected photons to each origin because Cherenkov light depends on the energy, age, atmosphere and so on. We use the MC simulation for the reconstruction of the longitudinal development, called Inverse MC (IMC) technique.

The idea of this technique is simple, looking for the best air shower by the comparison between data and MC. This technique includes the irreversible component at the telescopes, non-uniformity of the photo-cathode, spot size at the camera plane and so on. The critical problem of this technique is that it takes long time to produce the air shower of the UHECR and to trace the photons to the telescopes. We have the database which includes the air showers produced by COSMOS. However, the variation of the generated air showers is not enough for using the full IMC. So the important things for this technique are the simplification with keeping the accuracy as mentioned below.

In this analysis, the air shower for this reconstruction is generated by Gaisser-Hillas function(Eq. 14). It is good assumption to represent the simulated shower by COSMOS and CORSIKA. For the reduction of the calculation time, the database is used instead of the ray tracing. This database consists of the detection efficiency for each PMT with the arrival direction. For the generations of this database, the parallel 100k photons are injected to each telescope by 0.125 degree step. This simulation includes all the obstructions, the space with each segment mirrors, non-uniformity of the photo-cathode and spot size on the camera surface. On the other hand, all of the calibration constants are not included because almost all the parameter have time dependence. The example of the prepared data in the database is shown in Fig. 62.

For IMC technique, firstly, the shape of the photons along the shower axis is decided with the Gaisser-Hillas function where X_{max} is a variable and N_{max} is fixed to 1. For each air shower, the expected number of photo electrons $N'_{p.e.,i}$ detected by each PMT_i is calculated by

$$N'_{p.e.,i} = \sum_{type} \int_x E(x,type) D(x,type) \frac{A(x)}{4\pi r(x)^2} \varepsilon(x,type) dx, \quad (63)$$

$$\varepsilon(x,type) = S(x) \int_{lambda} f(\lambda,type) T(x,\lambda) R(\lambda) d\lambda, \quad (64)$$

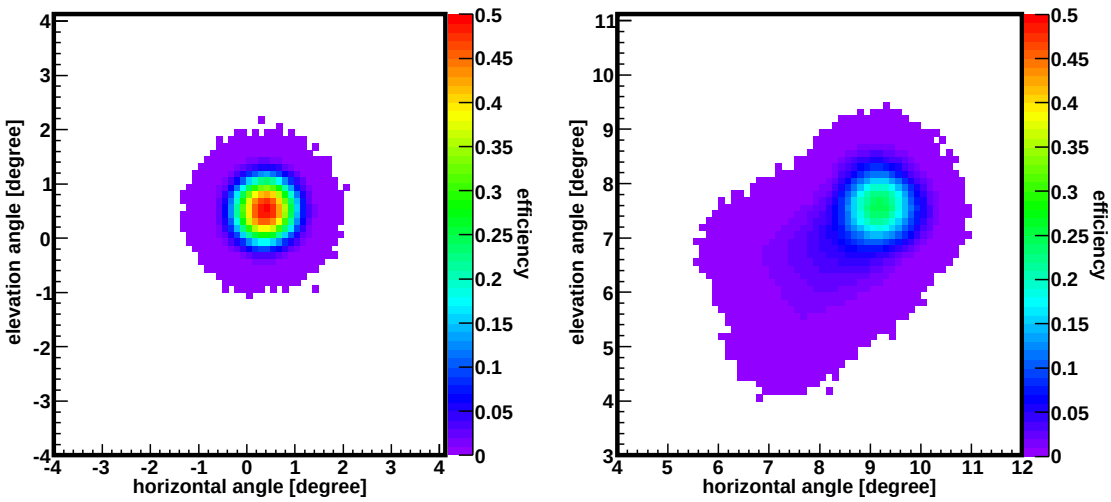

Fig. 62: The examples of the data in the database for IMC. The left figure shows the data of the PMT77 (at the center of the camera) and the right figure shows the data of the PMT00 (at the edge of the camera). Each PMT corresponds to the 6th telescope in the BR station. The horizontal and vertical axes are the arrival direction relative to the center of the field of view of each telescope. The colors are the ratio of the detected photons and injected photons.

where "type" is the origin of the photon production (fluorescence, direct Cherenkov, scattered Cherenkov by Rayleigh and Mie), x is the slant depth along the shower axis, E(x,type) is the total number of photons, D(x,type) is the fraction of the angular distribution from the corresponding point of x to FD station for each type, A(x) is the aperture of mirror area same as the simulation for creating the database, r(x) is the distance to the FD station, $\varepsilon(x, type)$ is the detection efficiency with the atmosphere and detector, S(x) is the detection sensitivity in the database, λ is the wavelength, f(λ,type) is the wavelength fraction for each phenomena, T(x,λ) is the atmospheric transparency and R(λ) is the detector efficiency. The atmospheric transparency and detector efficiency are calculated as:

$$T(x,\lambda) = T_{Rayleigh}(x,\lambda)T_{Mie}(x,\lambda) \quad (65)$$

$$R(\lambda) = R_{mirror}(\lambda)\tau_{filters}(\lambda)P(\lambda), \quad (66)$$

where $T_{Rayleigh}(x,\lambda)$ and T_{Mie} are the parameters of transparency for Rayleigh and Mie scattering respectively, $R_{mirror}(\lambda)$ is the mirror reflectance, $\tau_{filters}$ is the transmittance of the BG3 and paraglas, P(λ) includes the efficiency of the PMT (quantum efficiency, correction efficiency and gain). Each value is used by the calibration constant (Section 4).

The expected number of photo electrons for each X_{max} is calculated by using the above-

mentioned method. The X_{max} is calculated by maximizing the Likelihood L:

$$L = \sum_i N_{p.e.,i} \log(\frac{N'_{p.e.,i}}{\sum_i N'_{p.e.,i}}), \tag{67}$$

where $N_{i,p.e.}$ is the sum of the photo electrons at each PMT which is calculated in the 1st selection, $N'^{station}_{p.e.}$ is the total number of photo electrons in the FD station. After the decision of the X_{max}, the N_{max} is calculated by the scaling as follows:

$$N_{max} = \frac{\sum_i N_{p.e.,i}}{\sum_i N'_{p.e.,i}}. \tag{68}$$

The primary energy is calculated by the integration of the Gaisser-Hillas function (Eq. 16) with the correction for the missing energy (Fig. 48). The resolution of the reconstructed N_{max}, X_{max} and energy by this method is discussed at the Section 8.

7.5 Quality cut

To ensure the quality of the reconstructed values such as the direction of the shower axis, X_{max} and energy, this analysis requires the data cut for the reconstruction. The result for the geometry and longitudinal fitting has to be converged. The χ^2 for the geometrical fitting also has to be less than 100. The most powerful cut condition is that the X_{max} has to be observed within the field of view of FD. The positions of shower maximum of the events with high energy around $10^{19.5}$eV can be the under the ground. We cannot reconstruct the energy precisely for these events. To measure the spectrum, the lower limit of the energy is set as $10^{18.65}$ eV and the zenith angle is required to be more than 45 degrees. To reduce the effect of the uncertainty of the aperture, the lower threshold of energies is decided at which the trigger efficiency of the SD is above 80%. The aperture is discussed in Section 8.3. The threshold of the zenith angle is limited by the air shower database which is prepared below 50 degrees. The prepared database of the air shower was described in Section 6.1. The efficiency of the reconstruction with cuts is discussed in Section 8.

8 Monte Carlo studies

8.1 Dataset

The hybrid data set is prepared by the detector MC with the COSMOS database (Section 6.1). The date for the simulation data is obtained randomly within only FD observation period from May 27, 2008 to June 30, 2009. Two types of data set are prepared: flat type and slope type. About 20k events are prepared for each energy in the COSMOS database (0.1 step of the logarithm). The data set of the other type is 2.5M events with the slope of $E^{-3.1}$ from $10^{18.0}$ eV. The injection area is 25km radius from the center of the site (CLF) with the cosine zenith angle from 0.65 to 1. So the injection aperture is

$$A_{injection} = \iint S * \cos\theta \sin\theta d\theta d\phi \quad (69)$$
$$= 0.5775\pi S, \quad (70)$$

where S is the injection area. All of the calibration constants with the time dependence are also applied to MC simulation in the same way as real data (Section 6.2,Section 6.3).

8.2 Resolutions

The resolution of the reconstructed geometry and shower profile for the hybrid technique is obtained by using the slope-type data. These data pass the reconstruction process with quality cuts mentioned in Section 7.5. Since the lower energy threshold of the quality cut is set as $10^{18.7}$eV to measure the spectrum, the resolutions shown here correspond to those around $10^{18.7}$eV. Each resolution is obtained by comparison of the simulation true value with reconstructed value. The opening angle of the normal vector of the SDP is shown in Fig. 63. The resolution of the opening angle is about 0.4 degrees. The resolution for the core position is about 200m (Fig. 64). The arrival direction of the UHECR is determined with the accuracy of about 1.1 degrees (Fig. 65). The resolution of the Rp, which is the distance of the shower axis from the FD station, is about 1% with 1% systematics shift (Fig. 66). These resolutions are better than the values from FD monocular reconstruction. For example, in this energy region, the resolution of the arrival direction by FD monocular analysis is several degrees and the resolution of the core position is more than 600m.

To obtain the energy spectrum, the leakage from larger zenith angle should be considered. The cosine zenith angle of the generated MC data ranges from 0.65 (49.5 degrees) to 1. On the other hand, in this analysis, the value of 45 degrees is used as the threshold of the zenith angle. So the limit of the zenith angle to obtain the energy spectrum is decided by the considering resolution at the largest zenith angle in the MC data. Fig. 67 shows the zenith angle resolution at the true cosine zenith angle of 0.65. Since there is enough separation from 45 degree, this

MC simulation data can be considered for the leakage from lower angle with the limit at the zenith angle of 45 degrees.

The N_{max} resolution is shown in Fig. 68. It has -9% systematic shift and $\sim$ 8% resolution. The X_{max} resolution is $\sim$ 30 g/cm^2 with -13 g/cm^3 systematic shift (Fig. 69). These results are affected by the uncertainty of Rp. The energy resolution is shown in Fig. 70. The peak value is shifted by -8% and the resolution is 8%. These resolution values are also better than SD and FD monocular reconstruction. For example, in the SD analysis, the energy resolution for the energy range concerned is more than 10%. FD monocular analysis has also more than 15% resolution. The resolution of this analysis shows the best resolution in the TA experiment.

By using the slope-type and flat-type data, we obtain the energy dependence of systematic shift of reconstructed energy and the energy resolution as shown in Fig. 71. The systematic shift of reconstructed energy is about 8% with small energy dependence.

The systematic shift is caused by the difference of the air showers which are generated by the COSMOS and Gaisser-Hillas function. For generating the MC data, the air shower generated by the COSMOS is used. On the other hand, in the IMC reconstruction method, the air shower is generated by the Gaisser-Hillas function because the full MC of the air shower needs the huge calculation time. However, since the Gaisser-Hillas function represent the number of the charged particle along the shower axis, the conversion factor from the number of charged particles to the energy deposit has to be used with some assumptions. Since the amount of the energy deposit in the ionization loss depends on the energy in the low energy, this conversion factor depends on the energy distribution of the charged particles in the air shower. In the IMC method, the constant value, 2.2MeV/g/cm^2, is used as the conversion factor. On the other hand, the deposited energy in the COSMOS is more accuracy because the COSMOS calculates the deposition by the sum of each particles with each energy. The correction of the systematic shift means the correction of the dE/dX in the IMC process. So this shift is used as the correction for the shift of reconstructed energy to measure the energy spectrum.

The energy resolution is 7 $\sim$ 8%. The result at 10^{20}eV in Fig. 71 shows strange behavior. Since it is caused by the COSMOS shower with QGSJET II, the correction around 10^{20}eV should be done by using the interpolation of data points near 10^{20}eV.

The leakage from the lower energy is also important to obtain the energy spectrum. The energy of the MC data is above $10^{18.0}$ eV. The lower limit to obtain the energy spectrum is decided by the energy resolution at $10^{18.7}$ eV. Since the energy resolution is about 8%, the leakage of the energy spectrum is considered by the prepared MC data.

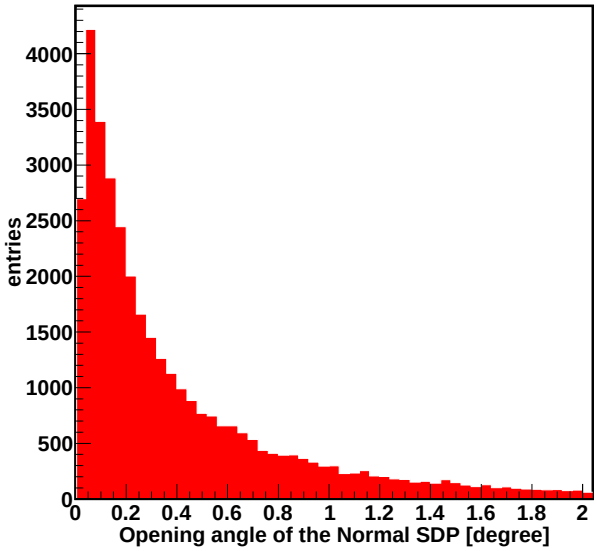

Fig. 63: The opening angle of the normal vector of SDP between simulation true and reconstructed value as the resolution of the SDP. The unit of the horizontal axis is degree. The peak is $\sim$ 0.1 degree and σ(68%) is $\sim$ 0.4 degree.

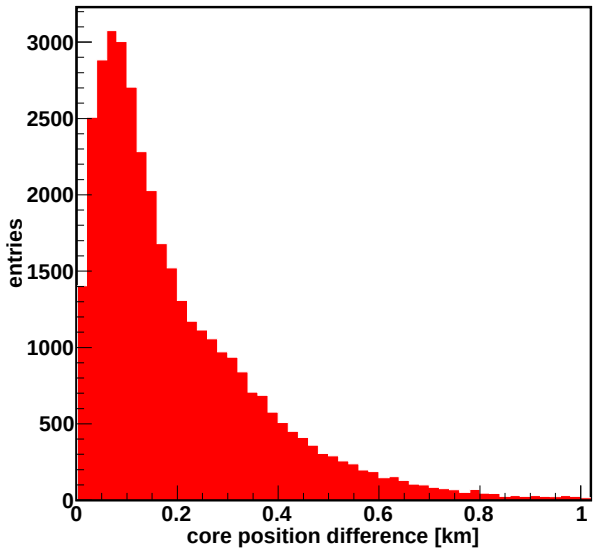

Fig. 64: The core position difference. The horizontal axis is the difference of the core positions between simulation true value and reconstructed value. The vertical axis is the number of events. Peak value is $\sim$ 100m and σ(68%) is $\sim$ 200m.

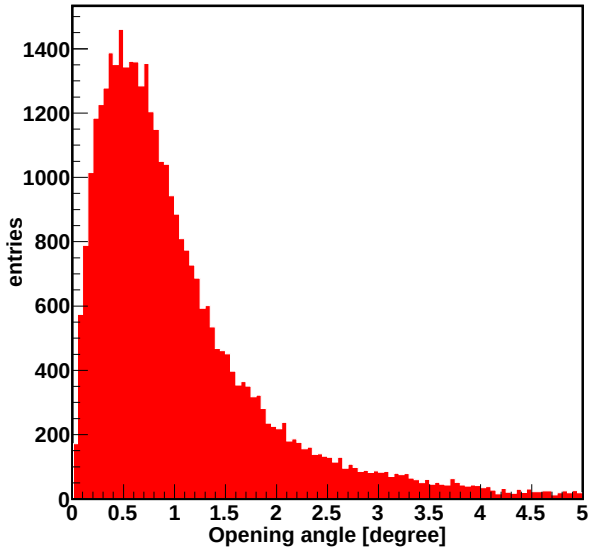

Fig. 65: The arrival direction difference. The horizontal axis is the opening angle between simulation true and reconstructed value. The vertical axis is the number of events. The peak value is $\sim$ 0.7 degrees and σ(68%) is $\sim$ 1.1 degrees.

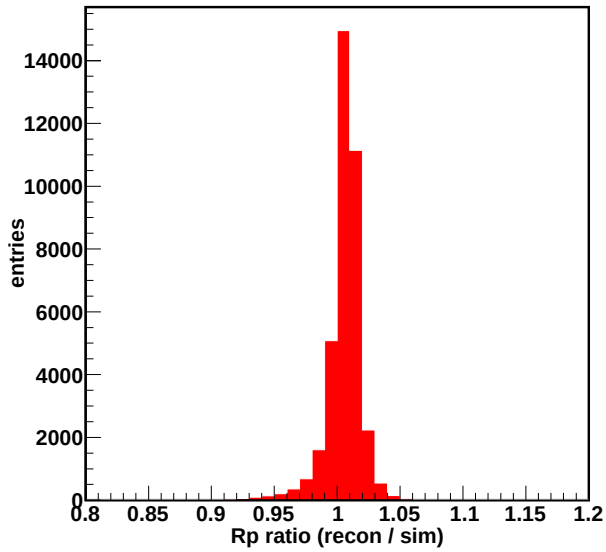

Fig. 66: The resolution of the distance of the shower axis from the FD station. The horizontal axis is the ratio of the reconstructed Rp value to the true Rp value. The vertical axis is the number of entries. The standard deviation is $\sim$1% and the peak value is shifted by +1%.

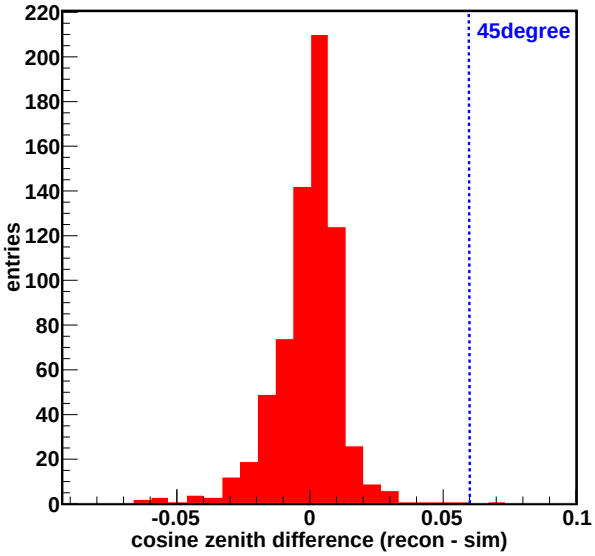

Fig. 67: The zenith angle difference for cosine zenith angle of 0.65. The horizontal axis is the difference of the cosine zenith angle. The vertical axis is the number of events. The blue dot line corresponds to the 45 degrees.

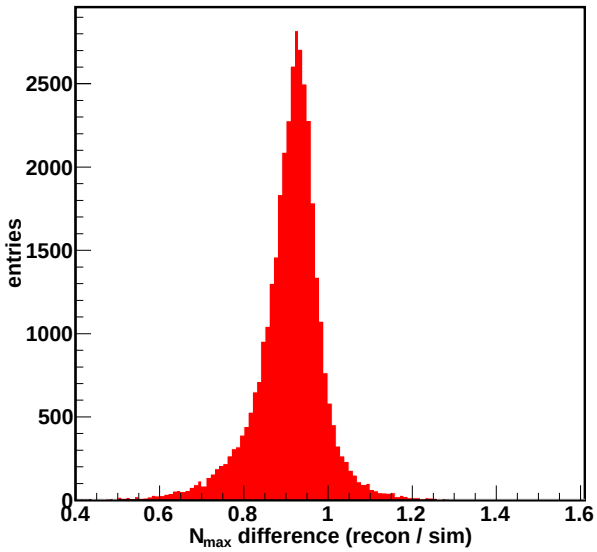

Fig. 68: The N_{max} resolution. Horizontal axis is the ratio of the reconstructed N_{max} to the true N_{max}. The vertical axis is the number of events. The peak value is about -9% and standard deviation is about 8%.

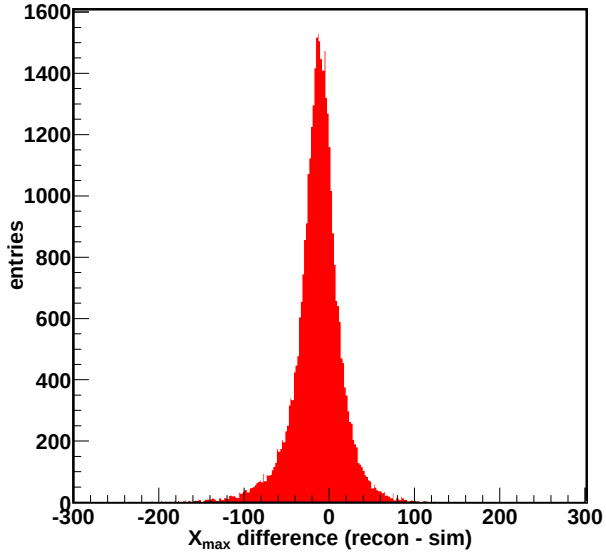

Fig. 69: The X_{max} comparison between simulation true value and reconstructed value. The horizontal axis is the X_{max} difference calculated by reconstructed values subtracted by simulation true value. The vertical axis is the number of events. The peak value is about -13g/cm^2 and one standard deviation is $\sim$ 30g/cm^2.

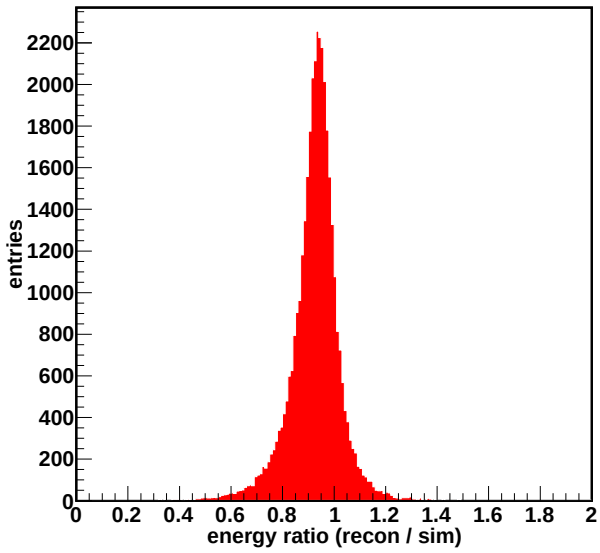

Fig. 70: The energy resolution. The horizontal axis is the ratio of reconstructed energy to the true energy. The vertical axis is the number of events. The peak value is about -8% and one standard deviation is about 8%.

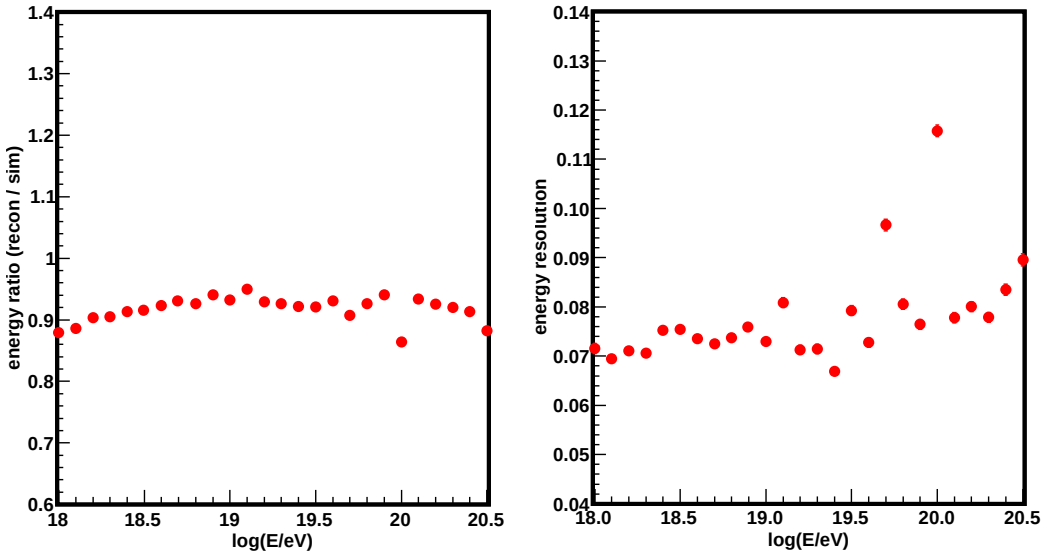

Fig. 71: The left figure shows the energy systematic shift by the reconstruction. The horizontal axis is the energy of the simulation true energy. The vertical axis is the ratio of reconstructed energy to simulation true energy. The systematic difference is about 8% with small energy dependence. The right figure shows the energy resolution for each energy. The horizontal axis is also simulation true energy. The vertical axis is one standard deviation as the energy resolution. The energy resolution is $\sim$ 8%.

8.3 Aperture

In the energy region above $\sim 10^{19}$eV, the aperture of the hybrid events is limited by the deployed SD area. The fluctuation of the aperture is small. But the statistics of the observed event is smaller than FD monocular analysis. In the energy region below $\sim 10^{19}$eV, the aperture is limited by the sensitivity of the FD. In TA configuration, the trigger efficiency of the SD is also reduced around that lower energy range. So the aperture estimation has to be done carefully. The lowest energy, which is limited by the trigger efficiency of the SD, is about 10^{18} eV. But the merit of this analysis is that the resolution of the reconstruction is quite better in this energy range, too.

In the term for using this analysis, there are two trigger conditions of the SD, with/without boundary trigger. The trigger conditions of the SDs are also different in each term. So in this analysis, two types of aperture are prepared, which are without boundary trigger from May 27, 2008 to November 14, 2008 and with boundary trigger from November 15, 2008 to September 28, 2009. The trigger conditions of FD are prepared for the three types: the BR monocular observation, LR monocular observation and stereo observation. For calculating the aperture, both of the slope and the flat MC data are used.

The trigger efficiency for the true core position in the area inside the edge of the array is shown in Fig. 72. It is only for the demonstration, and is not used for this analysis. The trigger efficiency becomes full above the 10^{19}eV.

The trigger efficiency of FD for the SD triggered events is shown in Fig. 73. This efficiency is also full around 10^{19}eV. The trigger aperture for the hybrid events is shown in Fig. 74. The effect of the boundary trigger for the hybrid aperture is small, because the aperture of the FD does not reached the boundary for the lower energy events and most of the air showers which arrive around the boundary are triggered by SD for the higher energy events even without boundary trigger.

The reconstruction efficiency with all quality cuts is shown in Fig. 75. The typical reconstruction efficiency is about 70% $\sim$ 80%. Those values become smaller for the higher energy. It is caused by the condition with which the X_{max} has to be observed, because the X_{max} of the higher energy is sometimes under the ground. For example, the reconstruction efficiency with quality cuts except the X_{max} cut is shown in Fig. 76. The efficiency is about 80% even for higher energy.

By using these studies, the aperture for the hybrid event is obtained as shown in Fig. 77. The aperture at higher energy is about 1000 km^2 sr, which is equivalent to the SD aperture of higher energy.

Since the aperture of lower energy is sensitive to energy, the systematic uncertainty is large. To measure the energy spectrum in this analysis, we set the lower energy at which the trigger efficiency of the SD is greater than 80%. From Fig. 72 and Fig. 73, the lower energy is set as $10^{18.65}$ eV.

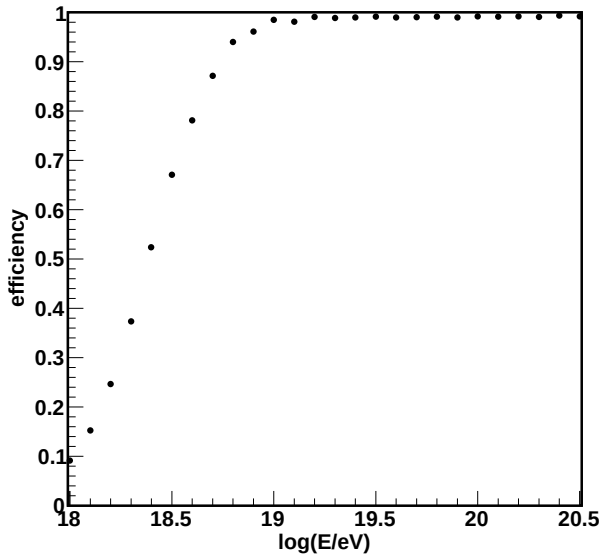

Fig. 72: The trigger efficiency of the SD for the true core position is in the area inside the edge of the array. The horizontal axis is the true energy and the vertical axis is the trigger efficiency. The errors are equivalent of the size of the each data point.

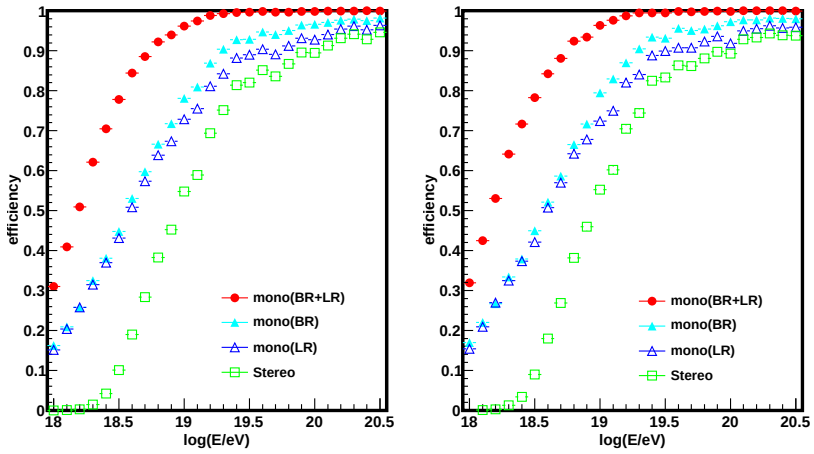

Fig. 73: The trigger efficiency of the FD for the SD triggered events. The left figure is for the trigger condition without boundary trigger and the right figure is for the condition with boundary trigger. The horizontal axis is the true energy of the simulation and the vertical axis is the trigger efficiency. Red filled circles are the efficiency for the events which were triggered by BR or the LR station. Light blue filled triangles are for the BR monocular observation and blue opened triangles are for the LR monocular observation. Green opened squares are for the FD stereo trigger.

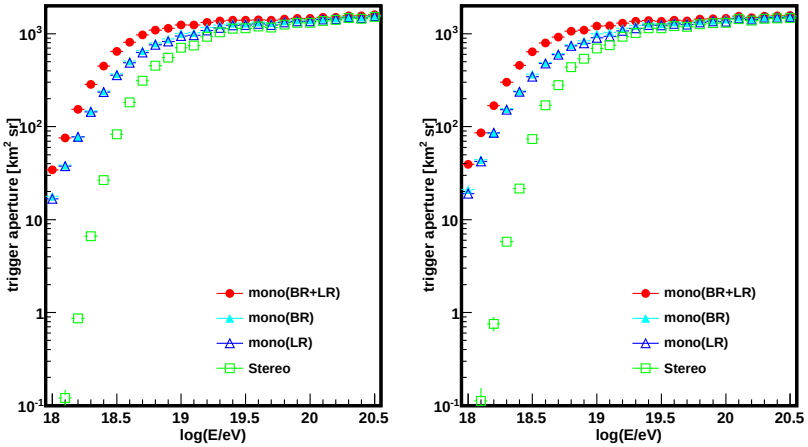

Fig. 74: The trigger aperture for the hybrid events. The left figure is for the trigger condition without boundary trigger and the right figure is for the condition with boundary trigger. The horizontal axis is the true energy of the simulation and the vertical axis is the trigger aperture. Red filled circle is the aperture for the events which were triggered by BR or the LR stations. Light blue filled triangle is for the BR monocular observation and blue opened triangle is for the LR monocular observation. Green opened square is for the FD stereo trigger.

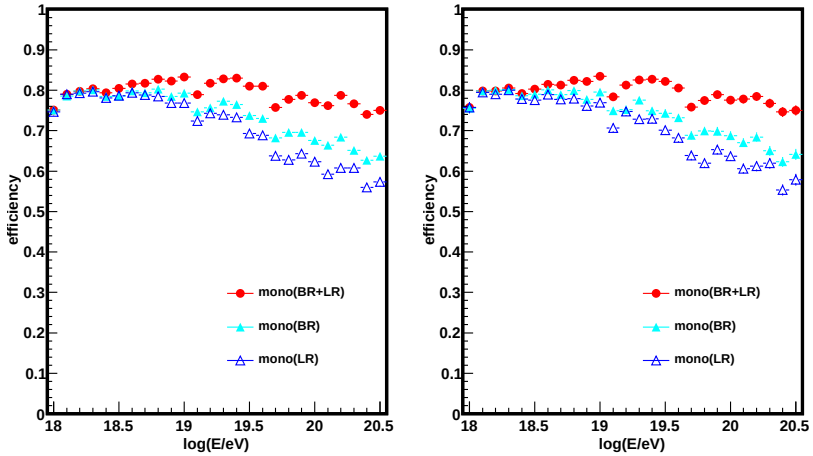

Fig. 75: The reconstruction efficiency with all quality cuts. The left figure is for the trigger condition without boundary trigger and the right figure is for the condition with boundary trigger. The horizontal axis is the true energy of the simulation and the vertical axis is the ratio of the number of the triggered events to that of reconstructed events with all the quality cuts. Red filled circle is the efficiency of the events which were triggered by BR or LR station. Light blue filled triangle is for the BR monocular observation and blue opened triangle is for the LR monocular observation.

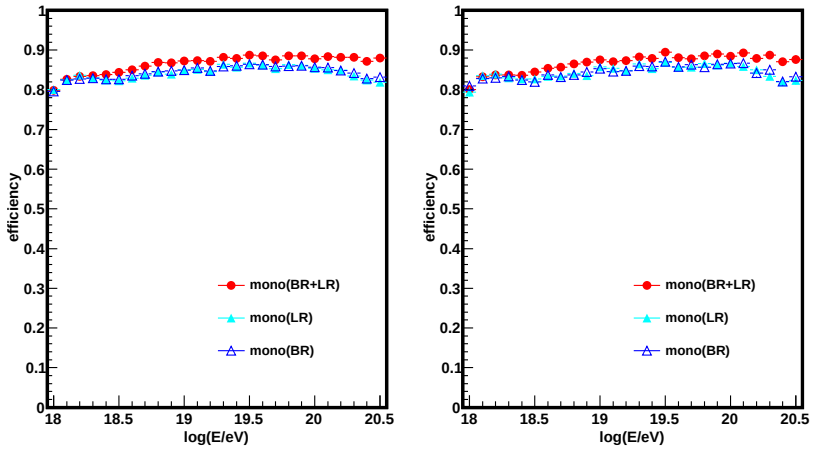

Fig. 76: The reconstruction efficiency with all the quality cuts except the X_{max} cut. The left figure is for the trigger condition without boundary trigger and the right figure is for the condition with boundary trigger. The horizontal axis is the true energy of the simulation and the vertical axis is the ratio of the number of the triggered events to that of the reconstructed events with quality cuts. Red filled circle is the efficiency for the events which were triggered by BR or LR. Light blue filled triangle is for the BR monocular observation and blue opened triangle is for the LR monocular observation.

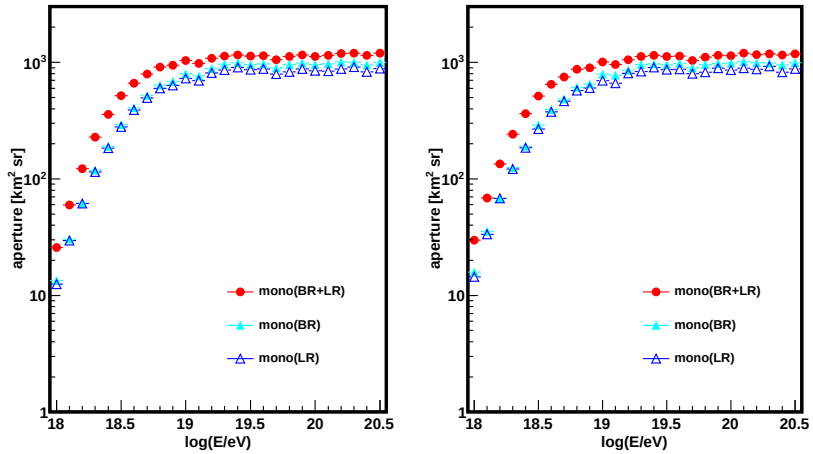

Fig. 77: The aperture for the hybrid events with reconstruction efficiency. The left figure is for the trigger condition without boundary trigger and the right figure is for the condition with boundary trigger. The horizontal axis is the true energy of the simulation and the vertical axis is the aperture. Red filled circle is the aperture for the events which were observed by BR or LR. Light blue filled triangle is for the BR monocular observation and Blue opened triangle is for the LR monocular observation.

8.4 Simple test for the procedure

For the check of the aperture and correction, the simple test for calculating the energy spectrum is done by using MC simulation data. All of the procedures to obtain the energy spectrum, such as reconstruction with quality cuts, energy correction and the usage of obtained aperture, were applied to the MC simulation data with slope $E^{-3.1}$ and compare the obtained slope of the energy spectrum and original one. The result is shown in Fig. 78. The reconstructed spectra are the same as the original spectra. These bias is less than 10% below $10^{19.5}$eV.

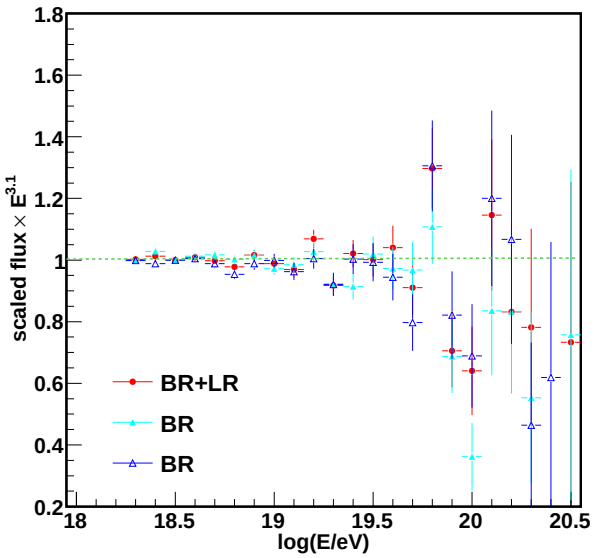

Fig. 78: The obtained energy spectrum from the simulation events with all of the procedure for the data analysis. The horizontal axis is the reconstructed energy and vertical axis is the flux multiplied by $E^{-3.1}$ and scaled at $10^{18.7}$ eV. Red filled circle is the energy spectrum for the events which are observed by BR or LR. Light blue filled triangle is for the BR monocular observation and blue opened triangle is for the LR monocular observation. Green dot line is the guide for the expected value.

9 Data analysis

9.1 Observation term

The TA hybrid observation started in March 2008. However, in the beginning of the hybrid observation term, sometimes the connection between SD and tower had trouble. The stable run started on May 11, 2008 and this analysis uses the term after this time. From Nov 14, 2008, the full operation with the boundary trigger started (Section 3). Because the aperture is different before and after that date, the observation term should be divided at that time for the analysis.

On the other hand, the aperture is also different between FD monocular observation and FD stereo observation. The aperture is obtained for each condition. So the observation period should also be divided by the observation condition of the stereo, only BR and only LR. For example, even when there are the observations both by the BR and LR stations at the same time, there is the observation only by one FD station if the other FD station has dead time. So the observation term should be counted carefully.

The aperture is affected by the cloud. In the TA site, the information of the cloud is recorded by the MD operator every hour which is called WEAT code (Section 4.5.4). The code includes the cloud information of the amount of the cloud in the directions of north, east, south, west and overhead. Since the SDs are located in the direction of south and east from the MD station, the sum of the cloud codes for the directions of east and south is used for the analysis of the observed data in the BR and LR stations. Each code is recorded as 0 or 1. If there is a cloud in the sky of the direction, the code is recorded as 1. In this analysis, only the data with which the sum of the east and south codes is less than 2 are used.

The result of the integrated observation term with dead time and cloud information until Sep 28, 2009 is shown in Fig. 79 and Table. 6. The term is reduced to 63% by the cloud cut. The observation term without boundary trigger is about 265 hours and about 642 hours with boundary trigger. Total observation time without duplication is about 907 hours.

9.2 Hybrid event candidate

The hybrid event search is done by using trigger time of the FD and SD. The search condition is that trigger time difference between FD and SD is less than 200μs. Since the observation methods are different between FD and SD, this event search provides good S/N ratio. The term for the search is from May 27, 2008 to Sep 28, 2009 with cloud cut. The time difference between FD and SD for the selected events is shown in Fig. 80. Almost all of the events are distributed between 0 and 100ns and remaining events are randomly distributed. This distribution proves that these are the hybrid events. The number of events which are found in this method is shown in Table. 7. In almost all the events, the SD detects the air shower faster than the FD. For the UHECRs with higher energy, the time difference becomes larger because the

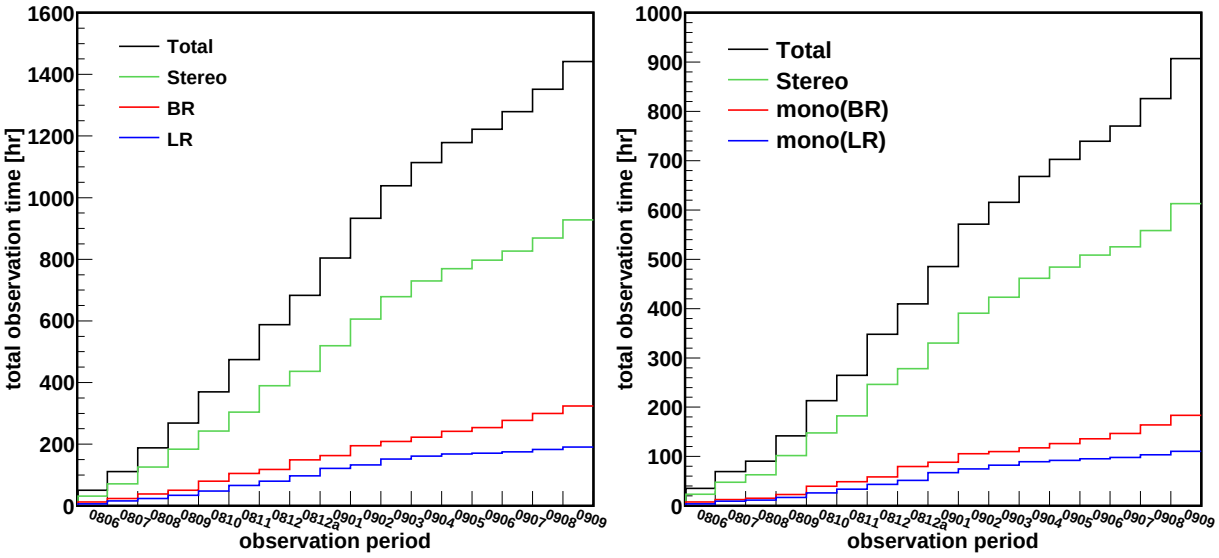

Fig. 79: The total observation time versus observation period for all of the time (left figure) and the time after cloud cut (right figure). The horizontal axis is the observation ID (year/month) and vertical axis is the total observation term in hour. The red line is the term observed only by BR and the blue line is only by LR. The green line corresponds to the stereo observation which is observed both by BR and LR at the same time. There is no overlap between three categories (only BR, only LR, stereo). The black line shows the sum of these categories.

Type	w/o boundary [hr]		w/ boundary [hr]		Sum [hr]	
	cloud cut	(all)	cloud cut	(all)	cloud cut	(all)
BR only	48.67	(104.77)	134.73	(219.14)	183.40	(323.91)
LR only	33.88	(65.98)	76.80	(124.24)	110.68	(190.22)
Stereo	182.25	(303.62)	430.46	(623.96)	612.71	(927.58)
BR (BR only + Stereo)	230.92	(408.39)	565.19	(843.10)	796.11	(1251.49)
LR (LR only + Stereo)	216.13	(369.60)	507.26	(748.20)	723.39	(1117.80)
Total	264.80	(474.37)	641.99	(967.34)	906.79	(1441.71)

Tab. 6: The result of the integration for the observation term for each type. The used term is from May 27, 2008 to Sep 28, 2009. The period of the observation with boundary trigger on 14 Nov 2008. The values with brackets are all of the observation terms and the values without brackets are the time applied by the cloud cut. All values in the table are subtracted by the dead time. BR only and LR only do not include the stereo observation term.

distance of shower axis from the FD becomes longer. About 2000 hybrid events are found with one FD station (monocular-hybrid events) and about 200 events with two FD stations (stereo-hybrid events).

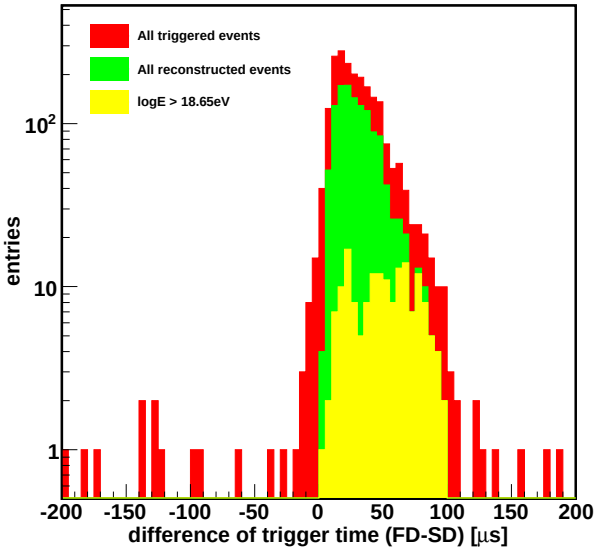

Fig. 80: The distribution of the trigger time difference between FD and SD (FD-SD). The red histogram shows the difference of all triggered events, the green histogram shows the events which are reconstructed by the hybrid analysis, and the yellow histogram shows the events which have the energy above $10^{18.65}$eV.

TYPE	Number of events
BR-SD	967
LR-SD	831
BR&LR-SD	180
Total	1978

Tab. 7: The result of the search for the hybrid event candidates. The number of events for each category doesn't have the duplication.

9.3 The time difference between FD and SD

Since the FD and SD use the same GPS, the time of both detectors is almost synchronized. But the precision less than 1μs is required for the hybrid reconstruction. So we estimate the time difference between FD and SD by the observed data.

The time difference is obtained by the stereo-hybrid events. The simple method is the comparison of the reconstructed events between BR and LR with the reconstructed geometry for each time difference.

About 100 events are reconstructed both by BR and LR with the quality cut (Section 7). The dependence of time difference between FD and SD on the difference of opening angle and core-position on the ground between reconstructed shower axis for the BR data and that for the LR data are shown in Fig. 81. The time difference which shows the smallest difference is around 0μs. The resolutions for the observed data are also consistent with those for the MC data. Since the number of stereo-hybrid events is not enough, this analysis doesn't have the resolution for the decision of the time difference. In this analysis, the value of 0us is used as the time difference between FD and SD.

9.4 Comparison of the data and Monte Carlo

After all of the analyses with quality cut and energy cut ($E > 10^{18.65}$eV), 124 events remain. This sample consist of 87 events which are reconstructed by BR, 79 events which are reconstructed by LR, and 42 events which are reconstructed by both of them. The differences of the trigger time of these events are also shown in Fig. 80. To check on the agreement between the observed data and MC data, the number of selected PMTs obtained by the pre-reconstruction (Fig. 82), number of clustered SDs (Fig. 83), the shower axis obtained by geometrical reconstruction (Fig. 84 $\sim$ Fig. 91), and the shower profile obtained by longitudinal reconstruction (Fig. 92 $\sim$ Fig. 97), are compared between the observed data and the simulated events which are generated by the slope of the $E^{-3.1}$. The distributions of the experimental data show good agreement with those generated by the MC simulation.

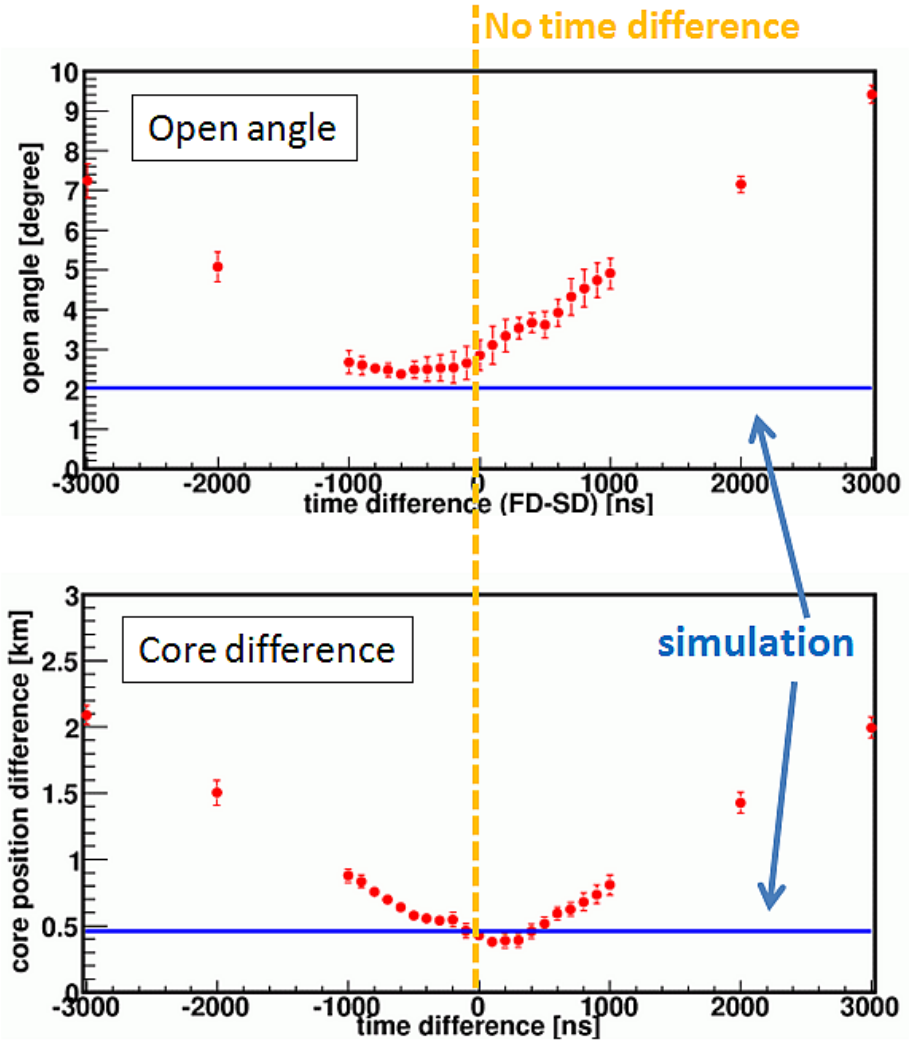

Fig. 81: The result of the comparison with the reconstructed geometry both by BR and LR independently for the Stereo-Hybrid events. The upper figure shows the opening angle. The horizontal axis is the time difference between FD and SD (FD-SD). The vertical axis is the opening angle between the reconstructed shower axes reconstructed by the BR and LR data. The lower figure shows the difference of the core position on the ground. The horizontal axis is also the time difference and the vertical axis shows the difference of the core position between the reconstructed geometry by BR and LR. The red points show the result of the experimental data. The blue line shows the result of the same procedure for the simulation data. The yellow vertical dashed line shows the position of the no-time difference between FD and SD.

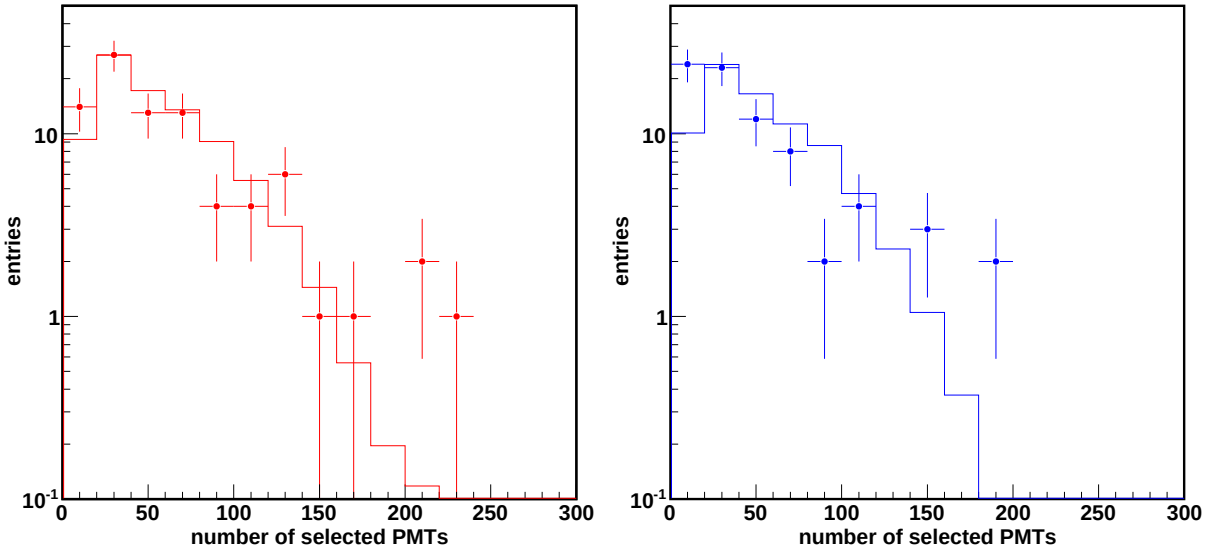

Fig. 82: The distribution of the numbers of selected PMTs. The left figure is for the BR station and the right figure is for the LR station. The horizontal axis is the number of selected PMTs by pre-reconstruction and the vertical axis is the number of events. The filled circles are the data and the histograms are simulated events scaled to the number of events of the data.

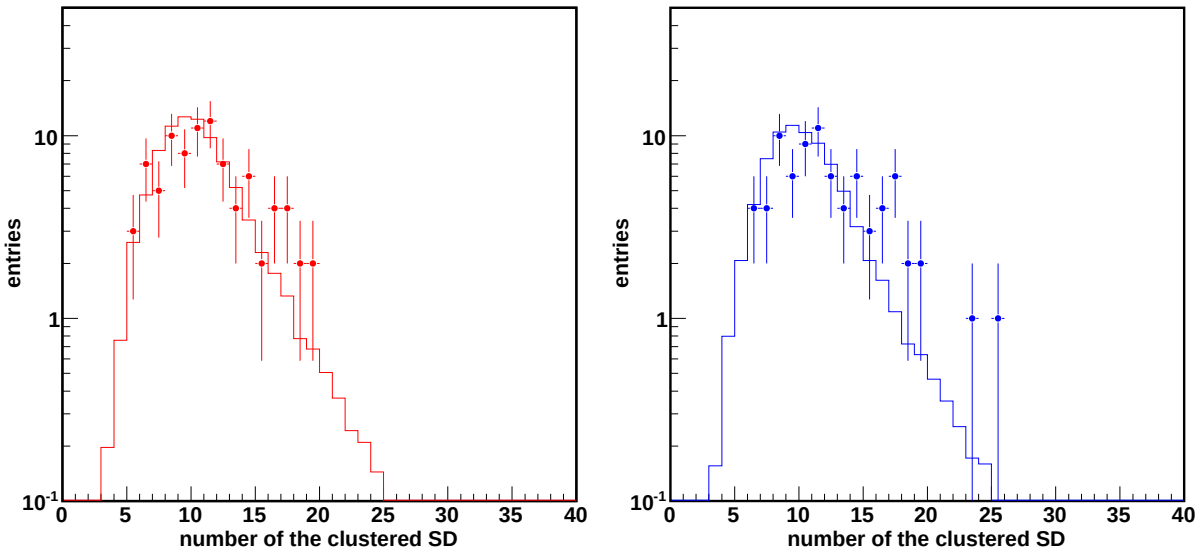

Fig. 83: The distributions of the numbers of clustered SDs. The definition of the clustered SDs is the number of neighboring SDs with energy deposit above 0.3 MIPs around the triggered SD. The left figure is the comparison for the BR station and the right figure is for the LR station. The horizontal axis is the number of clustered SDs and the vertical axis is the number of events. The filled circles are the data and the histograms are simulated events scaled to the number of events of the data.

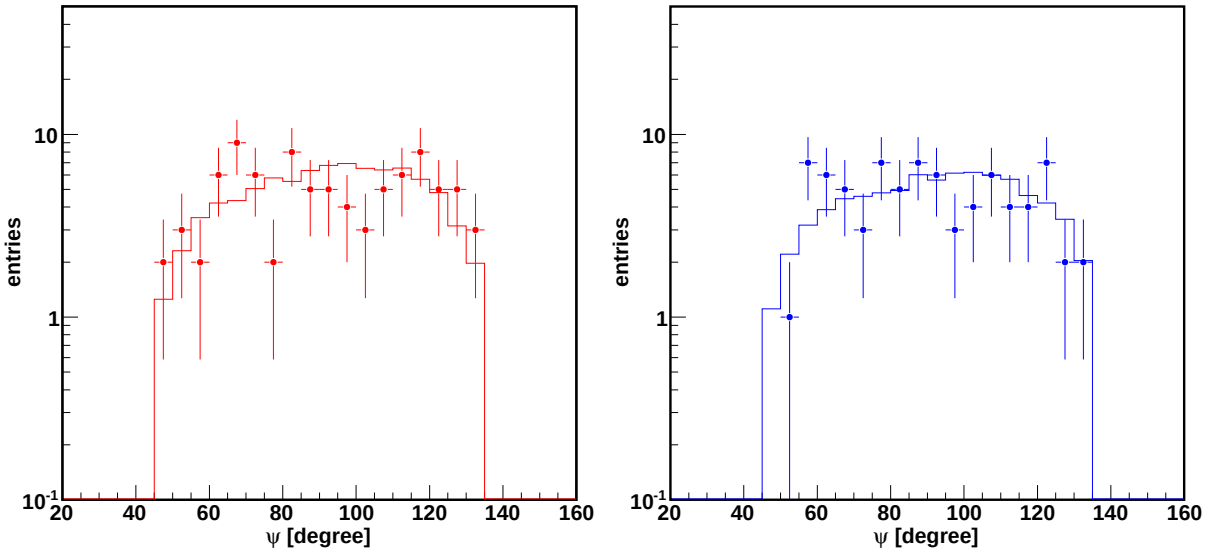

Fig. 84: The distributions of the elevation angle on the SDP (ψ) described in Eq. 59. The left figure is for the BR station and the right figure is for the LR station. The filled circles are the data and the histograms are simulated events scaled to the number of events of the data.

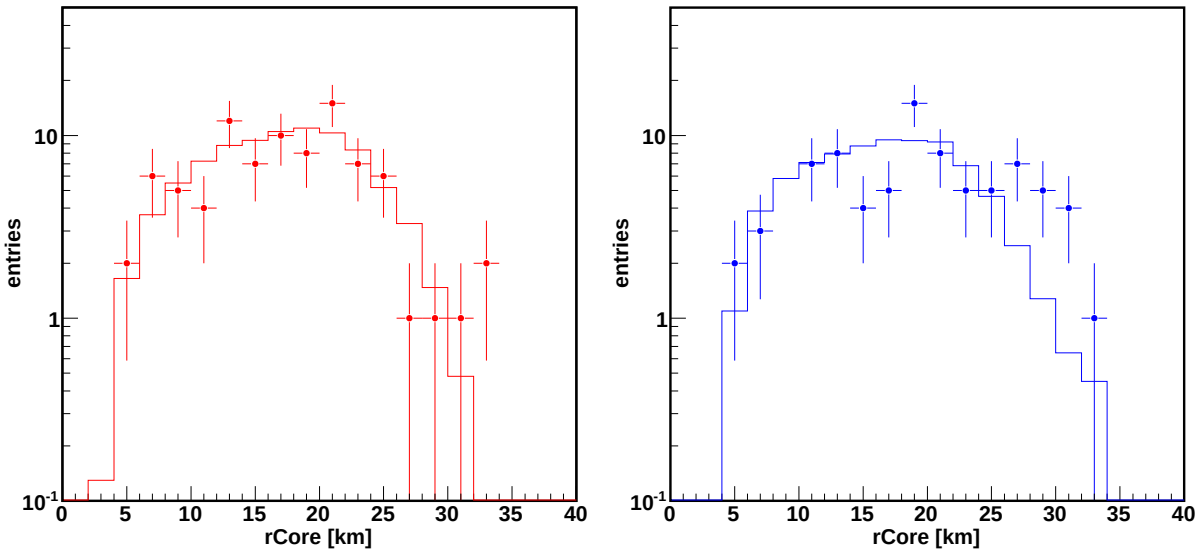

Fig. 85: The distributions of the distance from the FD station to the core position (R_{core}) described in Eq. 59. The left figure is the comparison for the BR station and the right figure is for the LR station. The filled circles are the data and the histograms are simulated events scaled to the number of events of the data.

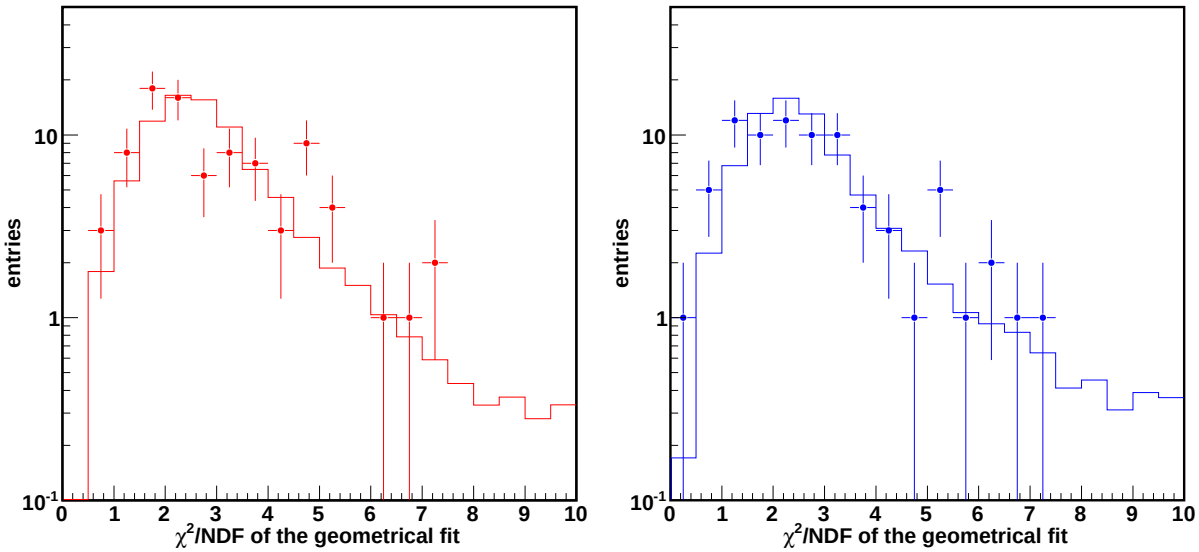

Fig. 86: The distributions of χ^2 described in Eq. 62. The left figure is for the BR station and the right figure is for the LR station. The filled circles are the data and the histograms are simulated events scaled to the number of events of the data.

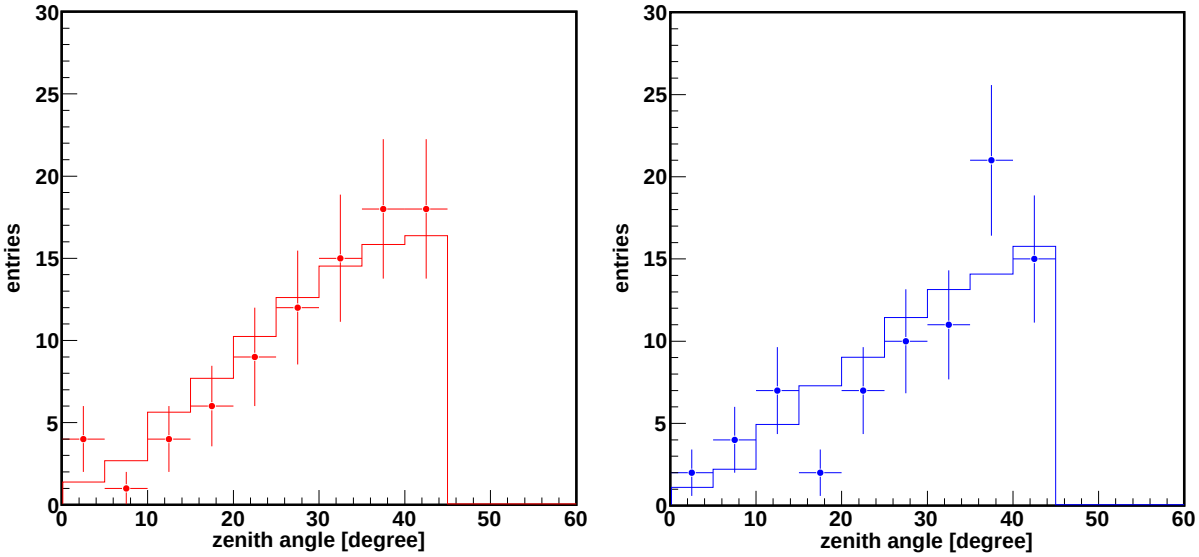

Fig. 87: Zenith-angle distributions for the BR station (left) and for the LR station (right). The filled circles are the data and the histograms are simulated events scaled to the number of events of the data.

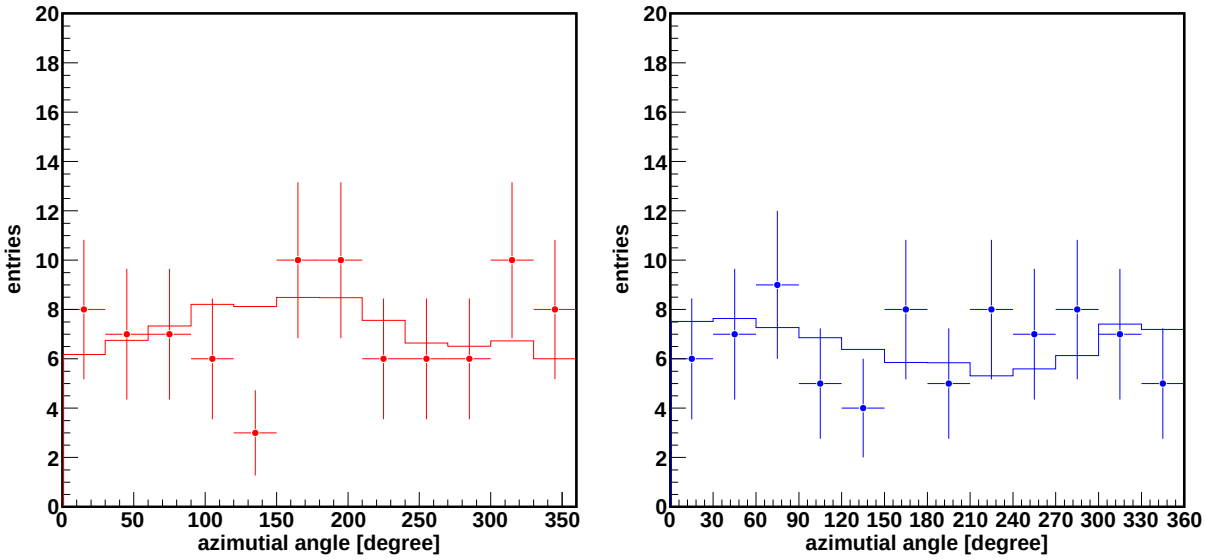

Fig. 88: The distributions of the azimuth angle of the reconstructed shower axis. The left figure is for the BR station and the right figure is for the LR station. The filled circles are the data and the histograms are simulated events scaled to the number of events of the data.

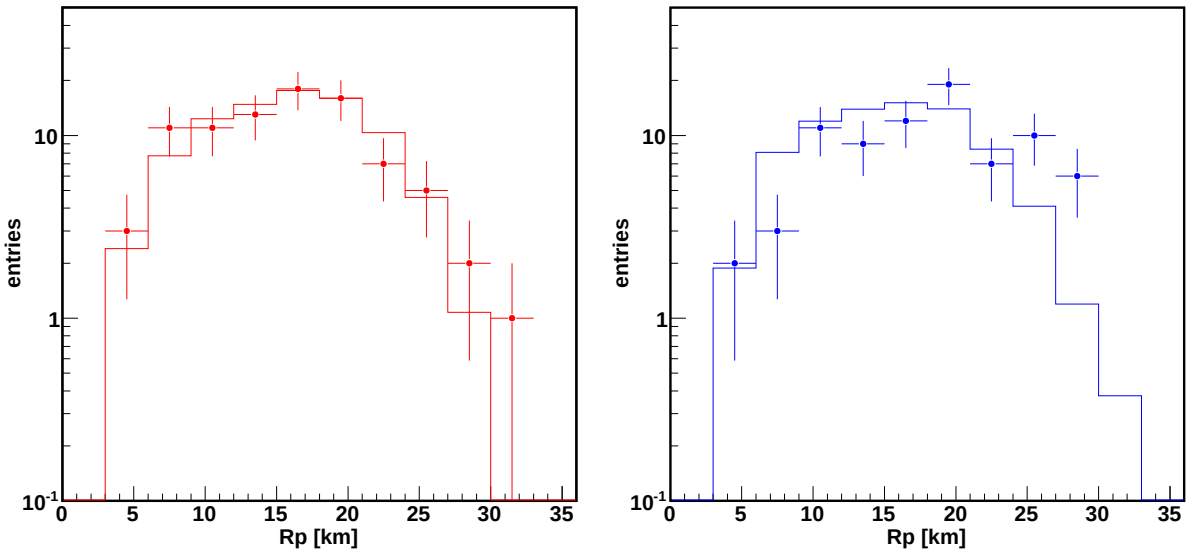

Fig. 89: The distributions of the distance of the reconstructed shower axis from the FD station (R_p). The left figure is for the BR station and the right figure is for the LR station. The filled circles are the data and the histograms are simulated events scaled to the number of events of the data.

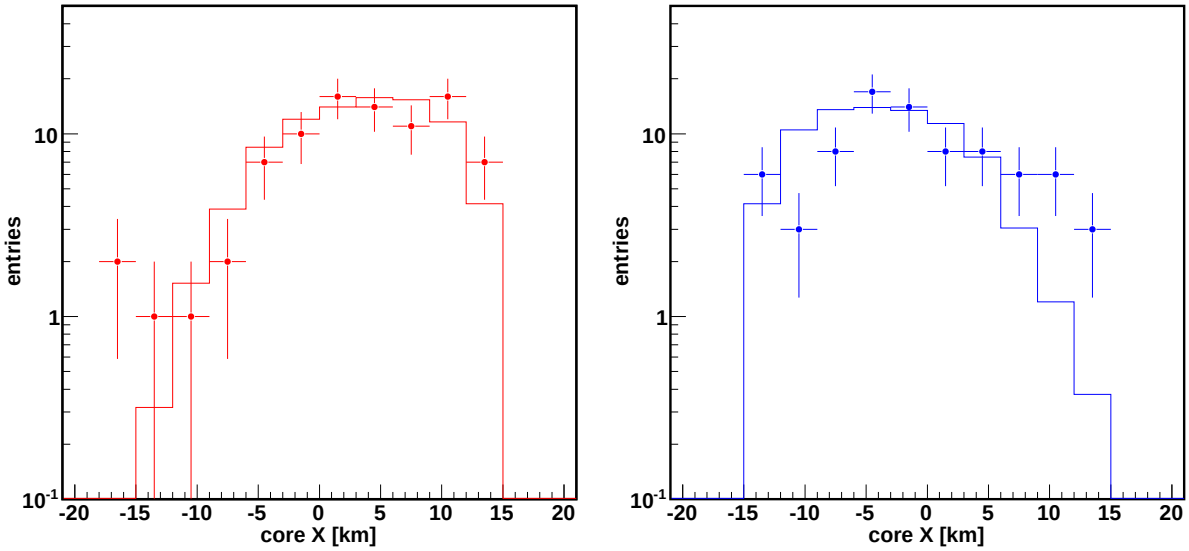

Fig. 90: The distributions of the reconstructed shower core position along the X axis (from west to east). The left figure is for the BR station and the right figure is for the LR station. The filled circles are the data and the histograms are simulated events scaled to the number of events of the data.

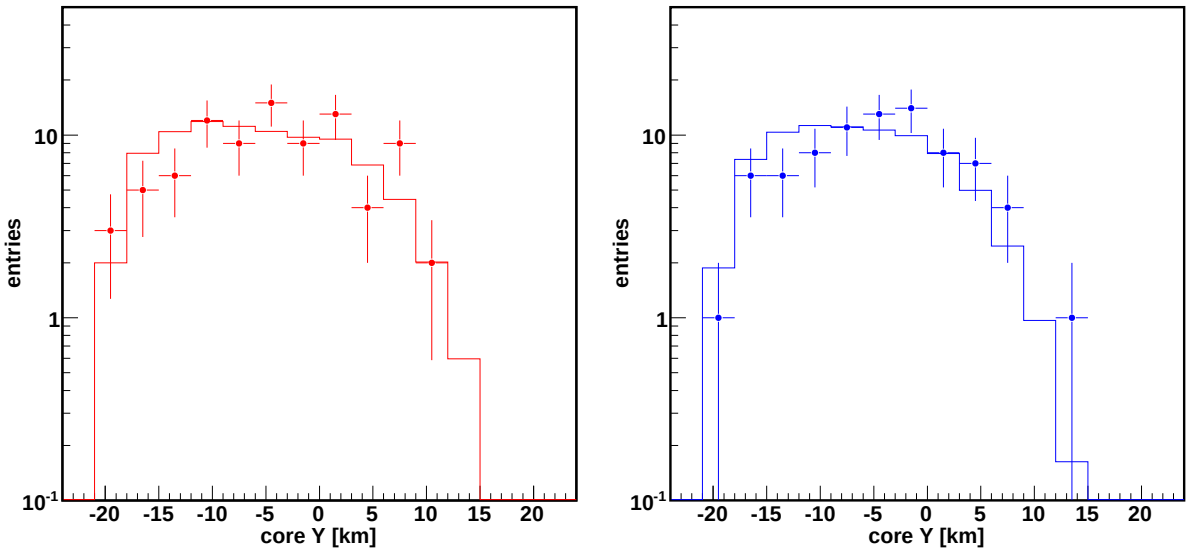

Fig. 91: The distributions of the reconstructed shower core position along the Y axis (from south to north). The left figure is for on the BR station and the right figure is for the LR station. The filled circles are the data and the histograms are simulated events scaled to the number of events of the data.

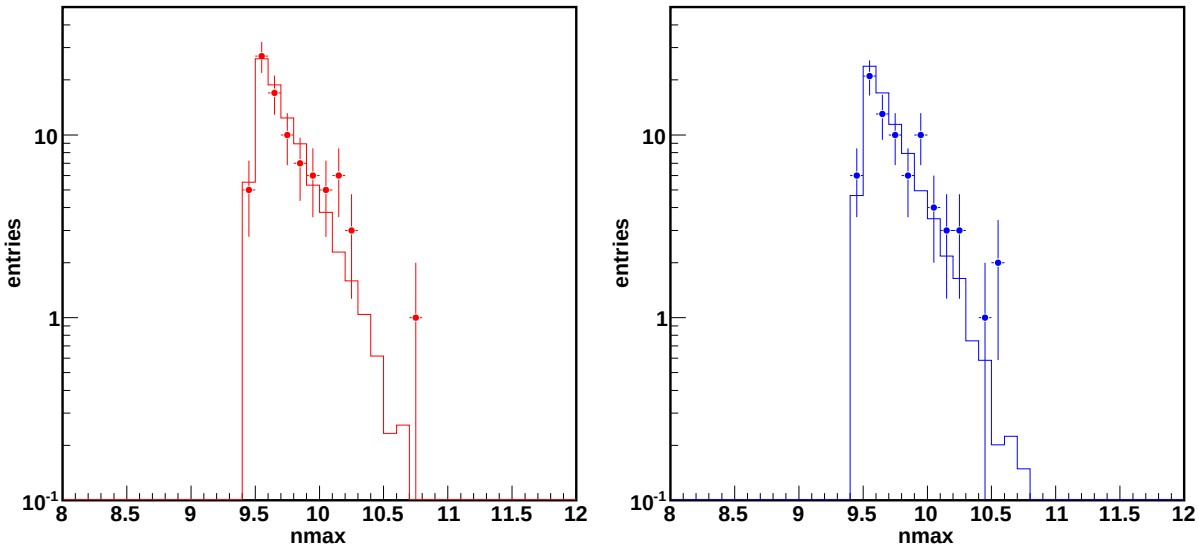

Fig. 92: The distributions of with the reconstructed N_{max} described in Eq. 14. The left figure is for the BR station and the right figure is for the LR station. The filled circles are the data and the histograms are simulated events scaled to the number of events of the data.

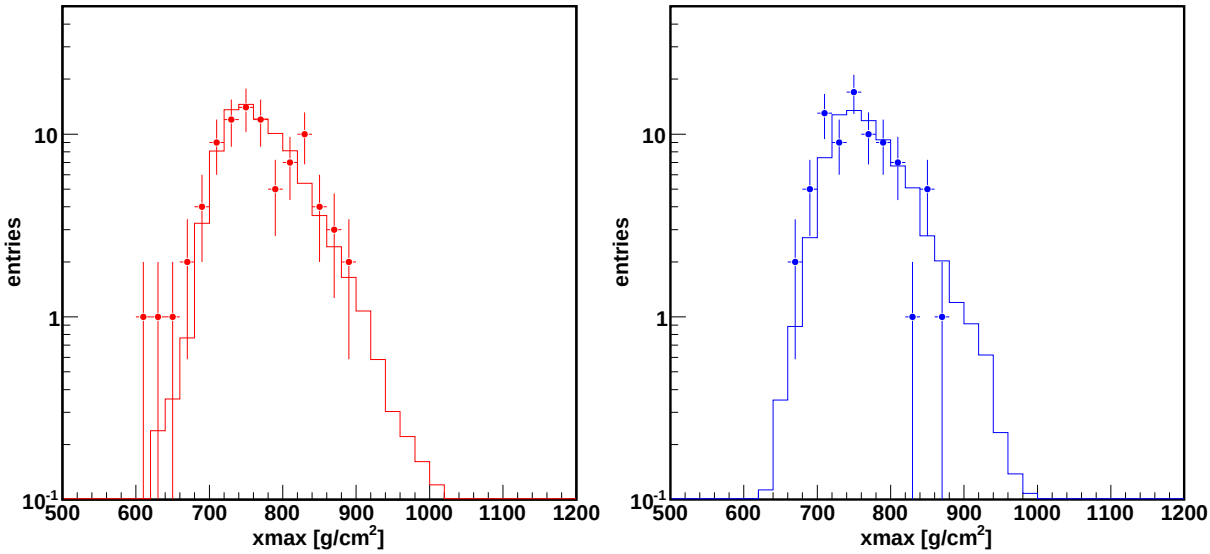

Fig. 93: The distributions of the reconstructed X_{max} described in Eq. 14. The left figure is for the BR station and the right figure is for the LR station. The filled circles are the data and the histograms are simulated events scaled to the number of events of the data.

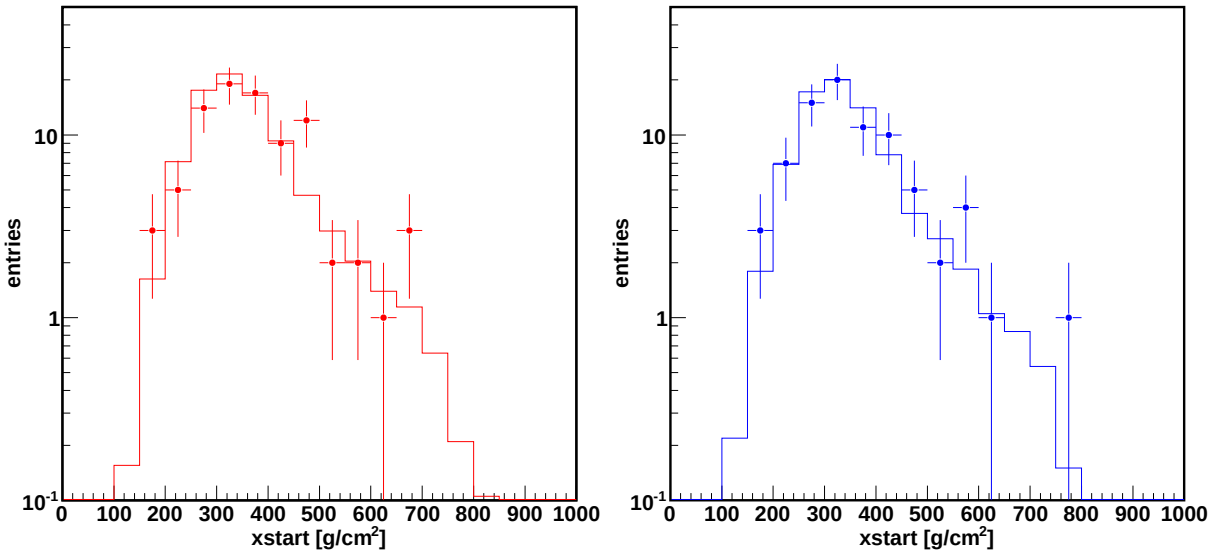

Fig. 94: The distributions of the observed depth of the shower starting position. The left figure is for the BR station and the right figure is for the LR station. The filled circles are the data and the histograms are simulated events scaled to the number of events of the data.

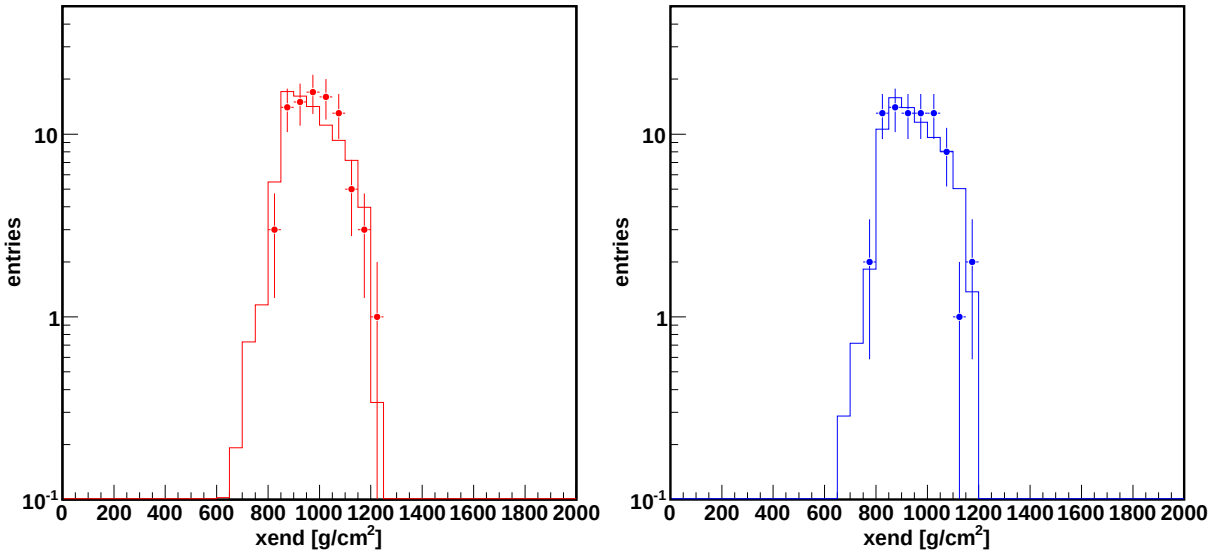

Fig. 95: The distributions of the observed depth of the shower end position. The left figure is for the BR station and the right figure is for the LR station. The filled circles are the data and the histograms are simulated events scaled to the number of events of the data.

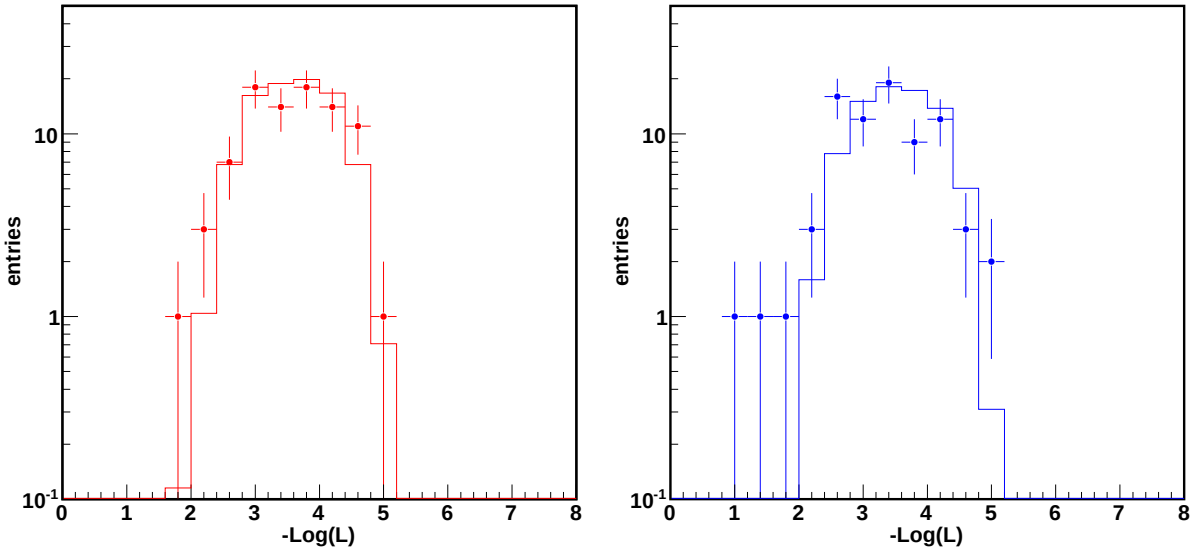

Fig. 96: The distributions of logarithm of the likelihood (-Log(L)) for the longitudinal fitting (Eq. 67). The left figure is for the BR station and the right figure is for the LR station. The filled circles are the data and the histograms are simulated events scaled to the number of events of the data.

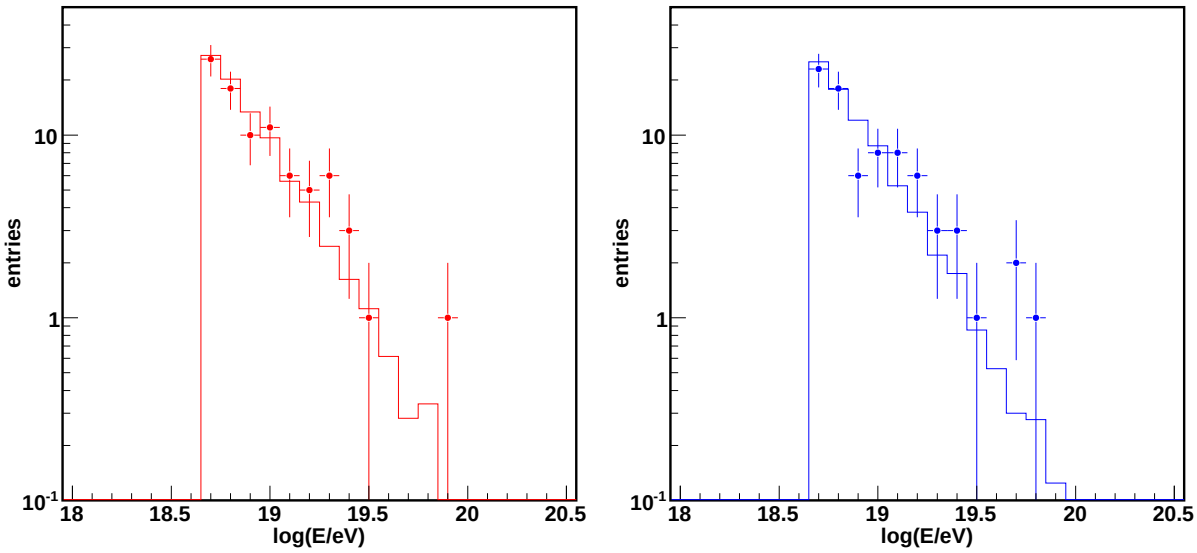

Fig. 97: The distributions of the reconstructed energy after the correction of the systematic energy shift (see Fig. 71). The left figure is for the BR station and the right figure is for the LR station. The filled circles are the data and the histograms are simulated events scaled to the number of events of the data.

9.5 The energy resolution by the stereo-hybrid events

The resolution is also estimated by the stereo-hybrid events. Since the reconstruction for the BR data and that for the LR data are independent, the difference of the reconstructed parameters of the same event has the information of the resolution. The reconstruction, calibration and analysis are same between the BR and LR data, the resolution of these stations should be the same. So the obtained difference σ_{BR+LR} is created by superposition of the resolution for the BR σ_{BR} and that for the LR σ_{LR}:

$$\sigma_{BR+LR} = \sqrt{\sigma_{BR}^2 + \sigma_{LR}^2}. \tag{71}$$

The result of the comparison with the reconstructed energy between BR and LR is shown in Fig. 98. Since the RMS of the distribution is 28%, the energy resolution for a single FD station is estimated as $\sim$ 20% by Eq. 71. The energy resolution of the experimental data is larger than that of the MC simulation which is 13%. The reason is clearly. The result of the data includes the other effects which are not included in MC. For example, the typical value is used for the attenuation of the Mie scattering. The result of the data includes the variation of the atmosphere. There are also other effects such as cloud, time difference between FD and SD, and difference of the calibration constant between BR and LR. So it is conceivable that the resolution obtained for the observed data by this method is worse than that for the MC simulations.

9.6 Examples of the events with large energy

In the reconstructed events, there are two events with energy above $10^{19.7}$ eV. The event display and result of the reconstruction for each event are shown in Fig. 99 and Fig. 100.

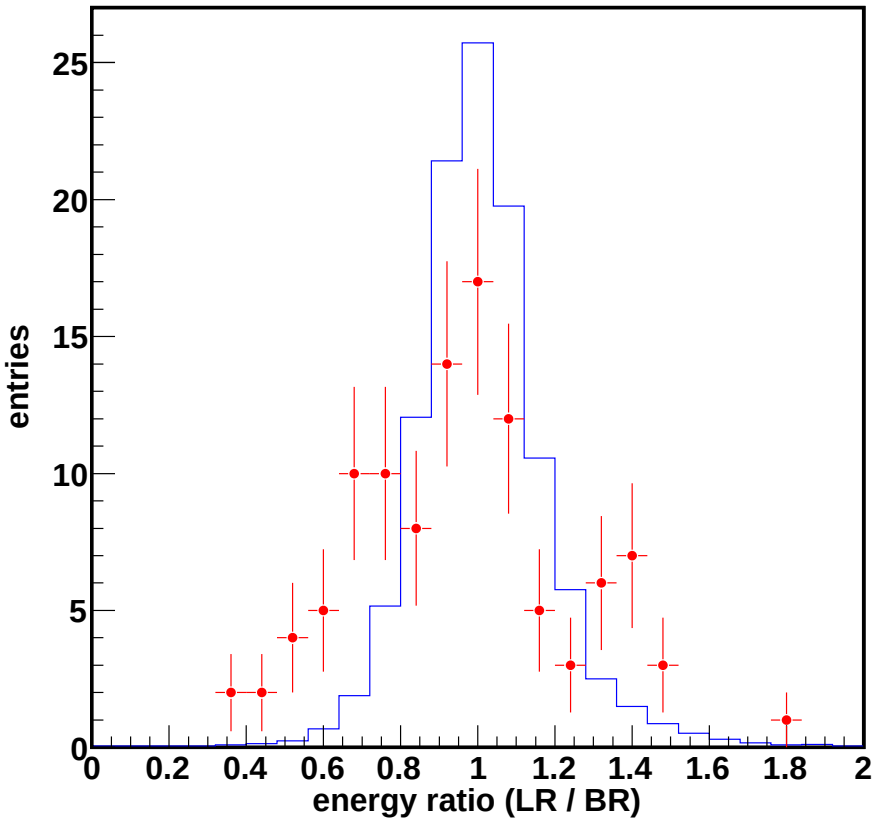

Fig. 98: The distribution of the ratio of the energy reconstructed by BR to that by LR for the stereo-hybrid events. The horizontal axis is the ratio of the energy reconstructed by LR to that by BR and the vertical axis is the number of events. The red points represent the experimental data and the blue line shows the simulated data. The area of simulated data is normalized to the number of experimental data. The RMS of the distribution is 13% for the MC simulation and 28% for the data.

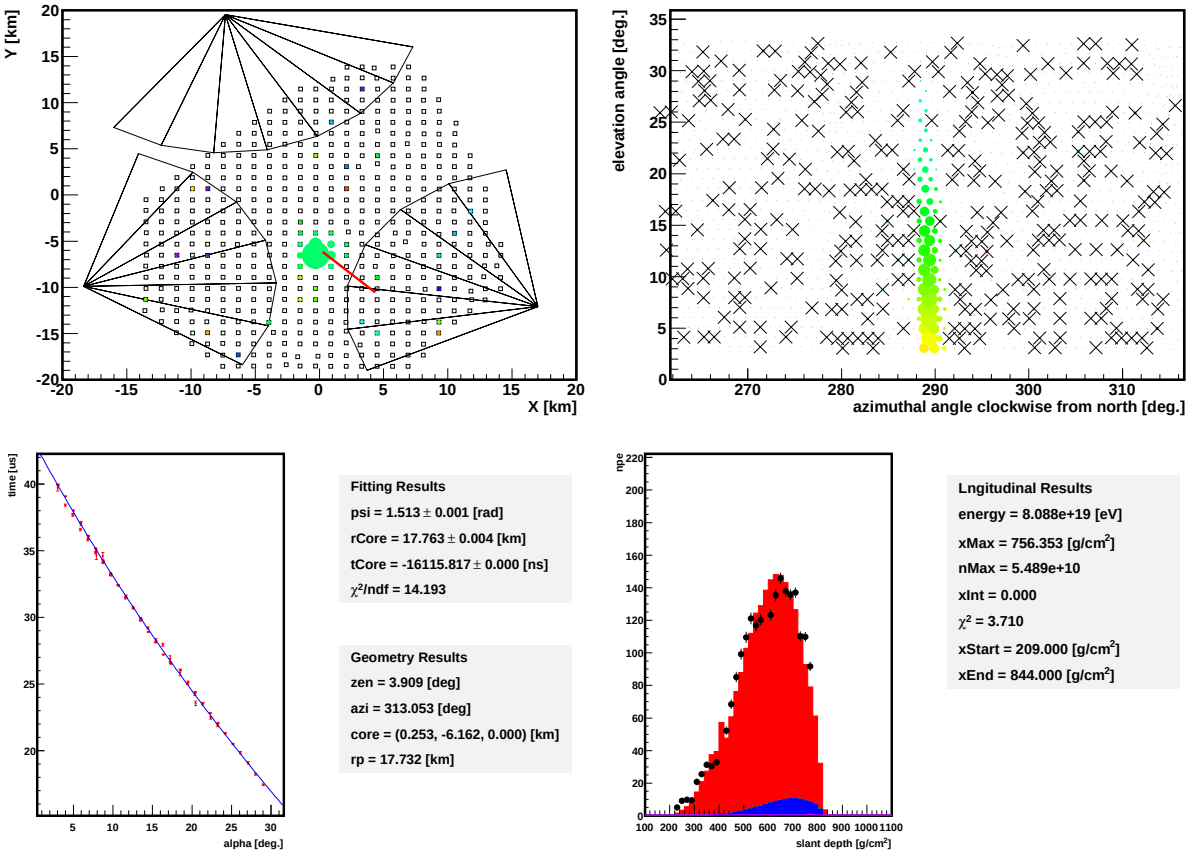

Fig. 99: The example of the high energy event observed on December 30, 2008 in the BR station. The left upper figure shows the hit map for the SDs. Open squares are the positions of all the SDs, color of the filled circles is the timing and the size is the number of photo electrons deposited in the scintillator, the black lines are the field of view for each FD. The horizontal and vertical axes are the positions on the TA site. The red line is the reconstructed shower axis. The right upper figure shows the hit map for FD. The horizontal and vertical axes represent the direction of each PMT. The black dots are the PMTs with the S/N above 3σ, the cross marks are the rejected PMTs by the pre-reconstruction, the filled circles are the selected PMTs. The color is the timing and the size is the detected photo electrons. The left lower figure shows the result of the geometrical reconstruction. The horizontal axis is the elevation angle on the SDP and the vertical axis is the timing. The red points are the experimental data and the blue line is the fitted function of Eq. 59. The right lower figure shows the result of the longitudinal reconstruction. The horizontal axis is the slant depth and the vertical axis is the number of detected photo electrons. The black points are the data, the red filled histogram is the fitted light curve by IMC (see Eq. 67) and the blue filled histogram is the scattered Cherenkov of the Rayleigh scattering.

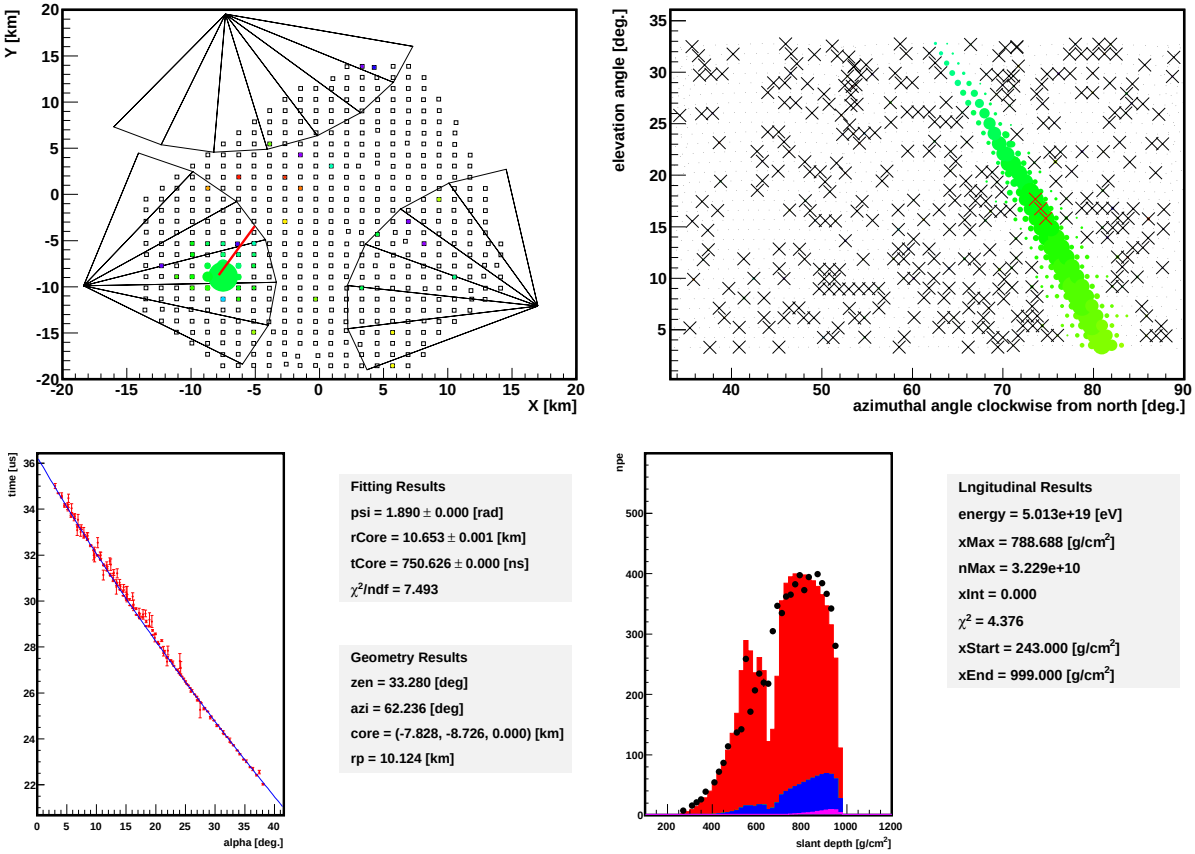

Fig. 100: The example of the high energy event observed on Sep 19, 2009 in the LR station. The red crosses on the right upper figure are the rejected PMTs by the 4th selection of the pre-reconstruction step. Since this rejection is also used in the IMC method, the reconstructed energy is not affected by this selection.

10 Energy spectrum

10.1 Exposure

The total exposure is calculated for the total observation term (Section 9.1) and the aperture is calculated from the MC simulations as described in Section 8.3. The exposure Ex_i for each energy bin E_i is calculated by:

$$Ex(E_i) = A(E_i)T, \tag{72}$$

where $A(E_i)$ is the aperture for E_i and T is the effective observation term. The largest exposure is obtained by combining the apertures for the stereo observation, BR monocular observation and LR monocular observation. But for the verification, the exposure of the BR monocular observation alone and that of the LR monocular observation alone are also prepared. The results of the exposure are shown in Fig. 101. Since the covering area of the SD by the BR station is larger than that by the LR station and the observation time of the BR station is also larger than that of the LR station, the exposure of the BR station is larger than that of the LR station. The exposure at the 10^{19} eV is about 3×10^{15} m^2 sr s. It is equivalent to about 6% of the AGASA exposure (5.1×10^{16} m^2 sr s [1]).

10.2 Energy spectrum

In this analysis, the energy spectrum with the energies above $10^{18.7}$ eV is obtained. The flux for each energy $J(E_i)$ is calculated by:

$$J(Ei) = \frac{N(E_i)/\Delta E_i}{Ex(E_i)}, \tag{73}$$

where $N(E_i)$ is the number of events for E_i bin and ΔE_i is the bin width of the E_i. The $N(E_i)$ is shown in Fig. 102. When the event is reconstructed both by BR and LR with quality cuts, the event which has larger number of selected PMTs is selected. The flux J(E) obtained by using Fig. 101 and Fig. 102 is shown in Fig. 103.

The common method of displaying the UHECR flux is to multiply each bin by a factor of E^3 spectrum. However, the normalization is so sensitive to the energy shift. For example, if the systematic shift of energy is 20%, the normalization of $E^3J(E)$ shifts factor 1.7. The obtained $E^3J(E)$ is shown in Fig. 104. The fluxes observed by BR and LR are consistent within the error bars. There are empty bins around the high energy region. Since empty bins may cause misunderstanding for the flux of the high energy, the bin width is changed above $10^{19.5}$ eV. The measured spectrum with the combination of the events which are observed by BR and LR is shown in Fig. 105. The energy spectrum of this analysis together with the other previously published results are also shown in Fig. 106

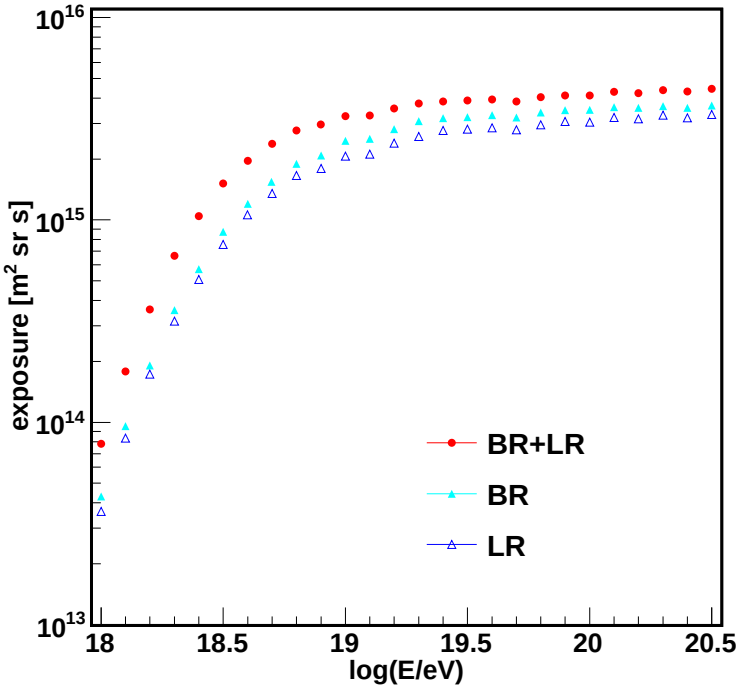

Fig. 101: The exposure for the hybrid event between May 27, 2008 and Sep 28, 2009. The horizontal axis is the energy of the primary cosmic rays and the vertical axis is the exposure. The red circles represent the exposure for which the stereo observation term $\times$ stereo aperture, only BR observation term $\times$ BR aperture and only LR observation term $\times$ LR aperture are combined. The light blue triangles represent the BR monocular exposure and the blue opened triangles represent the LR monocular exposure.

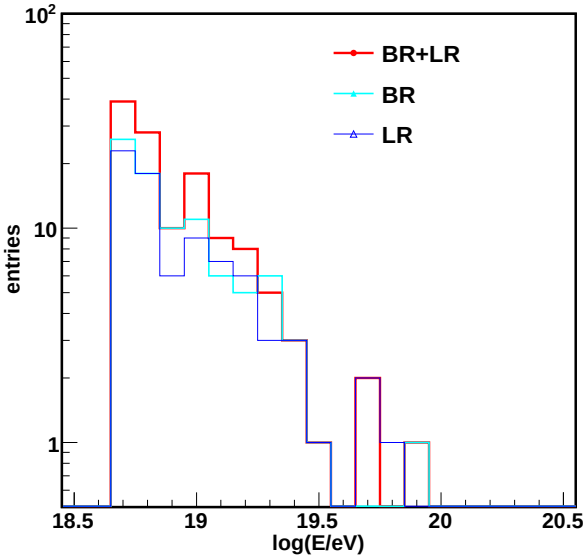

Fig. 102: Distribution of reconstructed $\log_{10}$E for the events above $10^{18.7}$eV after quality cuts. The red histogram is the sum for the BR and LR events. When the same event is reconstructed both by BR and LR, the event which has larger number of selected PMTs is selected. The light blue histogram represents the distribution for the events reconstructed by BR and the blue histogram represents that by LR.

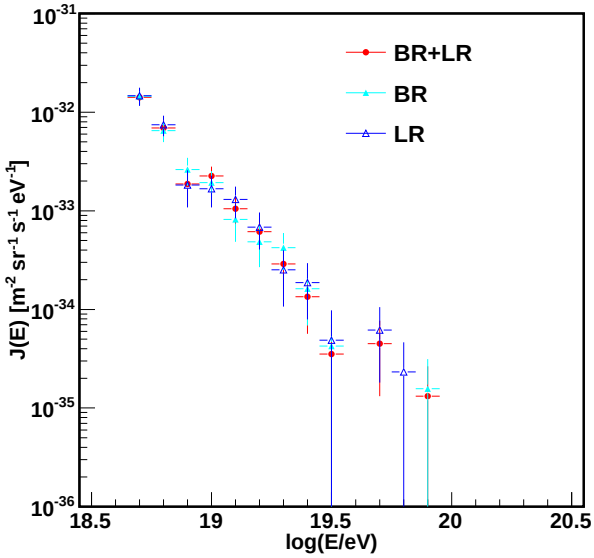

Fig. 103: The cosmic ray flux measured by the hybrid event. The horizontal axis is the energy of the primary cosmic rays and the vertical axis is the flux J(E). The red filled circles are obtained by combining the BR and LR events, the light blue open triangles are obtained by using the events observed by BR and the blue filled triangles are by LR.

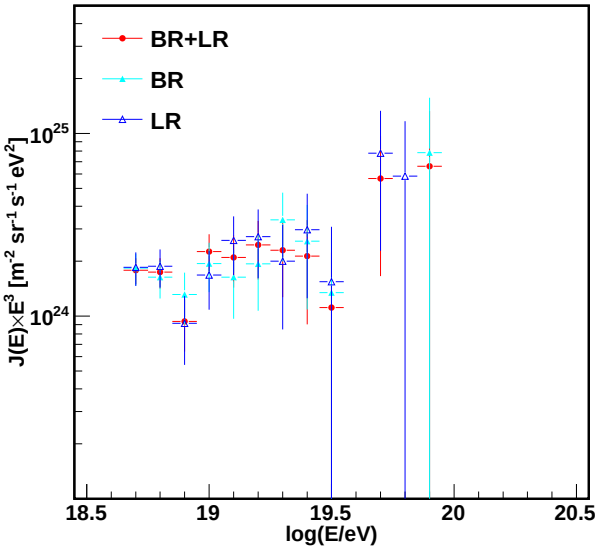

Fig. 104: The cosmic ray flux multiplied by a factor of E^3 for each bin. The horizontal axis is the energy of the primary cosmic rays and the vertical axis is the flux $J(E)\times E^3$. The red filled circles are obtained by combining the BR and LR events, the light blue open triangles are obtained by using the events observed by BR and the blue filled triangles are by LR.

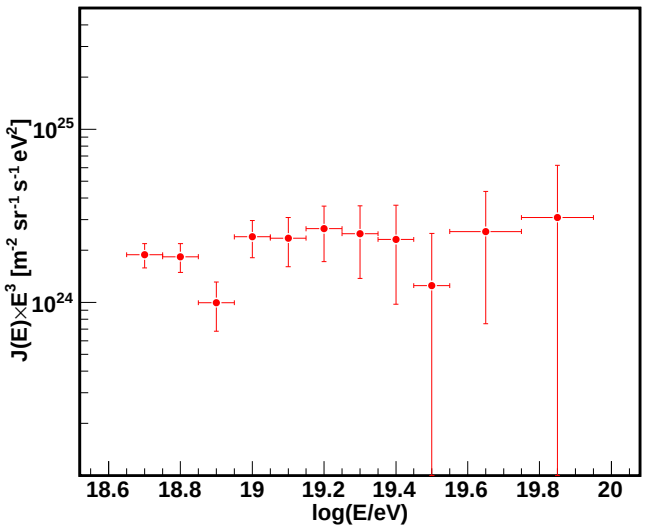

Fig. 105: The cosmic ray flux multiplied by a factor of E^3 for each bin. The horizontal axis is the energy of the primary cosmic rays and the vertical axis is the flux $J(E)\times E^3$. The red filled circles are obtained by combining the BR and LR events. The bin width is twice above the $10^{19.5}$eV.

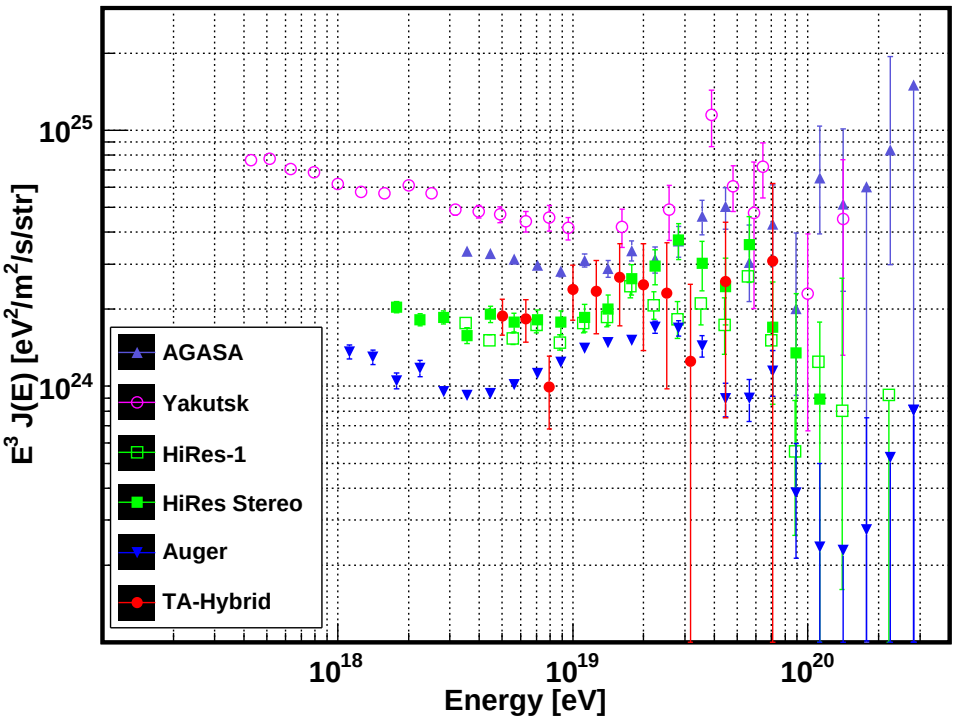

Fig. 106: The cosmic ray flux multiplied by a factor of E^3 for each bin by this analysis together with the previously published results by other experiments. The horizontal axis is the energy of the primary cosmic ray and vertical axis is the flux $J(E)\times E^3$. The red filled circles represent the result of this analysis (Fig. 105). The purple filled triangle represent the result by AGASA[1]. The light red opened circles represent result by Yakutsk[51]. The light green open squares represent the result by HiRes-1[2]. The light filled squares represent the result by HiRes Stereo[2]. The blue filled triangles represent the result by Auger[8].

11 Study of systematic error

11.1 Accidental trigger of SD

The detector MC for the SD does not include the triggered SD with noise hit. The trigger condition of the SD is three neighboring SDs with the signal above three MIPs. There can be two SDs with the signal above three MIPs and the other SD with signal smaller than 3 MIPs. If there is the noise hit SD above 3MIPs which neighboring the other two detectors, the SD are triggered as the real data but not triggered in the simulation. It causes the underestimation for the aperture of the small energy. So the accidental trigger rate is estimated.

The noise rate above 3 MIPs is less than 20Hz and the gate width to search for the SDs above 3MIPs is 8μs. The neighboring SDs around the two SDs are six. The probability of the accidental trigger is $20 \times 8 \times 10^{-6} \times 6 \simeq 0.1\%$. So this factor is negligible to measure the energy spectrum.

11.2 Fluorescence yield model

There are several models for the fluorescence yield. The models include the absolute yield and dependence for the atmospheric parameters. The comparison of the models is shown in Fig. 107. The maximum difference of the models is about 20%. Each model has the systematic error with $\pm$ 10% $\sim$ 15%. The errors are caused mainly by the calibration of the photo detector. Thus each result of the measurement is consistent within the systematic error. We use the differential spectrum by FLASH and total yield by Kakimoto et al. The amount of emitted photons of this model is the smallest among all the models.

The HiRes used the kakimoto-bunner model in Fig. 107. The difference of the fluorescence yield between this analysis and the HiRes analysis is about 3%. To compare the measured energy spectrum with the result of HiRes, this difference has to be considered. This difference does not affect the energy directly, because the wavelength dependence is also different. In this study, the spectrum with 3% fluorescence yield increment is prepared as the spectrum with maximum effect (Fig. 108). The reconstructed energy and trigger efficiency of FD are affected by this systematic difference. The HiRes spectrum is in between the original spectrum obtained by the hybrid analysis and the spectrum with 10% energy reduction. The spectrum obtained by the hybrid analysis is consistent with the HiRes data within the systematic uncertainty of the fluorescence yield models.

In general, the water vapor makes the fluorescence yield decrease by the quenching effect. The humidity dependence of the fluorescence yield is reported[58] and the yield is reduced by about 20% when the relative humidity is changed from 0% to 100%. For this analysis, the effect is less than 5% and not large because the experimental site is on the desert.

The systematic error of the energy from the fluorescence yield is estimated to be 12% from

the measurement of the absolute yield ($\pm$10%)[22] and humidity dependence(5%).

The uncertainty of the atmospheric parameter also causes the uncertainty of the fluorescence yield. The radiosonde database consists of the average values every month. The standard deviation of the pressure is less than 3% at 5km height and less than 1% on the ground. At the altitude of 10km, the standard deviation of the pressure is less than 3% and the temperature is less than 10% by the unit of degrees C. By these atmospheric uncertainties, the systematic error of the fluorescence yield is less than 3%.

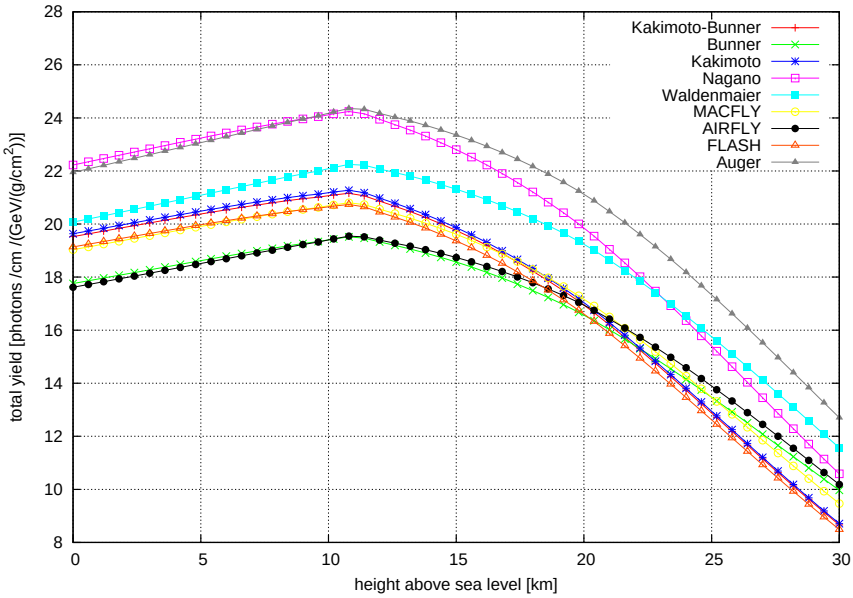

Fig. 107: The comparison of the fluorescence yield models with the US standard atmosphere[24]. The horizontal axis is the height above sea level and the vertical axis is the total fluorescence yield. The red line is the Bunner model[52] scaled by absolute yield of the Kakimoto model[22]. The green line is the Bunner model. The blue line is the Kakimoto model. The purple line is the Nagano model[53][54]. The light blue line is the Waldenmaier model [55]. The yellow line is the MACFLY model[56]. The black line is the AIRFLY model[57]. The light red line is the FLASH model scaled by absolute yield of the Kakimoto model[23] which is used in this analysis. The gray line is the AirFly model scaled by aboslute yield of the Nagano model which is used in Auger analysis[8]

11.3 Detector calibration

The main systematic error for the detector calibration is caused by the absolute calibration of the CRAYS. The systematic error is estimated to be about 8%[36] which is caused by the accuracy of the energy probe for the laser power measurement.(see Section 4.4)

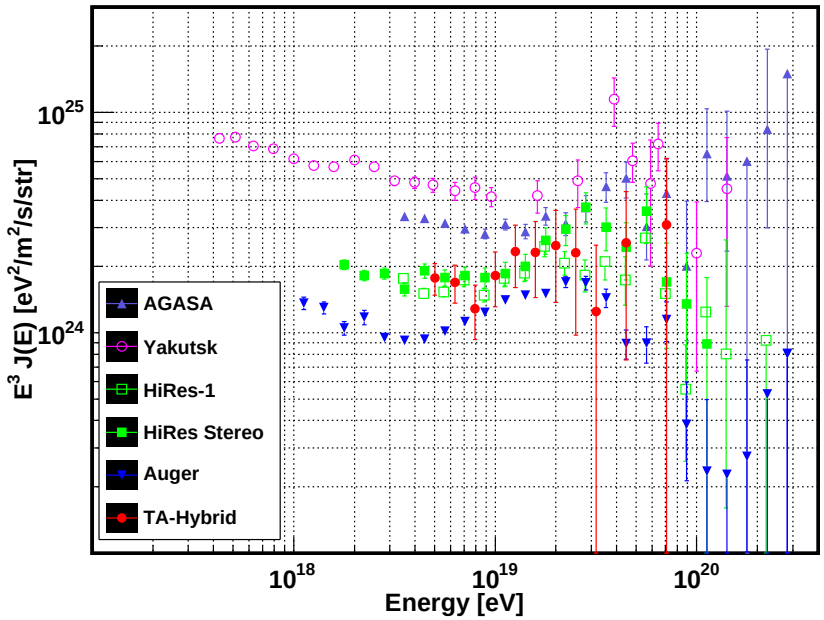

Fig. 108: The energy spectrum with 3% increment of the fluorescence yield. The configuration of this figure is the same as Fig. 106.

The gain of the PMT will be changed by the aging effect. We monitor the aging effect by the YAP. (see Section 4.4). The result of the YAP analysis shows that the gain of each camera is not shifted. The standard deviation of the amount of the gain shift of each camera is less than 3%.

The systematic error of the mirror reflectance is estimated to be about 3% by the systematic uncertainty on the spectrophotometer and interpolations of time variations(see Section 4). The time variation of the mirror reflectance is traced by using the typical value for each height of the mirror. The standard deviation of the reflectance in each height is less than 2%. The mirror area also has uncertainty at the edge and center by the anodization. The uncertainty is estimated to be 2%. So the total uncertainty of the mirror reflectance is estimated to be 5%.

We use the average value of the transmittances of the filters for all filters. The standard deviation of all measured filters is about 1%. The other factors are the time variation of the transmittances of the camera window, but the decrease is about 1% since the camera plane faces downwards.

So the total uncertainty of the detector calibration is estimated to be 10%.

11.4 Atmospheric attenuation

In this analysis, the typical value is used for the attenuation of the Mie scattering: the attenuation length on the ground is 29.4km and the scale height is 1.0km (see Section 4.5). The standard deviation of the attenuation length on the ground is $\pm$ 13km. On the other hand, in the hybrid events, the distance of the shower axis from the FD station is less than 30km because we use SD information(Fig. 89). The covered elevation angle of the telescope with lower field of view is from 3° to 18°. So in this study, the effect of the attenuation length of Mie scattering is calculated at 30km far from the FD station and 10 degrees elevation angle as the maximum systematic difference.

When the attenuation length is 29.4km, the amount of emitted photons is reduced to 85% at the telescope. On the other hand, when the attenuation length is 29.4km - 13km, the amount is changed to 75%. So the systematic error of the Mie extinction is estimated to be 10%.

The attenuation of the Rayleigh scattering depends on the uncertainty of the atmospheric pressure. The radiosonde database consists of the average monthly values. The standard deviation of the pressure is less than 3% at an altitude of 5km and less than 1% on the ground. The total uncertainty of the attenuation by the Rayleigh scattering from 30km distance and 10 degree elevation angle from the FD station is less than 5%

11.5 Monte Carlo

The reconstructed energy is corrected by the systematic shift of reconstructed value from the true in MC data. The correction factors are different for each energy. However, the correction factors have the fluctuation by the statistics of the COSMOS MC database. From Fig. 71, the maximum fluctuation is estimated to be 3%, which is considered as the systematic error.

11.6 Cloud

The cloud also affects the energy spectrum. For excluding the cloudy time, the WEAT code is used in this analysis (see Section 4.5.4, Section 9.1). To estimate the effect of the cloud cut, the energy spectrum without cloud cut is also calculated. The process to obtain the energy spectrum without cloud is the same as the process for the spectrum with cloud cut. After the analysis, 185 events remained. The obtained spectrum and comparison with the spectrum with cloud cut are shown in Fig. 109. The difference of the flux of these spectra is estimated by fit of the flat line. The fitted scale is 0% $\pm$ 12%. Since the amount of the data is small, the effect of the cloud does not appear clearly. So 12% which is the error of this result is used as the systematic error of the flux.

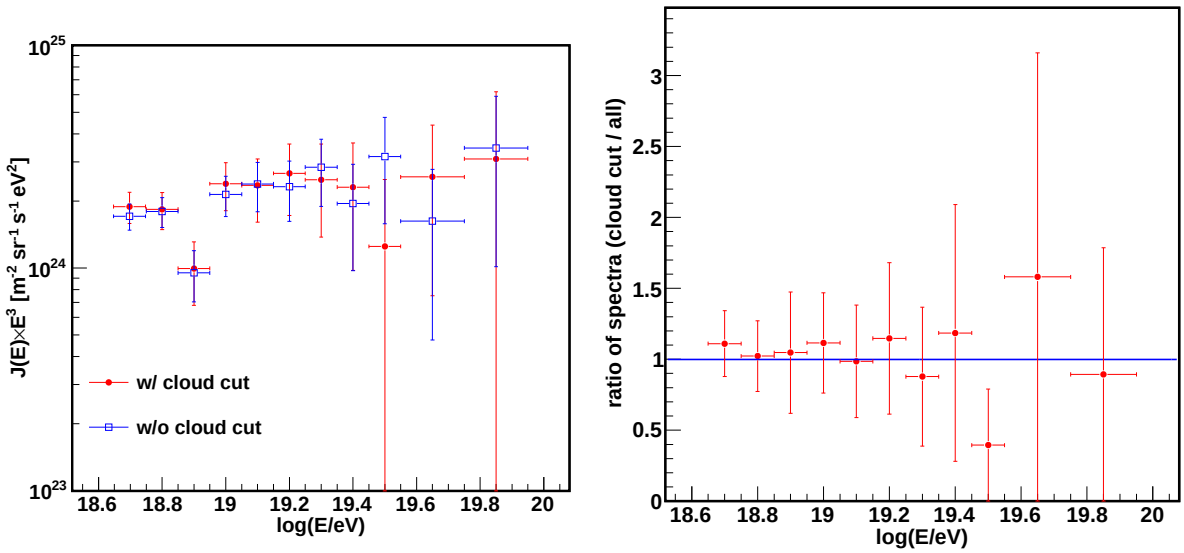

Fig. 109: The energy spectra calculated by using the cloud cut and by using all of the data (left figure) and the ratio of the spectra (right figure). In the left figure, red circles show the spectrum calculated by using the cloud cut and blue squares show the spectrum calculated by using all of the observed data. The horizontal axis is the energy and the vertical axis is the flux $J(E)\times E^3$. In the right figure, red circles show the ratio of these spectra and blue line is fitted by the flat line. The fitted scale is 1.00 ± 0.12 .

11.7 Summary of systematic error

The estimated systematic uncertainties for the energy measurement are summarized in Table. 8. The total systematic uncertainty of energy is 19%. This value is almost same as the other experiment (AGASA:18%, HiRes:17%, Auger:22%). The total systematic uncertainty of flux is 12% as described in Section 11.6. The spectrum with energy systematic error is shown in Fig. 110.

Item	Error	Comments
Detector sensitivity	10%	PMT(8%), mirror(5%), filter(1%) aging(3%)
Atmospheric attenuation	11%	Mie(10%), Rayleigh(5%)
Fluorescence yield	12%	measurement(10%), atmosphere(3%) humidity(5%)
Primary particle mass	5%	
MC correction	3%	
Quadratic sum	19%	

Tab. 8: The estimated systematic uncertainties of the energy measurement. The detector sensitivity is described in Section 11.3. The atmospheric attenuation is described in Section 11.4. The fluorescence yield is described in Section 11.2. The atmospheric attenuation is described in Section 11.4. The effect of the primary mass particle is described in Section 6.1. The MC correction is described in Section 11.5.

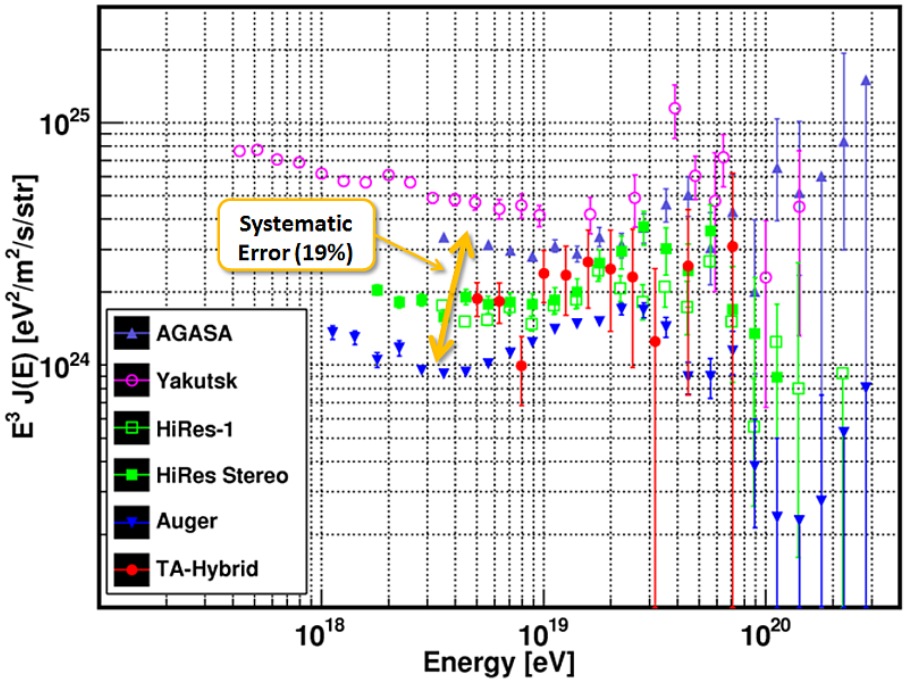

Fig. 110: The energy spectrum with the systematic uncertainty of the energy. The yellow arrow shows that of the systematic uncertainty of energy (19%). The other configuration of this figure is the same as Fig. 106.

12 Discussion

In this thesis, the precise analysis technique for hybrid events was developed, and the energy spectrum of the UHECRs above $10^{18.7}$eV was measured by using hybrid events observed with the TA detector for one and a half a year. The measured spectrum is consistent with the HiRes spectrum.

The measurement of spectrum by FD has the merit because energy is measured calorimetrically, but it has the demerit of uncertainty of the estimated aperture because of its energy dependence. On the other hand, in the hybrid analysis, the energy is measured by the FD in the same way as the HiRes technique, and the aperture above $10^{19.0}$eV by SD is flat and reliable. The consistency between the spectrum measured by the hybrid analysis and the HiRes spectrum also means the justification of the aperture of the HiRes experiment.

In future, the following items related to the hybrid analysis will be studied and updated;

1. energy scale and flux by FD
2. energy spectrum below $10^{19.0}$eV
3. comparison of energy scale between FD and SD
4. zenith angle

In this section, the above items are discussed.

12.1 Energy scale and flux by FD

In the hybrid analysis, systematic uncertainty of the measured energy is 19%. The main contributions are fluorescence yield, detector sensitivity and atmospheric attenuation. Since the above uncertainties are common for FD observation, the HiRes and Auger experiments showed almost same uncertainties: 17% for the HiRes FD and 22% for the Auger FD.

End-to-end absolute calibration by ELS

The TA experiment will have absolute calibration technique by the electron linear accelerator called ELS which was described in Section 4.6. By observing fluorescence light from air shower induced by electron beam with known total energy, fluorescence yield and detector sensitivity will be calibrated with about 5% uncertainty. This end-to-end calibration on the FD site is the first trial in the world and will start in the spring of 2010. The systematic errors with and without the ELS are shown in Table. 9. The systematic uncertainty wil be improved from 19% to 14%.

Item	w/o ELS	w/ ELS
Fluorescence yield	12% measurement(10%) atmosphere(3%) humidity(5%)	8% ELS(5%) atmosphere(3%) humidity(5%)
Detector sensitivity	10% PMT(8%) mirror(5%) filter(1%) aging(3%)	
Atmospheric attenuation	11% Mie(10%) Rayleigh(5%)	
Primary particle mass	5%	
MC correlation	3%	
Quadratic sum	19%	14%

Tab. 9: The comparison of systematic uncertainty in measuring energy with and without the ELS calibration.

Atmospheric attenuation

After applying the ELS calibration, the main uncertainty in the energy measurement will be atmospheric attenuation. The atmospheric condition is measured by the LIDAR at the beginning and at the end of the observation every day. If the number of hybrid events is increased, the events only with good weather will be used for the analysis. In addition to the LIDAR, the laser from the CLF is shot every 30 minutes during the observation. By using the CLF events as the relative measurement of the atmosphere, the atmospheric correction will be improved from the frequent measurement. The TA will aim at around 10% of the total systematic error of the measured energy. This is much smaller than the difference ($\sim$20%) of the energy scales between the AGASA, HiRes and Auger experiments. Thus the energy scale of UHECRs by the hybrid analysis of the TA experiment will be determined with the best accuracy among the experiments for the observation of UHECRs.

Cloud monitoring for improvement of aperture

Cloud is one of the uncertainties in the calculation of the aperture. In this analysis, the WEAT code which is recorded by the MD operator is used for the cloud cut. The TA also has the IR camera for the cloud monitor. However, it was not used for this analysis because the

period when the IR camera was operated is less than 50% of the used data set. Recently the fraction of the period when IR camera was stably operated was increased up to more than 80%. In future, the number of the observed data will be increased, and only data with good weather will be used for the analysis. In March 2011, the exposure will be twice of the data set used in this thesis. So 12% systematic error of the flux will be decreased.

12.2 Energy spectrum below $10^{19.0}$eV

Physics below 10^{19}eV

The energy spectrum includes the dip around the energy of $10^{19.0}$eV[59] in addition to the GZK cutoff. The energy spectra from the other experiments become almost same structure after the shift of energy scales to the HiRes spectrum (Fig. 111). There are two models to explain the dip. One is the pair-production model. The dip is created by the pair-production between UHECR and CMB. In this case, the UHECRs are protons. The other is that the origin of UHECRs around $10^{19.0}$eV changes from the our galaxy to extra-galaxy. In this case, the transition of mass composition should be observed because the maximum energy of irons by acceleration is higher than that of protons in the same magnetic field. So the measurement of the energy spectrum and mass composition below 10^{19}eV is important for the estimation of the origin of UHECRs.

Hybrid trigger

One of the merit of the hybrid analysis by comparing with the FD monocular analysis is that the aperture is determined by SD precisely. The aperture above the energy of 10^{19}eV is flat, but the aperture below the energy of 10^{19}eV is reduced due to inefficiency of the current SD trigger. The typical trigger efficiency of SD is shown in Fig. 72. For example, the trigger efficiency of SD is only 10% at the energy of 10^{18}eV.

To extend the energy region to the lower energy, the hybrid trigger, by which SD is triggered by FD, will be installed to the TA data acquisition. By the hybrid trigger, the aperture at the energy of 10^{18}eV will be 100%. So the energy spectrum measured by the hybrid analysis will be extended down to around $10^{17.5}$eV, which is the same as the FD monocular spectrum by the HiRes experiment. The hybrid trigger will be installed in the middle of 2010.

The energy and mass composition are measured with accuracy from the energy of $10^{18.7}$eV by the developed hybrid analysis. The hybrid analysis of the TA experiment is aimed toward the measurement of the transition of mass composition and energy spectrum from the energy of $10^{17.5}$eV with energy scale of about 10% accuracy by the inclusion of more information from atmospheric monitoring, the improvement of energy calibration by ELS, and the installation of the hybrid trigger.

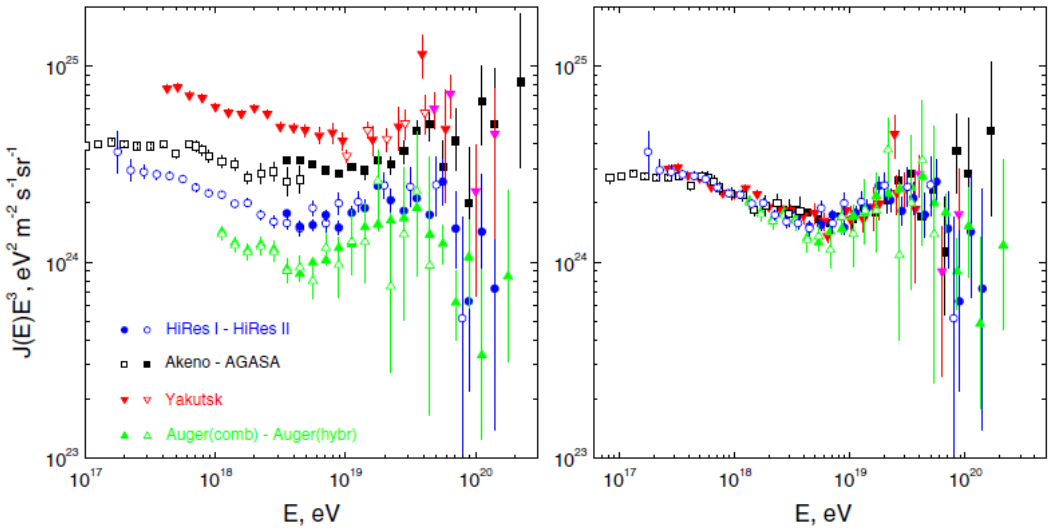

Fig. 111: The comparison of the energy spectra of the UHECRs (left panel) and the spectra scaled to the HiRes spectrum (right panel)[59]. The horizontal axis is the energy of the primary cosmic rays and the vertical axis is the flux multiplied by E^3. The blue filled circles represent the data by HiRes-I. The blue open circles represent the data by HiRes II. The black open squares represent the data by Akeno. The black filled squares represent the data by AGASA. The red filled and open triangles represent the data of Yakutsuk. The green filled triangles represent the spectrum by Auger, for which the data of the hybrid analysis and SD analysis are combined. The green open triangles represent the data of the hybrid analysis by Auger.

12.3 Comparison of energy scale between FD and SD

Energy scales by FD and SD

One of the most important subjects of the hybrid analysis in TA is the comparison of energy scale between FD and SD. The TA SD is a plastic scintillator detector, which is the same as the AGASA detector, and one set of the telescopes among three TA FD stations is transferred from the HiRes site. The Auger experiment also has the hybrid detector, but the SD is a water Cherenkov detector, which is sensitive to muons. So different components of air showers are observed with the SDs in the Auger and TA experiments. The hybrid observation only by the TA experiment corresponds to the direct comparison between the AGASA and HiRes results.

The comparison of energy scales between FD and SD is not finished yet because the SD analysis is not currently ready. The SD analysis will be ready within half a year. The number of hybrid events above $10^{18.7}$eV with quality cuts is 124 events from the observation for one and half a year, and it is enough for the check of the energy scale between FD and SD. So this work will be performed by the end of this year.

12.3.1 Energy spectrum above $10^{18.7}$eV

The measurement of the energy spectrum above $10^{19.5}$eV is the most important subject in TA experiment. By the improvement of the energy scale, the hybrid analysis will have the least uncertainty in measuring energy. However, the statistics of hybrid events is not enough for the measurement of the spectrum around the energy region of the GZK cutoff because the exposure above $10^{19.0}$eV is 1/10 of that by SD. The FD monocular analysis has the statistics larger than that by the hybrid analysis and precise energy scale that is the same as the hybrid analysis, but the aperture only by FD has more uncertainty. The technique both with the precise energy scale by FD and precise aperture by SD is to use the new energy estimator which is obtained by the comparison with the FD energy and the density of energy deposit measured by SD in the hybrid events. The method is mentioned below.

From SD data, energy is measured by using the density of energy deposit at a fixed distance from shower core position on the ground. AGASA used 600m for a distance from shower core position. The relation between the energy deposit on the ground and energy of the UHECRs is obtained by using air shower MC simulation. However, the lateral distribution by air shower MC simulation has large uncertainty of hadronic interaction. The Auger experiment uses hybrid technique to measure the energy spectrum. Fig. 112 shows the comparison between the energy measured by FD and the density of the energy deposit at a distance of 1000m from the core position measured by SDs. This relation in Fig. 112 cannot be applied to the TA experiment directly because the SDs in the Auger experiment are water tank (not plastic scintillator). So it is necessary to measure the relation between FD and SD with plastic scintillator for the TA experiment. The exposure of the TA SD will reach about twice of the AGASA total exposure

in March of 2011, and the TA will measure the energy spectrum above $10^{19.5}$eV with energy uncertainty of 10% level by the hybrid technique and ELS.

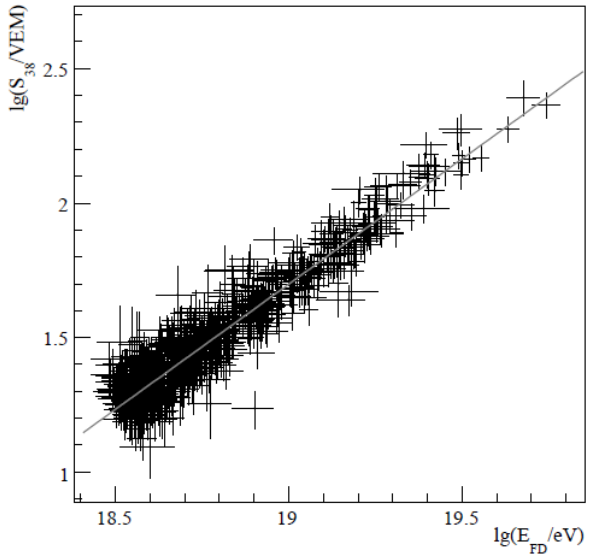

Fig. 112: The comparison of the energy measured by FD and the density of energy deposit measured by SD in the Auger experiment[8]. The horizontal axis is the energy measured by the FD. The vertical axis is the density of the energy deposit at the distance of 1000m from the core position which is equivalent to the zenith angle of 38 degrees measured by the SD. The black line is the estimated relation from this scatter plot.

12.3.2 Model dependence

If the energy scales between SD and FD are inconsistent, there is a possibility that the difference is originated from air shower MC. The energy is determined by using lateral distribution of the air shower on the ground from SD data. The lateral distribution depends on hadronic interaction of UHECRs with atmospheric molecules. However, the lateral distribution by MC simulation has large uncertainty because the energy of UHECRs is much larger than the energy of particles generated by the existing accelerators. For example, the center of mass energy of the collision between the proton of the energy of 10^{20}eV and atmospheric molecules is 433TeV. On the other hand, the center of mass energy of the Tevatron is 2TeV and that of the LHC will be 14TeV.

The theories of the high energy interaction is also being improved. One of the recent models is the Color Glass Condensate (CGC), which describes the saturation of the gluons[60]. Since CGC effect causes the suppression of the forward scattering, it is expected that the X_{max} becomes smaller than that by the existing models[61]. It also affects the energy scale by SD. The framework of the CGC is also planned to be installed to the CORSIKA air shower

simulator[62]. The air shower simulation will be improved by the theories such as the CGC together with the result of the LHC. For example, the LHCf experiment will distinguish the existing models and provide the proper hadron interaction model used for UHECRs[63]. The above-mentioned improved high energy hadronic model will be used for the comparison of the results of hybrid events between the observed data and MCs

12.4 Zenith angle

The available number of hybrid events will be increased by changing the zenith angle cut. The zenith angle used for the analysis is currently limited at 45 degrees because the MC events are generated below 50 degrees. If the limit of zenith angle is changed to 60 degrees, the number of hybrid events will be increased by about 30%. By the change of the limit of zenith angle to 60 degrees, the available number of hybrid events will be about 1,000 above the energy of $10^{18.5}$eV and about 200 above the energy of 10^{19}eV by March of 2011.

13 Conclusion

The Telescope Array is the largest stereo-hybrid detector for UHECR observation in the northern hemisphere with the three Fluorescence Detectors (FDs) which are the same as the HiRes technique and 507 Surface Detectors (SDs) which are the same as the AGASA technique. In this analysis, the hybrid events which are observed both by FD and SD are used to measure the energy spectrum with the developed hybrid reconstruction technique.

To carry out this study, the method of the hybrid analysis, in which the timing of SD data is applied to FD monocular reconstruction, is developed. A full hybrid Monte Carlo (MC) simulation with an air shower simulation is developed. The MC simulation includes the Utah atmosphere and the detector response with the time dependence.

The resolutions which are estimated by using the MC simulation are less than 1.1 degrees of the arrival direction and less than 8% of the energy for the observed UHECRs with energies above $10^{18.7}$eV, respectively. These resolutions are quite better than that of the FD monocular analysis. For example, the resolutions of the arrival direction of those are several degree for the events with the energy of $10^{18.7}$. The aperture of the hybrid event is also obtained by using MC simulation.

The used term of the data is from May 27, 2008 to September 28, 2009. The exposure is about 3×10^{15} m^2 sr s for at the energy of 10^{19}eV, which is equivalent to 6% of the AGASA exposure. About 2000 hybrid events are found with one FD station (monocular-hybrid events) and about 200 events hybrid events with two FD stations (stereo-hybrid events).

In this hybrid analysis, the main contributions to the systematic uncertainty of energy and flux measurements are the PMT calibration (8%), mirror reflectance (5%), atmospheric attenuation (11%), fluorescence yield (12%). The total systematic error of the energy measurement is estimated to be 19% by a quadratic sum of these factors. The total systematic uncertainty of the flux is estimated to be 12% by the cloud.

The measured energy spectrum with the developed hybrid technique with energies above $10^{18.7}$ eV is consistent with the result of HiRes within the systematic uncertainty.

By the March of 2011, the systematic uncertainty of the energy will be improved to around 10% level by the ELS calibration and the data selection of the good weather. By the improvement of the SD analysis, the energy scale between FD and SD will be compared by the hybrid analysis as the direct comparison between the AGASA and HiRes results. This work will become the verification of the inconsistency of the result of the GZK cut off. In March of 2011, the exposure of the TA will reach about twice of the AGASA total exposure. The TA will measure the energy spectrum around the GZK cut off with the energy uncertainty of 10% level by the hybrid technique and ELS calibration.

References

[1] M.Takeda et al., Phys.Rev.Lett.81, 1163(1998).

[2] R.Abbasi et al., Phys.Rev.Lett.100, 101101 (2008)

[3] K.Greisen, Phys.Rev.Lett.16, 748(1966).

[4] G.T.Zatsepin and V.A.Kuzmin, JETP.Lett.81, 1163(1998).

[5] http://www-hdnew.fnal.gov/tevatron/

[6] http://lhc.web.cern.ch/lhc/

[7] http://www.telescopearray.org/

[8] J.Abraham et al., Proceedings of the 31th ICRC

[9] M.A.MALKAN et al, Astro.Phys.496, (1998).

[10] Hinshaw G et al, astro-ph/0603451.

[11] S.Yoshida, M.Teshima, Prog.Theor.Phys.89, 833(1993).

[12] G.R.Blumenthal, Phys.Rev.D 1, 1956(1970).

[13] H.Bethe and W.Heitler, Proc.Roy.Soc. A146, 83(1934).

[14] F.W.Stecker, astro-ph/0908110.

[15] J.L.Puget et al, AstroPhys. 205, 638 (1976).

[16] T.Yamamoto, K.Mase, T.Takeda, N.Sakaki, M.Teshima AstroPart.Phys.20, 405(2004).

[17] A.M.Hillas, Ann.Rev.Astron.Astrophys.22, 425(1984).

[18] K.Ptitsyna, S.Troitsky, atsro-ph/0808.0367

[19] V.A.Kuzmin and V.A.Rubakov. Phys.Atom.Nucl.,24, 61 (1998)

[20] M.Nagano et al., J.Phys.G:Nucl.Part.10, 1295(1984).

[21] A.N.Buerner, Ph.D. thesis, Cornell University, 1967.

[22] F.Kakimoto et al, Nucl.Instrum.Meth.Phys.Res.A 372, 244(1996).

[23] R.Abbasi et al, AstroPart.Phys.29, 77 (2008)

[24] http://modelweb.gsfc.nasa.gov/atmos/us_standard.html

[25] D.Heck et al., Report FZKA 6019, 1998

[26] GEANT 3.21, CERN Program Library Long Writeups W5013, 1994

[27] F.Nerling et al., AstroPart.Phys.24, 421 (2006)

[28] J.Alcaraz et al., Phys.Lett.B 490, 27 (2000)

[29] J.Alcaraz et al., Phys.Lett.B 494, 193 (2000)

[30] T.Nonaka et al., Proceedings of the 31th ICRC

[31] A.Taketa et al., Proceedings of the 31th ICRC

[32] A.Taketa et al., Proceedings of the 29th ICRC

[33] Y.Tameda et al., Nucl.Instrum.Meth.Phys.Res.A 609, 227 (2009)

[34] D.Ikeda et al., Proceedings of the 31th ICRC

[35] H.Tokuno et al., Nucl.Instrum.Meth.Phys.Res.A 601, 364 (2009)

[36] S.Kawana et al., Proceedings of the 31th ICRC

[37] S.Ogio et al., Proceedings of the 31th ICRC

[38] http://www-frd.fsl.noaa.gov/mab/raob/

[39] S.Machida et al., Proceedings of the 29th ICRC

[40] T.Tomida et al., Proceedings of the 31th ICRC

[41] R.Abbasi et al., AstroPart.Phys.25, 74 (2006).

[42] M.Chikawa et al., Proceedings of the 31th ICRC

[43] S.Agostinelli et al., Nucl.Instrum.Methods Phys. Res., Sect, A 506, 250 (2003).

[44] T.Shibata et al., Nucl.Instrum.Methods Phys. Res., Sect, A 597, 61 (2008)

[45] http://cosmos.n.kanagawa-u.ac.jp/cosmosHome/index.html

[46] K.Kasahara et al., Proceedings of 30th ICRC

[47] F.Choen et al., Proceedings of 30th ICRC

[48] Y.Tameda, Ph.D. thesis, Tokyo Institute of Tecnology, 2010

[49] P.A.Sadowski et al., AstroPart.Phys.18, 237 (2002)

[50] http://heasarc.gsfc.nasa.gov/W3Browse/all/td1.html

[51] V.P.Egorova et al., Nucl.Phys.B 136, 3 (2004)

[52] A.N.Bunner, Ph.D.Thesis, Cornell Universicy, (1967)

[53] M.Nagano et al., Astropart.Phys.20, 293 (2003)

[54] M.Nagano et al., Astropart.Phys.22, 235 (2004)

[55] T.Waldenmaier et al., Astropart.Phys.29, 205 (2008)

[56] P.Colin et al., Astropart.Phys.27, 317 (2007)

[57] M.Ave et al., Astropart.Phys.27. 317 (2007)

[58] M.Ave et al., Nucl.Instrum.Meth.Phys.Res.A 597, 50 (2008)

[59] V.Berezinsky et al., Nucl.Phys.B 188, 227 (2009)

[60] E.Iancu and R.Venugopalan., hep-ph/0303204

[61] H.J.Drescher et al., Phys.Rev.Lett 94, 231801 (2005)

[62] S.Ostapchenko., presenattion in the TeVPA (2008)

[63] T.Sako et al., Proceedings of the 31th ICRC